

FAST NEUTRON CROSS SECTIONS IN THE 2s-1d SHELL

FAST NEUTRON CROSS SECTIONS IN THE 2s-1d SHELL

By

GEOFFREY ROSS NORMAN, B.Sc.

A Thesis

Submitted to the Faculty of Graduate Studies

in Partial Fulfilment of the Requirements

for the Degree

Doctor of Philosophy

McMaster University

July 1971

DOCTOR OF PHILOSOPHY (1971)
(Physics)

McMASTER UNIVERSITY
Hamilton, Ontario.

TITLE: Fast Neutron Cross Sections in the 2s-1d Shell

AUTHOR: Geoffrey Ross Norman, B.Sc. (University of Manitoba)

SUPERVISOR: Dr. T. J. Kennett

NUMBER OF PAGES: x, 154

SCOPE AND CONTENTS:

A new technique has been developed for the measurement of fast neutron total cross-sections in the range $0.8 \rightarrow 3.0$ MeV using the fast neutrons from a reactor. The method was used to obtain the cross-section of six elements in the 2s-1d shell. Various analytical techniques have been applied to measure the behavior of the average cross-sections and delineate the properties of the observed resonances. From these results the resonances are confirmed as examples of "doorway" states, and conclusions are drawn about the distributions of the parameters of these states. The average properties are related to nuclear models of the origin and characteristics of states of high excitation in the target nuclides.

ACKNOWLEDGEMENTS

I wish to thank my research director, Dr. T. J. Kennett, for his advice and encouragement, and many stimulating discussions during the course of this project. Thanks are due also to the members of my supervisory committee, Dr. J. A. Kuehner and Dr. W.H. Fleming, for putting me back on the track from time to time. I also wish to acknowledge the assistance of Dr. W. V. Prestwich and Dr. R. K. Bhaduri, who assisted me over some theoretical stumbling blocks. And to several of my fellow graduate students, particularly Mr. A. H. Colenbrander and Mr. Morley Davis, for aid in some of the menial tasks, and for relief from boredom in the office.

Thanks are also due to the reactor staff who carried on with the experiment at all hours of the day or night and particularly night, and to Helen Kennelly, whose typing efficiency approaches unity.

On the personal side, I am indebted to my wife whose talents with a drafting pen are unapproachable, and who has discovered that good books make a poor substitute for love and attention.

Finally thanks go to my dog, who treated my manuscript with special care by leaving it intact, unlike other volumes in my possession.

TABLE OF CONTENTS

	<u>Page</u>
CHAPTER I INTRODUCTION	1
1.1 Neutron Cross Sections and Nuclear Structure	1
1.2 The Optical Model	4
1.3 Compound Nucleus and Statistical Model	7
1.4 Unified Theory of Nuclear Reactions - Doorway States	9
CHAPTER II PREVIOUS WORK	16
CHAPTER III TECHNIQUES AND INSTRUMENTATION	22
3.1 General Considerations	22
3.2 The Experiment Configuration	23
3.3 The Neutron Source	23
3.4 Collimation and Shielding	25
3.4.1 General Consideration	25
3.4.2 Specific Configuration	27
3.5 The Detector	32
3.5.1 Choice of Detector	32
3.5.2 Nature and Characteristics of Detection Mechanism	33
3.5.3 Characteristics of Neutron Response	34
3.5.4 Application to Experiment	41
3.6 General Consideration of Experiment Design	43
3.7 Experiment Configuration - Physical Layout	48
3.8 Experiment Configuration - Instrumentation	49

	<u>Page</u>
3.9 The Fast Comparator Circuit	53
3.10 Time-to-Amplitude Convertor	54
3.11 The TAC Gate Module	55
3.12 The Experiment Controller Module	56
3.13 The Multichannel Pulse Height Analyser	62
CHAPTER IV DATA ANALYSIS	65
4.1 Cross-Section Calculation	65
4.2 Data Reduction - General Considerations	67
4.3 Computer Calculations	69
4.3.1 Calculations with Individual Spectra	69
4.3.2 Cross-section Calculation	73
4.4 Discussion of Errors	76
4.4.1 Errors in Magnitude of Cross-Section	77
4.4.2 Errors in Energy Calculation	81
4.4.3 Errors in $d\sigma/dE$ -Energy Resolution	83
CHAPTER V RESULTS	86
5.1 Selection of Sample Elements	86
5.2 Experimental Cross Section Results	87
5.3 Discussion of Individual Cross-Sections	89
5.4 Additional Data	92
CHAPTER VI ANALYSIS OF AVERAGE CROSS SECTION	96
6.1 Introduction	96
6.2 Solution of Schroedinger Equation	99
6.3 Optical Model Results	100

	<u>Page</u>
CHAPTER VII ANALYSIS OF INDIVIDUAL RESONANCES	102
7.1 Introduction	102
7.2 Calculation of True Resonance Parameters	103
7.3 Distribution of Widths	109
7.4 Widths and Spacings of Compound Nucleus Resonances	112
7.5 Application to Present Experiment	116
7.6 Energy Dependence of Doorway State Widths	119
CHAPTER VIII SPECTRAL ANALYSIS OF CROSS-SECTIONS	120
8.1 Signal Analysis Techniques	120
8.2 The Auto-correlation Function	121
8.3 The Power Spectrum Function	122
8.4 Detailed Properties of Auto-Correlation and Power Spectrum	124
8.5 Experimental Results	127
8.6 Correlation Between Widths and Spacings in Auto-correlation Function	130
8.7 Distributions of Widths and Spacings-Model Distributions	133
CHAPTER IX DISCUSSION OF RESULTS	137
9.1 Nuclear Parameters and Nuclear Cross-Sections	137
9.2 Average Fluctuation Amplitude and Ground State Spin	139
9.3 Cross-Section Fluctuations and Nuclear Deformation.	144
BIBLIOGRAPHY	151

LIST OF TABLES

<u>NUMBER</u>		<u>Page</u>
I	Size of Samples Used in Present Experiment	88
II	Previous Experimental Results in 2s-1d shell	93
III	Widths and Amplitudes of Resonances 800 keV \rightarrow 4000 keV	110
IV	Average Compound Nucleus Parameters of F, Al, Ca.	117
V	Average Parameters of Picket Fence Distribution	131
VI	Average Parameters of Experimental Distri- butions	131
VII	Spin, Deformation and Auto-Correlation Function A = 19 \rightarrow 40	146

LIST OF ILLUSTRATIONS

<u>FIG. NO.</u>	<u>TITLE</u>	<u>Following Page</u>
1	Schematic Representation of Experiment	23
2a	Neutron Flux at Various Distances from Core	23
2b	Neutron Distribution in Flight Time	24
3	Average No. of Collisions to Thermalize	27
4	Schematic Diagram of Beam Tube	28
5	Plan View of Experimental Shielding	29
6	Efficiency of Organic Scintillator	35
7	Illustration of Timing Walk	39
8	Variation of Transit Time with Radius	40
9	Overall Resolution Stop Counter	40
10	Illustration of Prompt Peak Function of Peak Height	42
11	Walk Function of Pulse Height	43
12	Calibration Pulse Height vs Proton Energy	43
13	Optimum Accumulated Counts Sample In and Out	45
14	Schematic-Instrumentation Layout	49
15	Schematic - Fast Comparator Circuit	53
16	Schematic - TAC Gate Module	55
17	Signals in TAC Gate Module	55
18	Schematic Experiment Controller Module	57
19	Signal in Experiment Controller Module	60
20	Schematic - Pulse Height Analyser	62
21	Flow Chart of First Program	69

<u>FIG. NO.</u>	<u>TITLE</u>	<u>Following Page</u>
22	Flow Chart of Second Program	73
23	Non linearity of Time Scale	75
24	Energy Resolution Function of ξ	85
25	Overall System Energy Resolution	85
26	Cross Section of Magnesium 0.8-4.0 MeV	89
27	Cross Section of Aluminum 0.8-4.0 MeV	90
28	Cross Section of Phosphorus 0.8-4.0 MeV	90
29	Cross Section of Chlorine 0.8-4.0 MeV	91
30	Cross Section of Potassium 0.8-4.0 MeV	91
31	Cross Section of Calcium 0.8-4.0 MeV	92
32	Cross Section of Fluorine 0.8-4.0 MeV	93
33	Cross Section of Sodium 0.8-4.0 MeV	93
34	Cross Section of Silicon 0.8-4.0 MeV	93
35	Cross Section of Sulphur 0.8-4.0 MeV	93
36	Relation Between True Width, Total Width, and Resolution	107
37	Relation Between True Amplitude, Observed Amplitude and Resolution	107
38	Distribution of Widths $A = 19 \rightarrow A = 40$	109
39	Distribution of Compound Nucleus and Inter- mediate Widths in F, Al and Ca	117
40	Width of Resonances Function of Energy in Fluorine	118
41	Width of Resonances Function of Energy in Aluminum	118
42	Width of Resonances Function of Energy in Calcium	118

<u>FIG. NO.</u>	<u>TITLE</u>	<u>Following Page</u>
43	Auto-Correlation Function of Picket Fence Cross Section	126
44-47	Auto-Correlation Functions $A = 19 \rightarrow 40$	127
48	Power Spectra $A = 19 \rightarrow 40$	129
49	Relation Between Auto-Correlation Width, Average Widths and Average Spacing in Experiment	132
50	W/Γ Function of D/Γ for Experimental and Theoretical Distributions	133
51	Damping of Auto-Correlation Function as a Function of D/Γ	140
52	Relation Between Variance and Deformation Parameter.	145

CHAPTER I

INTRODUCTION

1.1 Neutron Cross Sections and Nuclear Structure

The experimental study of neutron cross-sections has occupied an important position in the expansion of the field of knowledge of nuclear physics and has been crucial to applications of nuclear physics to solutions of problems in many fields of human endeavour. In particular, knowledge of the absorption and scattering of neutrons by nuclei is essential to the design of nuclear reactors and nuclear weapons, and the neutron cross-section is a basic parameter in the production of radioisotopes.

The neutron total cross-section of a nucleus is a measure of the strength of the interaction between the incident neutron and the nucleons. A study of this cross-section with coarse resolution reveals a smooth curve, as a function of energy, characterized by a broad resonance-like structure with periods of the order of millions of electron volts. Furthermore this resonance structure varies smoothly with atomic number throughout the periodic table. Theoretical interpretation of these trends has led to the development of the optical model description of nuclear reactions, which is discussed in more detail in section 1.2.

If by contrast, the cross-section is studied with very high resolution, one observes a multiplicity of extremely narrow resonances with characteristic shape, distributed throughout the range of neutron energies. As the neutron energy is increased, however, the average width of these resonances becomes comparable to the average spacing between resonances, and the cross-section exhibits random fluctuations. As the neutron energy is increased further, ultimately the fluctuations are smoothed out and the cross-section exhibits only slow variations with periods of the order of MeV.

This resonance structure in the neutron total cross-section was theoretically explained by the compound-nucleus model proposed initially by Bohr⁽¹⁾ and Bethe⁽²⁾, in which the neutron, upon entering the nucleus, undergoes successive interactions with nucleons, and gives up its energy to collective motions of all the nucleons. Because the time duration of this process is long in comparison with the transit time of the nucleus, from the Heisenberg uncertainty principle, this collective motion results in states of relatively well defined energy, with unique quantum numbers. These states are observed as the narrow resonances in the neutron cross-section. The compound nucleus model is discussed more fully in Section 1.3.

For neutron energies greater than a few hundred kilovolts, a third type of structure has been observed. This "intermediate" structure is characterized by resonance-like variations of cross-section with characteristic widths ranging

from a few tens of kilovolts to several hundred kilovolts. Particularly in the heavier elements, widths of this order lie well outside the limits predicted from the compound-nucleus model, but remain considerably less than the very broad resonance behavior of the optical model.

These resonances have been theoretically interpreted by Feshbach⁽³⁾, as evidence of the first interaction of the incident particle with a nucleon within the nuclear volume. This "doorway state" model provides a dynamic bridge between the interaction of the neutron with the nuclear potential, described by the optical model, and the multiple interactions of the compound-nucleus. Although of comparatively recent origin, this theory has been substantiated, at least qualitatively, by the observation of doorway-state type structure in many reactions. The model will be described in Section 1.4.

The present work constitutes a systematic investigation of the neutron cross-section from 800 keV to 4 MeV for all elements with $9 \leq Z \leq 20$. To facilitate this study, a new experimental method has been developed, using the continuous-energy beam from a reactor. Neutron flight times are measured by scattering from organic phosphors at the extrema of the flight path. From this investigation the existence of this intermediate structure will be confirmed and certain characteristics of the distributions of the parameters of the doorway states delineated. Finally we will attempt to correlate the observed intermediate structure with predictions derived from the theory.

1.2 The Optical Model

The optical model attempts to describe the interaction of incident particles with the nucleus by means of an average potential, representing the sum of potentials contributed by all the nucleons.

The name is derived from the formal analogy with the interaction between a plane wave of light and a semi-transparent spherical object. Thus absorption of incident particles corresponds with attenuation of the light wave in passing through the medium, and scattering corresponds to refraction and diffraction of the incident plane wave. To account for attenuation of the incident wave, the optical potential contains an imaginary component, thus for a spinless particle in a square well the radial wave function is of the form

$$\psi(r) = A e^{ikr} \quad (1.1)$$

where

$$k^2 = 2M(E-V-iW)/\hbar^2 \quad (1.2)$$

hence

$$\psi(r) = A e^{-\frac{\sqrt{2MW}r}{\hbar}} e^{ik'r}, k' \text{ real} \quad (1.3)$$

and the imaginary potential results in exponential attenuation of the incident beam.

Development of the model has resulted primarily in a refinement of potential shapes. For the real potential, it is obvious that the infinite discontinuity of the square well at the nuclear surface is unrealistic, and present day optical

potentials are primarily of the Wood-Saxon type:

$$V(r) = \frac{V_{ws}}{1 + e^{+(r-r_o)/a_w}} \quad (1.4)$$

This potential shape is constant inside the nuclear volume, falling to half the constant value at $r = r_o$, with a diffusiveness characterized by the parameter a_w .

The mechanism of absorption of particles from the incident beam implies an interaction within the nuclear volume resulting in the elevation of nuclear particles to excited states. From the Pauli exclusion principle no unoccupied states may exist in the interior of the nucleus in the ground state, hence, it is reasonable to assume an imaginary potential concentrated at the nuclear surface. Commonly this potential is of Gaussian form, or alternatively, derivative Woods-Saxon form

$$W(r) = iW \frac{e^{+(r-r_o)/a_d}}{\left[1 + e^{+(r-r_o)/a_d}\right]^2} \quad (1.8)$$

This potential is maximized near $r=r_o$, and decreases approximately exponentially with r , with diffuseness again characterized by a_d .

To account for the intrinsic spin of the incident particle, realistic optical potentials usually include a real spin-dependent component. This potential is characterized by the same radial dependence as the spin-independent imaginary

potential, but contains an ℓ -s coupling coefficient.

An additional refinement was introduced by Perey and Buck⁽⁴⁾, who used a two-body non-local potential of Woods-Saxon form. This model has been used to fit a large body of experimental cross-section and angular distribution data using a single parameter set.

The solution of the optical potential involves a matching of the wave function in the interior to the external free particle wave function by a consideration of resulting phase shifts at the nuclear surface.

The solution is obtained for each value of the orbital angular momentum ℓ by equating the wave function ψ_ℓ and its radial derivative $\frac{d\psi_\ell}{dr}$ at the boundary. The phase shifts, ϕ_ℓ , which are solutions of the boundary matching equations are related to the absorption plus scattering, and total cross-sections by the equations.

$$\eta_\ell = e^{2i\phi_\ell} \quad (1.9)$$

$$\sigma_{\text{elastic}}(\ell) = \pi\lambda^2(2\ell+1)|1-\eta_\ell|^2 \quad (1.10)$$

$$\sigma_{\text{abs}}(\ell) = \pi\lambda^2(2\ell+1)(1-|\eta_\ell|^2) \quad (1.11)$$

The total cross-section is then a sum over all ℓ ;

$$\sigma_{\text{Tot}} = \sum_{\ell} (\sigma_{\text{el}}(\ell) + \sigma_{\text{abs}}(\ell)) \quad (1.12)$$

A complete calculation of the cross-section must include consideration of non-elastic scattering channels open to

the incident particle. A procedure for calculating the contribution to the cross-section of inelastic scattering to excited states of the target nucleus has been outlined by Hauser and Feshbach⁽⁵⁾. This model assumes a statistical distribution of compound nucleus levels, and calculates branching to all channels open to the incident neutron.

In the range of neutron energy under consideration in the present experiment, inelastic processes may occur, however these contribute less than 15% to the total cross-section and will not be included in the present calculations.

1.3 Compound Nucleus and Statistical Model

The compound nucleus model was developed by Bethe⁽²⁾ and Bohr⁽¹⁾ in the 1930s. Ample evidence for the existence of a compound state has occurred since that time. One type of experimental evidence derives from the numerous measurements of low-energy neutron total cross-sections, which display prominent narrow resonances corresponding to the excitation of compound-nucleus states just above the neutron separation energy.

In this model the neutron energy is shared by many nucleons, resulting in the formation of a quasibound state of the compound system. Subsequent particle emission occurs when sufficient energy is concentrated on a nucleon, or group of nucleons, to overcome the attractive nuclear potential and escape from the nucleus. Because of the randomness

of such a mechanism, an assumption of the classical compound nucleus model is that the probability of decay to each exit channel is independent of the mode of formation. Certain calculations based on the compound nucleus, for example, the population of excited states of the target nucleus by inelastic scattering, employ an additional assumption, that the density of states in the compound nucleus is sufficiently high that an average over the energy interval of the incident beam will include a large number of states.

Using these properties of the compound nucleus, one may then determine certain general properties of the compound nucleus resonances observed in total cross-sections. In particular, the distribution of widths of these resonances has been calculated by Porter and Thomas⁽⁶⁾ using the method outlined in Section 7.4.

One may also investigate the distribution of spacings between resonances; by examining the density of states in the compound nucleus. The density of levels is sufficiently high that the calculation may be performed using the concepts of statistical mechanics. From such considerations it may be shown that the number of states, per unit energy of interval, representing the nucleus as a Fermi gas of $\sim N$ particles, is given by

$$\omega(E) \sim C E^{-5/4} \exp 2(aE)^{1/2} \quad (1.13)$$

Additional refinements include a correction for finite angular momentum and shell effects. However this

formula has been used extensively to fit experimental data with empirically assigned values of the parameters C and A.

Thus, the assumptions of the compound nucleus model provide a mechanism to explain the narrow resonances observed in neutron total cross-sections. Furthermore, distributions of resonance parameters may be obtained from this model, and theories have been developed to relate the observed widths and spacings to nuclear parameters, permitting an extrapolation of low energy results to the neutron energies encountered in the present experiment.

1.4 Unified Theory of Nuclear Reactions - Doorway States

The basis for the optical model is the concept of a virtual state of the incident particle in the field of the target nucleus. These states are experimentally observed as the single-particle resonances with widths of the order of millions of electron volts. An extension of this interpretation describes the intermediate width resonances in the cross-section as evidence of the population of simple modes of excitation with complexity between single particle and compound nucleus states. These states are postulated as being the only excitations which couple directly to the entrance channel, and the complex excitations corresponding to the compound nucleus must be generated as a coupling through these states. Thus these states, acting as "doorway" to the formation of the compound nucleus, are labelled as doorway states.

As a simplified model, we consider the case of a single incident nucleon impinging on a closed shell target nucleus. The initial wave function consists of the incident nucleon moving in the field of the nucleus. This interaction is described by a model Hamiltonian such as the optical model. Now if the residual interaction, corresponding to the difference between the model Hamiltonian and the true Hamiltonian, is a sum of two-body interactions, then the residual interaction acting on the incident one-particle wave function will excite a particle-hole pair. This $2p-1h$ state then is a doorway state, since by assuming a two-body residual interaction, the only states which couple to the entrance channel are $2p-1h$ states.

The multiple application of the residual interaction to these intermediate states will result in the formation of $(np-(n-1)h)$ states, which, for sufficiently high n , are observed as compound nucleus resonances. However these compound nucleus states are a selected subset of the totality of such states; the distinction arising from the mode of formation, which will selectively populate compound nucleus states which are strongly coupled to the doorway state.

Thus if a cross-section measurement were performed with good resolution, one should observe a "clumping" of compound nucleus resonances over an energy region corresponding to the range in energy over which the compound nucleus reso-

nances couple strongly to the doorway state. This energy range corresponds to the width of the doorway state observed in experiments with poorer resolution.

The doorway state, since it results from a single interaction, is not an eigenstate of the nuclear Hamiltonian. Consequently the state has a finite half-life, and therefore an observable width Γ_d . This width is comprised of two components Γ_d^\uparrow , for escape into the entrance channel, and Γ_d^\downarrow , for decay into the multi-particle excitations:

$$\Gamma_d = \Gamma_d^\uparrow + \Gamma_d^\downarrow \quad (1.14)$$

Detailed Theory

Certain detailed properties of the doorway state may be obtained from a theoretical analysis of the mechanism described above. This analysis, which will be given only for the case of an isolated $\ell = 0$ resonance, is due to Feshbach, Kerman and Lemmer⁽³⁾. Following the physical interpretation above, the nuclear wave function is decomposed into three mutually orthogonal components, comprising the entrance channel wave function, ψ_0 , the doorway states, ψ_d and the complex states leading from the doorway state ϕ_s .

These states may be interpreted as the result of projection on the total wave function by the projection operators, P , d , q respectively.

Thus

$$\psi_0 = P\psi, \psi_d = d\psi, \phi_s = q\psi \quad (1.15)$$

and

$$\psi = \psi_0 + \psi_d + \phi_s. \quad (1.16)$$

Then we examine an isolated eigenvalue at energy E_d of the doorway state Hamiltonian, defined as $H_{dd} = dHd$ and

$$(E_d - H_{dd})\psi_d = 0 \quad (1.17)$$

Using this representation in the unified theory^(7,8) of nuclear reactions formalism the intermediate model absorption cross-section may be shown to be of Lorentzian form,

$$\sigma_a(E) = \pi\lambda^2 T_0(E) \quad (1.18)$$

where

$$T_0(E) = \frac{\Gamma_d^\uparrow \Gamma_d^\downarrow}{(E - E_0)^2 + \frac{1}{4} \Gamma_d^2}$$

and

$$\Gamma_d = \Gamma_d^\uparrow + \Gamma_d^\downarrow \quad (1.19)$$

and

$$E_0 = E_d + \Delta_d^\uparrow + \Delta_d^\downarrow \quad (1.20)$$

$\Gamma_d^\uparrow, \Delta_d^\uparrow, \Gamma_d^\downarrow, \Delta_d^\downarrow$ are the width and energy shift associated with coupling to the entrance channel and to ϕ_s respectively.

Furthermore the respective widths are written as the square of matrix elements between ψ_d , and ψ_0, ϕ_s .

$$\Gamma_d^\dagger \approx \frac{2\pi}{\Delta E} \sum_q |\langle \phi_q | H_{qd} | \psi_d \rangle|^2 \quad (1.21)$$

$$\Gamma_d^\dagger = 2\pi |\langle \psi_d | H_{dp} | \psi_o \rangle|^2 \quad (1.22)$$

Γ_d^\dagger , therefore is a summation over the q eigenstates of the compound system which are directly coupled to the doorway state and are contained within an averaging interval ΔE . The interval ΔE is chosen such that $\Gamma_{c.n.} \ll \Delta E \ll \Gamma_d$, thus gives a local average of the compound nucleus resonances.

Therefore the doorway state resonance contains, in the numerator, the matrix element coupling the doorway state to the incident single particle state, and the matrix element coupling to the compound nucleus resonances in the region near the doorway state resonance energy to the doorway state.

Several other avenues have been explored theoretically. It may be shown, for example, that the doorway-state strength function is equivalent to a local average of the compound nucleus strength function, and is in turn related by averaging to the optical model transmission coefficient:

$$T_{opt}(E) = 2\pi \frac{\langle \Gamma_d \rangle}{\langle D_d \rangle} \sim 2\pi \frac{\langle \langle \Gamma \rangle \rangle}{\langle \langle D \rangle \rangle} \quad (1.23)$$

Furthermore, if one considers the conservation properties of the nuclear Hamiltonian, it may be shown that the doorway state will have unique spin and parity and that it will decay to compound nucleus states of the same spin and parity.

This property may be applied experimentally to the analysis of fine-structure resonances to provide confirmation of the doorway state.

Using this theory of intermediate structure certain properties of the intermediate resonance have been predicted by several authors:

(a) Damping Width Γ_d^\downarrow . The damping width is dependent on firstly the number of 2p-1h states available, and secondly, the number of 3p-2h states into which they may decay. Franco and Lemmer⁽⁹⁾ have calculated the number of these states around $N = 126$, and, using a residual two-body interaction for H_{dq} have determined the distribution of damping widths. This is found to resemble a Porter Thomas distribution with mean width of $\Gamma_d^\downarrow \approx 100$ keV, but is considered a very rough estimate of the true widths.

(b) Escape Width Γ_d^\uparrow . Because this width is less dependent on the detailed properties of available states, depending only on the number of 2p-1h states, the calculation is less complex than the calculation of damping widths. Lemmer and Shakin⁽¹⁰⁾ have performed this calculation based on shell model plus residual interaction, for inelastic scattering of neutrons from N^{15} and have obtained widths ranging from 0.6 to 800 keV for 12 resonances in the range of excitation energy < 10 MeV.

The average width is of the order of several hundred kilovolts.

(c) . Spacings of Doorway States $\langle D \rangle$. The average spacing is expected to vary from nucleus to nucleus, dependent on the detailed properties of nuclear structure. An estimate of the number of 2p-1h states, per unit energy interval, equivalent to the average spacing, has been obtained by LeCouteur⁽¹¹⁾ using a Fermi gas model, and has found an inverse dependence on excitation energy, and a decrease with mass number as A^{-2} . Shell model estimates yield an average spacing of 200 keV to 400 keV. However these are interpreted as very rough estimates. Kerman et al⁽¹²⁾ have inferred a dependence on mass number as A^{-1} for the average spacing. Furthermore, it is expected that doorway resonances will have maximum amplitude near a single particle resonance, and maximum spacing near closed shells.

CHAPTER II

PREVIOUS WORK

The measurement and interpretation of neutron total cross-sections has been of continuing interest since the early 1950's. The earliest systematic work was performed by Barschall^(13,14,15,16,17) and coworkers at Wisconsin in 1949-1952. This work encompassed a detailed and systematic investigation of about thirty elements through the periodic table in the energy region 0-3 MeV. The resolution of the experiments was about 7 keV, but the neutron energies were selected at intervals of about 25 keV in the region less than 1 MeV, and about 100 keV for energies greater than 1 MeV. Therefore, these experiments yielded little information on detailed resonance structure in the MeV range. However the systematic trends observed in the broad structure of the cross-section had a significant impact on nuclear theory leading directly to the evolution of the optical model of nuclear reactions.

Similar experiments conducted by Frier et al⁽¹⁸⁾ at the same time resulted in a detailed measurement of the multiple α -particle nuclei, C^{12} , O^{16} , Mg^{24} , Si^{28} , S^{32} in the energy region 0.6-1.8 MeV. These investigations clearly showed evidence of broad resonance structure, but the interpretation of such structure in terms of a multiple α -particle model was

not fruitful.

Numerous other researchers have contributed experimental data in the region below 3 MeV, among whom are Hibdon⁽¹⁹⁾, who has studied the cross-sections of F^{19} , Al^{27} and Ca^{40} below 500 keV with very high resolution; Cabe, Laurat and Yvon⁽²⁰⁾, P^{31} with high resolution in the range 800-1200 keV, Wills, Bair, Cohn and Willard⁽²¹⁾, F^{19} from 0.5 - 5 MeV; Stelson and Preston⁽²²⁾, Na^{23} below 1 MeV and Ricamo⁽²³⁾, P^{31} and S^{32} from 1.9 - 3.6 MeV. Virtually all of the above experimenters use as a neutron source the $Li^7(p,n)Be^7$ reaction. Previous measurements using reactor neutrons have been limited to one group, Nerenson and Darden^(24,25) who used the continuous energy reactor beam in conjunction with an energy-sensitive detector. However this technique resulted in a resolution of only $\sim 10\%$, and was clearly inferior to other experiments.

The $Li^7(p,n)Be^7$ reaction has been virtually the only neutron source for measurements of total cross-sections until recently. However this mechanism presents two limitations to an extensive systematic high resolution study. The first is that the use of monochromatic neutrons necessitates the "dialing" of an accelerator through a number of energy steps which is inversely proportional to the system resolution. The second constraint is that this mechanism can not be used above 2 MeV due to the increased branching of the decay to an excited state in Be^7 , Foster and Glasgow^(26,27) and independently

Galloway and Schrader⁽²⁸⁾, have circumvented these restrictions in the investigation of cross-sections at higher energies by using a continuous neutron source, the $\text{Li}^7(d,n)\alpha+\alpha$, and a pulsed beam time-of-flight facility. The measurements of the first group have extended the available data to 15 MeV systematically throughout the periodic table. However, this neutron source yields a spectrum peaked at ~ 10 MeV, and the tailing off of the spectrum, restricts the low energy limit of their facility to around 2.0 MeV.

The impact of these measurements on present understanding of the interaction of nucleons with nuclei has been alluded to. The initial results of Barschall et al⁽¹³⁻¹⁷⁾ led to the development of the optical model, which attempts to describe the interaction of particles by means of an average potential containing a real term, leading to scattering, and an imaginary component which results in absorption. Feshbach, Porter and Weisskopf⁽²⁹⁾ showed that such a model would predict the maxima and minima observed experimentally in cross-section measurements. Initial work was based on square well potential, and subsequent development led to improved potential shapes, by rounding the edges⁽³⁰⁾, concentrating the imaginary potential near the surface⁽³¹⁾, and adding spin-orbit coupling⁽³²⁾. Perhaps the most significant improvement in the accuracy of this model was obtained by replacing the simple average potential by a two-body non-local potential containing the usual

spin-dependent real and imaginary terms. This model, developed by Perey and Buck⁽⁴⁾, has been shown adequate⁽²⁷⁾ in predicting the average behaviour of the total cross-section from 2 to 15 MeV over the periodic table using a single parameter set.

More recent experimental work in various mass and energy regions has had similar implications in terms of nuclear theory. It was observed that many cross-sections in the region of several MeV showed resonance-like fluctuations with widths of $50 \rightarrow 100$ keV, intermediate in width to the very broad structure of the optical model and the narrow resonances characteristic of the compound nucleus system. Examples of this structure are found in the cross-section of F^{19} measured by Monahan and Elwyn⁽³³⁾ and the low resolution scattering data from F, Na, Mg, Al and P by the same authors⁽³⁴⁾. An energy-averaging of the photo capture cross-section of Al^{27} , measured by Singh et al⁽³⁵⁾ shows similar broad structure. Seth⁽³⁶⁾ has carried out measurements from 0-600 keV of seventeen medium weight nuclides, and showed fluctuations with mean width of about 75 keV. Many other examples of such intermediate structure exist; indeed this structure is evident in some of the early work previously cited.

The existence of this structure led Feshbach and collaborators^(3,12,37) to postulate a "doorway" state model. In this model, the first stage of the nucleon-nucleus interaction is by means of the optical potential. In the second stage, the incident particle interacts with a single nucleon, raising it out

of the bound state to an excited level, resulting in the formation of a 2p-1h state which gives rise to the observed intermediate structure, and which leads to re-emission, or by additional two-particle interactions to the compound nucleus.

This 2p-1h state, which acts as the "doorway" to compound nucleus formation, is labelled a doorway state. Initial investigations, which were attempts to quantify the observed data, centred about verifying the existence of such structure. Agodi and Pappalardi⁽³⁸⁾ in a study of the (n,n) and (n,p) cross-sections of P^{31} and S^{32} showed that such fluctuations lay within the limits predicted by Ericson. However Monahan and Elwyn⁽³⁹⁾ demonstrated that the statistical probability of fluctuations of this order over an energy spread much greater than the compound nucleus width was highly improbable. This analysis was performed by defining a level-order statistic which yielded the probability of n successive correlated values of the cross-section, where each value was determined over an interval much greater than the average compound nucleus width. In this manner fluctuations in the observed cross-section of Mo and Sn near 200 keV with width ~ 20 keV were shown to be statistically improbable.

One property of the doorway state mechanism is that it is a coupling mechanism between the entrance channel and the compound nucleus. Experimentally, then, if a doorway state resonance could be examined with sufficiently high resolution, it should decompose into a large number of narrow compound

nucleus resonances having the same spin and parity as the doorway state. Furthermore the fine structure resonances should have a distribution of widths and spacings quite different from the usual Porter-Thomas and Wigner distributions. Monahan and Elwyn⁽⁴⁰⁾ have performed such an analysis of fine structure observed in the cross-section of Fe between .35 and .65 MeV, a region dominated by two broad doorway states, and have substantiated these predictions.

Finally, additional theoretical calculations have been performed to evaluate neutron strength functions and neutron widths using this unified approach to the neutron-nucleus interaction. These calculations have been performed by Block and Feshbach⁽³⁷⁾, and Shakin and collaborators^(41,42).

CHAPTER III

TECHNIQUES AND INSTRUMENTATION

3.1 General Considerations

The technique used in the present work is a modification of a technique developed by Foster and Glasgow⁽²⁶⁾ and independently by Galloway and Schraeder⁽²⁸⁾. In concept, the method is one of measuring the transmission of neutrons through a sample using a white spectrum of neutrons and defining the energy by a measurement of time of flight. These experiments used the neutron spectrum obtained from the $\text{Li}^7(d,n)\alpha+\alpha$ reaction and realized the zero time required for the flight time measurement by pulsing the accelerator beam of deuterons.

In the present experiment, the fast neutron spectrum from a pool-type nuclear reactor was used as the neutron source. The zero time is defined by scattering off a fast organic scintillator, and the flight time is measured as the time difference between detection of the neutron in the scattering detector (the start counter) and detection in a second organic scintillator located at the end of the flight path (the stop counter). By utilizing the reactor as a neutron source, and by single scattering neutrons before passage through the

sample, it has been possible to investigate cross-sections in a region inaccessible to the previously mentioned experiments.

3.2 The Experiment Configuration

Figure 1 is a schematic representation of the experiment configuration. A collimated beam of ~ 1 cm. diameter emerged from a horizontal beam port of the 2 MW McMaster reactor, and scattered off the start counter labelled C1. The scattered beam passed through a slot in the shielding well, and was incident on the sample. Transmitted neutrons were detected by a second counter located at C2, after traversing a flight path of ~ 4 meters. The sample was mounted on a mechanism attached to a relay-controlled air piston, and was switched in and out of the beam at an interval of about six seconds.

3.3 The Neutron Source

The McMaster reactor is a pool type reactor, using fuel elements enriched to 90% U^{235} , and producing 2 MW (thermal). The fuel elements, consisting of thin plates of U-Al alloy clad in aluminum, are arranged in a rectangular lattice. At the nominal power of 2 MW, the thermal neutron flux in the region of the core is about 10^{13} n/cm²-sec. In addition, there is a fast-neutron flux of $\sim 10^{12}$ /cm²sec comprising "fission spectrum neutrons". Fig.(2a) is a plot of this component at

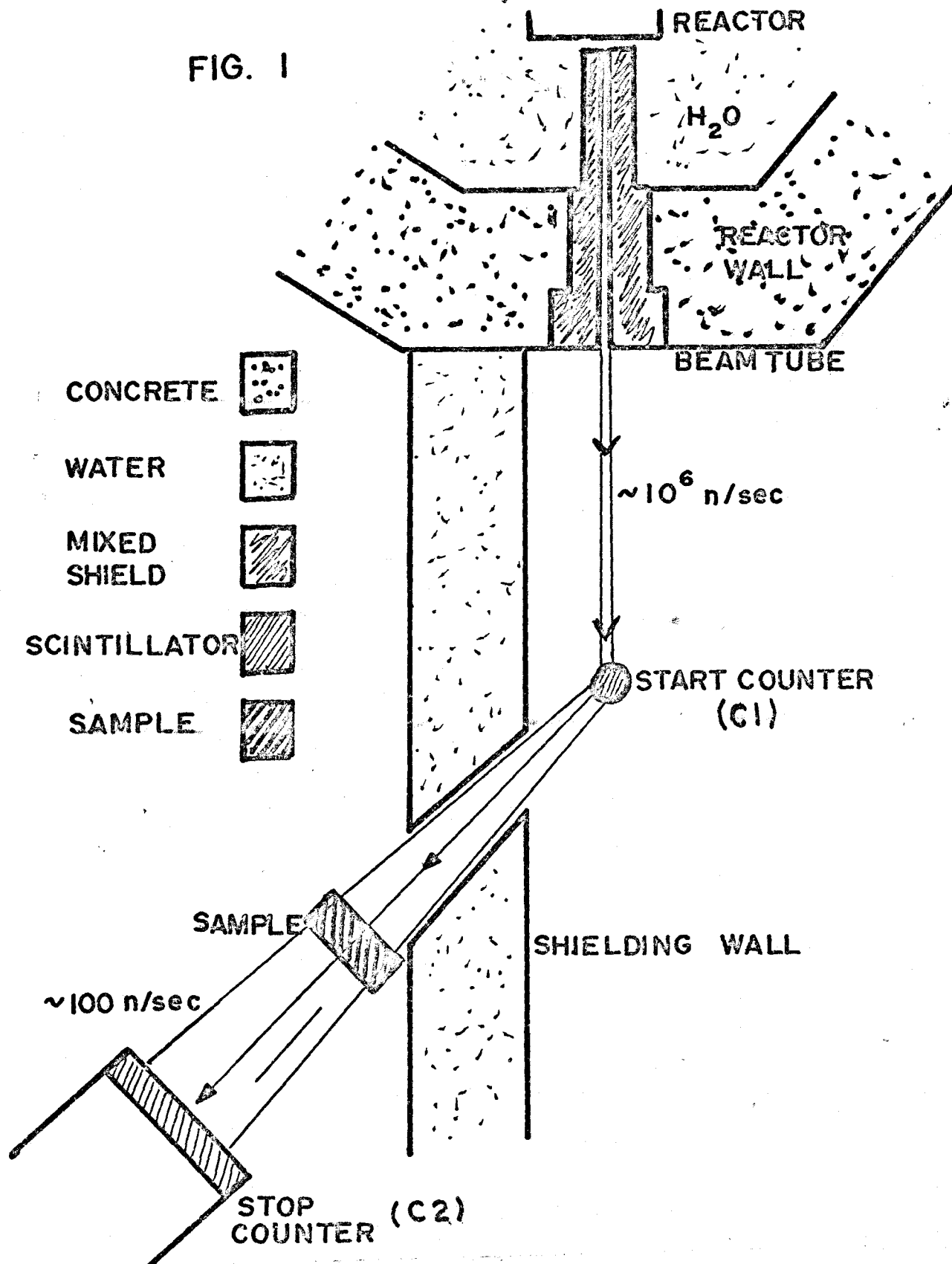
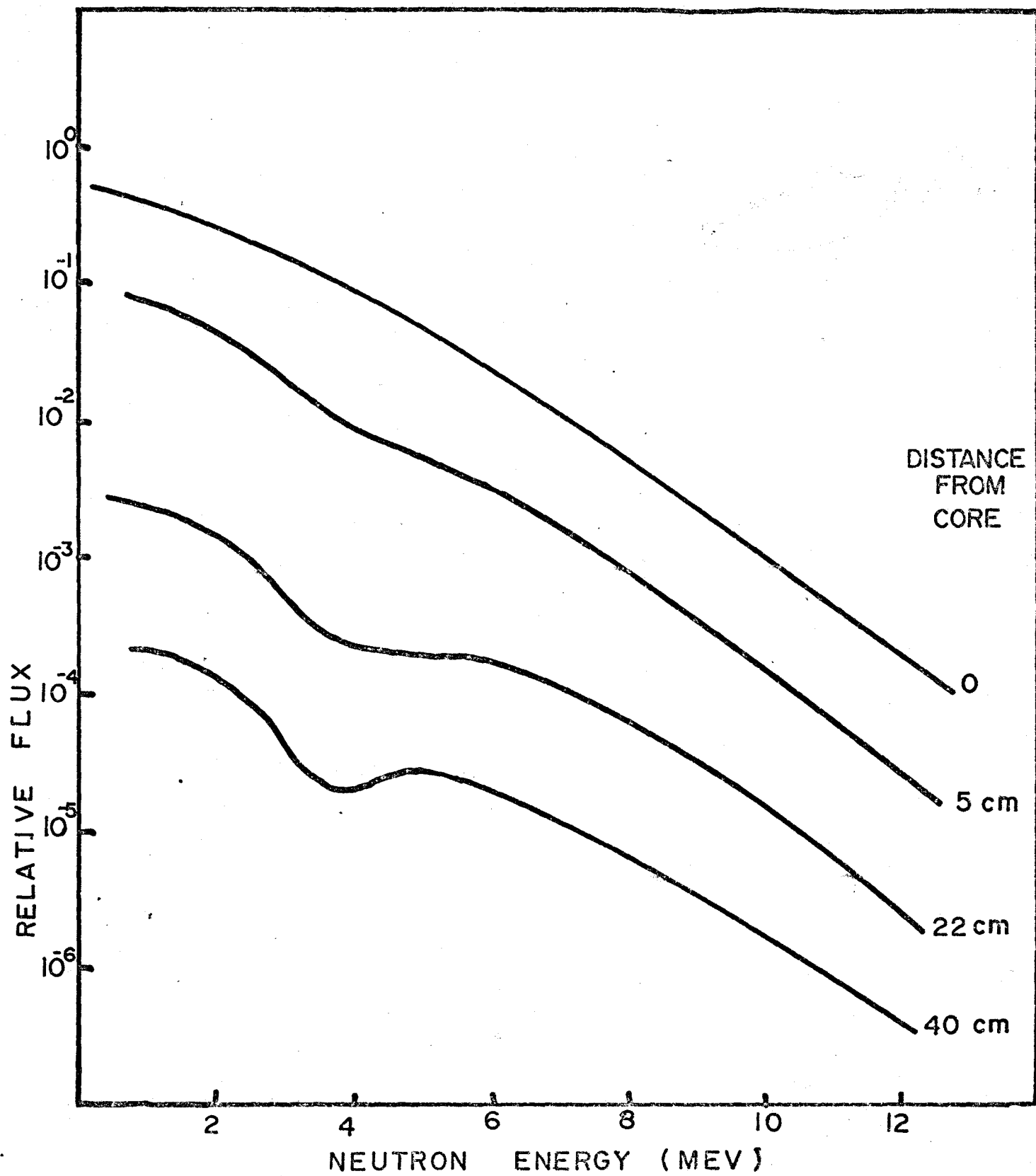


FIG.1. SCHEMATIC REPRESENTATION OF EXPERIMENT

THE INCIDENT BEAM IS SCATTERED BY THE START COUNTER, PASSES THROUGH THE SAMPLE, AND IS DETECTED BY THE STOP COUNTER 3.68 M. DISTANT

FIG.2A NEUTRON FLUX AT VARIOUS DISTANCES FROM CORE.



various locations in and around the core. The data were abstracted from Arad et al⁽⁴³⁾ and were determined using threshold detectors for a pool-type reactor similar in design to the McMaster Reactor.

Surrounding the reactor, and penetrating the shielding wall, are eight beam tubes, which are stepped from a maximum diameter of 12" at the outside of the shielding wall, to a six inch diameter at the core.

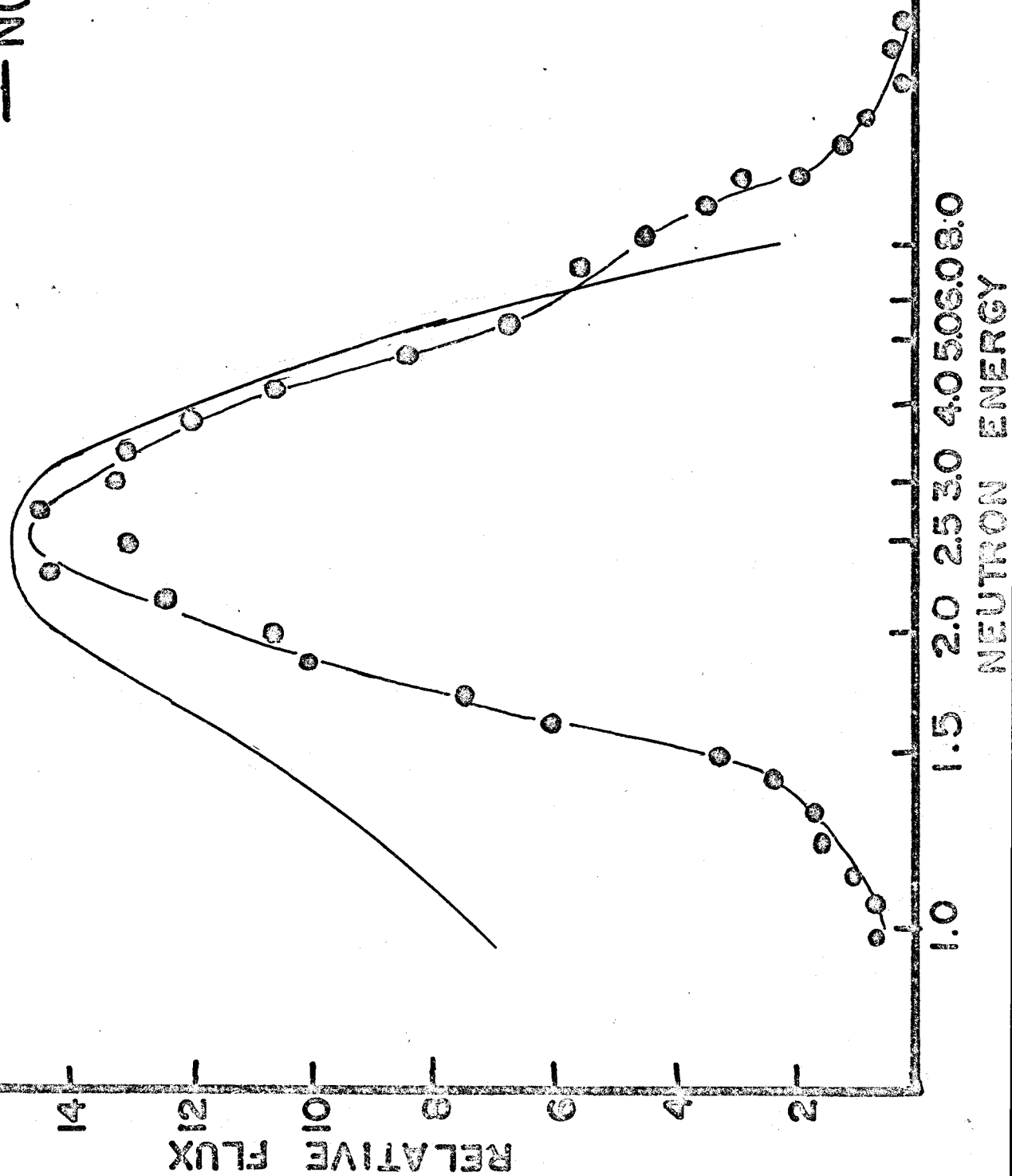
One of these beam tubes was designed and used in the present experiment. Collimators inserted in the beam tube reduced the diameter of the beam to 0.5 cm at the reactor wall, and resulted in an intensity of $\sim 10^6$ fast neutrons/sec. The collimation is described in detail in Section IIIc. To a fair approximation, the energy dependence of the fast neutron flux component of a thermal reactor can be characterized by a function of the form $\phi(E) = k\ell^{-E} \sinh \sqrt{2E}$. In the time domain, $dE/dt = cE^{3/2}$ so this function becomes $\phi(t) = k'\ell^{-E} \sinh \sqrt{2E} E^{3/2}$. Fig. 2(b) is a comparison of the neutron time spectrum obtained at the present experiment with the functional form above. No correction has been made for detector efficiency, which is reduced at low energies by the superposition of a finite pulse height threshold on the continuous pulse height response of the scintillator.

This distribution, which peaked at 2.5 MeV, was not ideal for the investigation of cross-sections in the energy range from 800 keV to 3.0 MeV. However, by scattering the

FIG.2B. NEUTRON DISTRIBUTION IN
FLIGHT TIME

CORRESPONDING NEUTRON ENERGIES
ARE PLOTTED ON THE ORDINATE.

• EXPERIMENTAL
— $N(E) = e^{-E} \sinh \sqrt{2E}$



neutron beam from the hydrogenous material of the start counter, the primary interaction, proton recoil, resulted in a scattered beam with reduced mean energy. The scattering (n,p) cross section in the lab system can be written as:

$$\sigma(\theta) \propto \cos\theta \quad (3.1)$$

and the corresponding energy of the scattered neutron becomes

$$E(\theta) = E_0 \cos^2\theta. \quad (3.2)$$

Thus by selection of scattering angle, it was possible to obtain a neutron flux distribution peaking at any energy between 0 and 2.5 MeV, within the constraints imposed by the vanishing cross-section at $\theta = 90^\circ$ and proximity to the incident beam at $\theta = 0^\circ$. A scattering angle of 45° was selected for this experiment, resulting in a flux distribution peaking at 1.25 MeV, and permitting investigation of cross-sections from 800 keV to 3 MeV.

3.4 Collimation and Shielding

3.4.1 General considerations

In comparison with shielding techniques for thermal neutrons or gamma rays, the techniques used in fast neutron shielding are considerably more arduous. For unlike thermal neutrons, which have an extremely high probability of capture in certain materials, or gamma rays, which are stopped readily with material of high Z, fast neutrons interact with about the

same probability in all materials. The situation is further complicated by the nature of the interaction, which in the range of a few MeV, is predominantly elastic or inelastic scattering. Thus even after an interaction, the neutron remains free, and in fact, if the interaction is elastic scattering, the neutron energy is only reduced by an amount equal to the recoil energy of the interacting nucleus.

The average energy loss in an elastic nuclear collision may be characterized by the parameter

$$\xi = \overline{\ln E_0/E} = 1 - \frac{\alpha \ln \alpha}{1-\alpha} \quad (3.3)$$

where

$$\alpha = \left(\frac{A-1}{A+1}\right)^2. \quad (3.4)$$

From this equation, one may calculate the average number of collisions necessary to "thermalize" a fast neutron of energy E_0 , where "thermalize" implies a final energy $E' = .025$ eV. Since the neutron energy after one collision is

$$E_1 = E_0 e^{-\xi} \quad (3.5)$$

and after n collisions is

$$E_n = (E_0) (e^{-\xi}) (e^{-\xi}) (e^{-\xi}) \dots n \text{ terms} \quad (3.6)$$

$$= E_0 e^{-n\xi} \quad (3.7)$$

then

$$n = \frac{1}{\xi} \ln \frac{E_n}{E_0}. \quad (3.8)$$

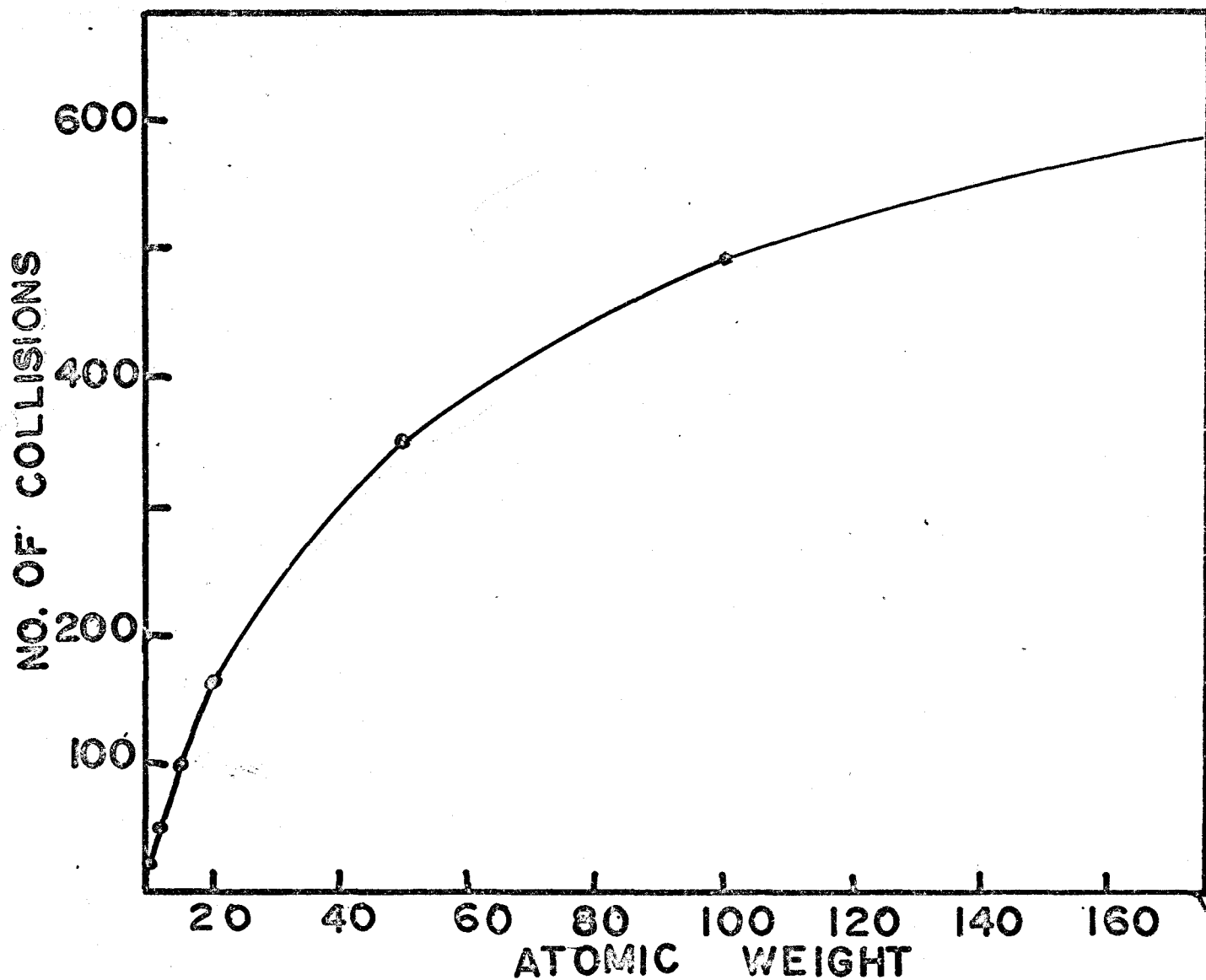
Fig. (3) illustrates the average number of collisions necessary to thermalize a 1 MeV neutron as a function of mass number. From this figure it is evident that the most rapid energy loss results from interaction with low A material. Thus an expedient choice of shielding is one containing copious amounts of hydrogen, such as ordinary water or paraffin wax. Since the thermal capture cross-section of hydrogen is large, no other material need be used, but to avoid production of the 2.2 MeV gamma ray following thermal capture in hydrogen, dopants such as boron or lithium are often dispersed in the shielding medium. For water or paraffin, the attenuation length associated with the exponential reduction of transmitted flux is ~ 5 cm for 1 MeV neutrons, thus a reduction in flux of $10^{-3} \rightarrow 10^{-6}$ requires a shielding thickness of 35-70 cm. In some applications, such as direct beam collimation in the present experiment, it was necessary to shield against both neutrons and gamma rays. In this instance lead shot dispersed in a matrix of paraffin wax, or, where structural rigidity was required, barytes concrete, containing an aggregate of Ba ore, and large amounts of hydrogen present as water of hydration was utilized.

3.4.2 Specific configuration

The shielding in the present experiment serves three principal functions:

- (1) Collimation of direct reactor beam.

FIG.3. AVERAGE NUMBER OF COLLISIONS TO THERMALIZE
A 1 MEV NEUTRON AS A FUNCTION OF ATOMIC MASS.



- (2) Biological shielding of scattered beam, from first detector and unscattered primary beam.
- (3) Shielding of second detector from room background and multiply-scattered neutron background.

These will be described separately, as there exists a physical separation of these three shielding components.

(1) Collimation of primary beam

Fig. (4) is a scale drawing of the beam collimation. The liners illustrated were located in an existing beam port. At the reactor end a cylinder of Pb, six inches in thickness, was placed on the beam tube externally to reduce the gamma radiation from the core and reduce the thickness of water to $\sim 1/2$ " between the core and the end of the beam tube, in order to decrease the thermalization of the neutron flux. The liner consisted of aluminum, filled with barytes concrete, and contained removable collimators to allow for varying beam sizes for different experiments.

The forward removable collimator reduced the beam to one-inch diameter by collimation with a paraffin, borax and lead shot structure. Beyond this collimator, there was inserted an aluminum cylinder, the forward end of which was closed by aluminum, and the opposite end welded to a $1/2$ " aluminum plate which was bolted to the wall of the reactor. This design permitted insertion and removal of inner collimators

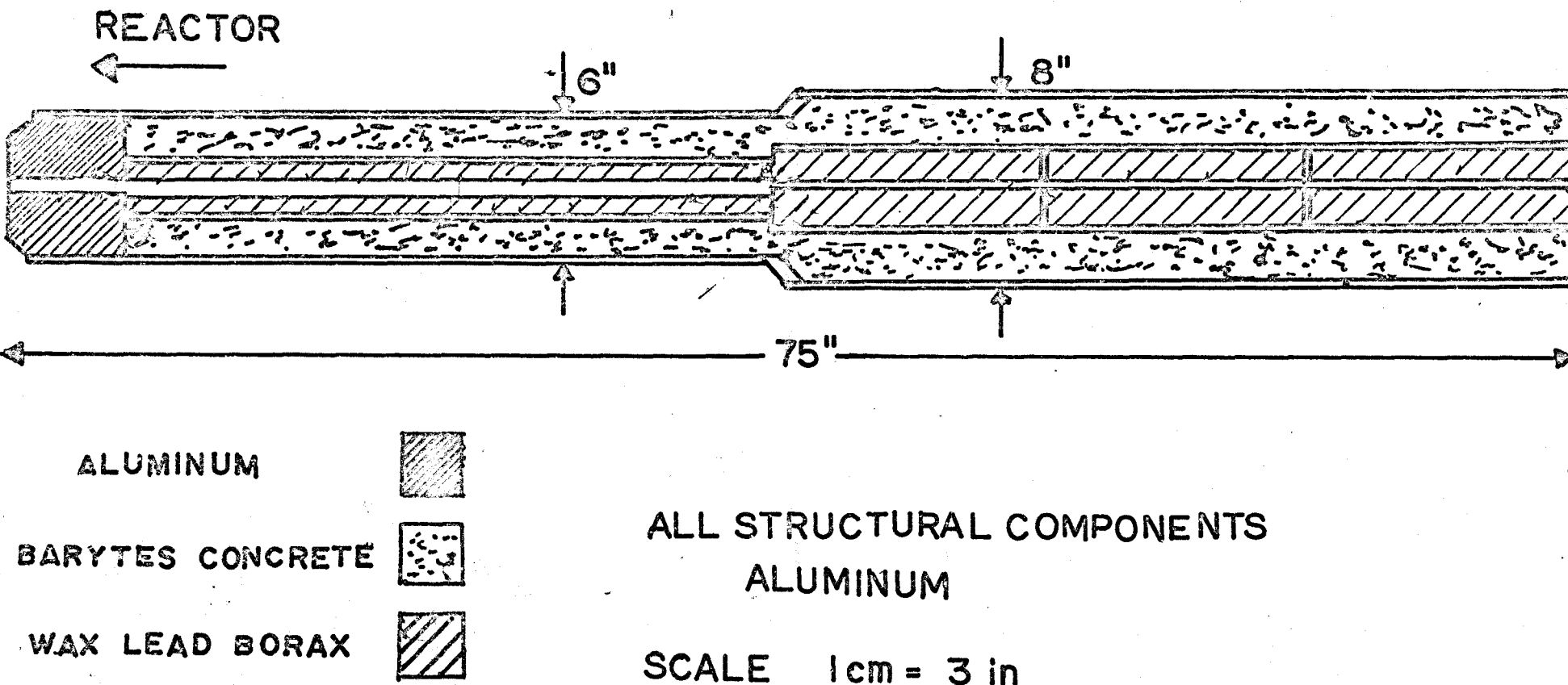


FIG. 4. SCHEMATIC DIAGRAM OF BEAM TUBE.

USED TO COLLIMATE THE INCIDENT BEAM TO 1 CM. DIAMETER

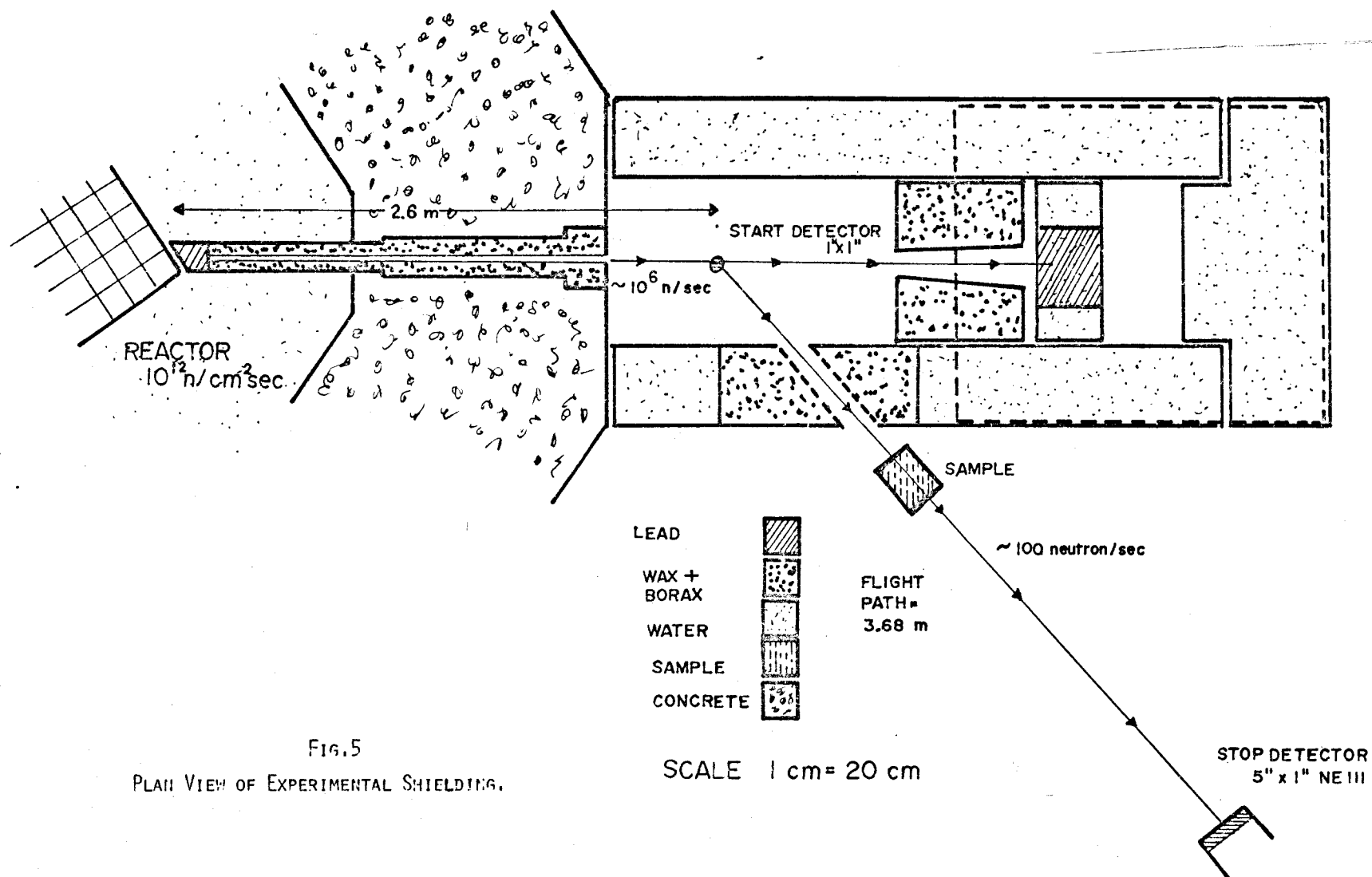
without disassembly of the beam port. Inner collimators in this tube were filled with the same mixture, and had an inner diameter of 1/4". The collimators were in three sections 12" long, with provision for attachment of a bayonet for insertion and withdrawal. Between the second and third collimators a plastic-encased LiF pad was positioned to cover the beam, absorbing any thermal neutron component in the beam.

The beam tube was provided with remotely-operated water valves for flooding to facilitate on power changes in the experimental configuration.

(2) Biological shielding

Because the beam of $\sim 10^7$ fast neutrons/sec represents a considerable health hazard, it was necessary to provide extensive biological shielding against scattered components of the beam. Two sources of scattered neutrons existed; the first detector, and the beam stop. A second consequence of this shielding was the reduction of background in the second counter from air-scattering.

Fig. (5) is a schematic plan view of the biological shielding. All components were 160 cm high, constructed of structural channel iron, with cladding of 1/8" steel plate. The outer shielding components were water-filled tanks, one of which was provided with a slot for extraction of the scattered beam. The scattered beam was accurately defined by a tapered lucite box, which fitted within the walls of the slot, the



remainder of which was filled with paraffin blocks.

The unscattered beam was stopped in a lead block of dimensions 30 cm×40 cm×40 cm located in a water-filled tank. To reduce the back-scattered radiation within the area defined by the tanks, a tapered collimator of 40 cm thickness was located ahead of the beam stop. Finally, as it was anticipated that a considerable health hazard could exist to personnel working in this area from neutrons scattered upwards from the beam stop, an additional water tank of thickness 40 cm rested on the tanks in the region shown dotted on the diagram.

The radiation levels due to neutron and gamma radiation in the region of the beam stop outside the shielding was <0.5 mrem/hr. While the radiation level above the tanks was significantly higher, providing a health hazard for prolonged exposure, this was deemed tolerable as, from the design of the reactor, it was impossible for personnel to receive a direct exposure in this direction at a distance of <5 meters unless engaged in work on this experiment.

(3) Stop-counter shielding

It was crucial to the success of this experiment to reduce background events in the second counter, because the true event rate at the second counter amounted to fewer than 100 events/sec, a natural outcome of the very low solid angle subtended by the detector at this distance.

Because of the design of the experiment, the option of increasing the primary flux to reduce true-to-chance ratio was untenable, as the probability of random "coincidences" increased exponentially with an increase in rate in the first counter. Thus a compromise existed between increased flux to increase the true event rate in the second counter, and an upper limit in the start counter determined by the rate at which the mean time between events became comparable with the neutron flight times.

Thus, having arrived at a maximum primary beam flux based on the above considerations, further improvements in background ratio were effected only by improvements in shielding of the second counter.

The shielding configuration which evolved consisted of a rectangular box of lead, 2.5 cm thick, 90 cm long, in the middle of which was located the scintillator, with the photomultiplier extending backwards and enclosed by the shielding. In the scintillator area, a graded shield of tin and copper was affixed to the interior walls of the box, and additional lead shielding was placed on the exterior of the box.

Surrounding the box were paraffin sheets to a total of 15 cm thickness in all directions, for the purpose of neutron shielding.

Thus the shielding acted as a crude collimator, restricting direct viewing of background radiation to a small

cone at the forward end of the collimator.

The entire configuration was mounted on a movable table to permit experiment changes without dismantling.

This arrangement resulted in a reduction of background events by one-to-two orders of magnitude, compared with an unshielded configuration.

3.5 The Detector

3.5.1 Choice of detector

The experimental conditions encountered in neutron time-of-flight spectroscopy impose stringent restrictions on the neutron detector requirements. These are:

(1) Ultra fast decay time. To achieve reasonable energy resolution with realistic flight paths, the time resolution of the detection system must be of the order of a few nanoseconds. This implies a detector response with rise time of this order.

(2) High efficiency. Because of the low solid angle subtended by the second counter the system efficiency is low, and effort must be made to maximize the neutron detection efficiency by selection of high efficiency detectors, short flight paths (within energy resolution restrictions) and large detector solid angles.

Thus the intrinsic efficiency of the detection material for neutrons must be high and the detector must be

capable of fabrication in large physical dimensions. These considerations are best met by a large class of light-emitting materials broadly known as organic scintillators. Historically the first examples of these were the organic crystals anthracene and stilbene, but these have since been supplemented by a large variety of organic-based scintillators in both liquid and solid solution.

The majority of time-of-flight experiments have utilized a scintillating liquid NE213 which has the specifically useful property that the decay times of the phosphor for neutron and gamma ray interactions are significantly different, thus it is possible to discriminate against gamma ray events on the basis of pulse shape. However it has been shown that for neutron energies < 2 MeV existing pulse shape discrimination circuits are impractical. Therefore it was decided from the outset to not employ pulse shape discrimination, and the selection of phosphor was based solely on low decay time and convenience in application. The material chosen was NE111, a plastic scintillator manufactured by Nuclear Enterprises Ltd., characterized by a phosphor decay time of ~ 1.5 nsec.

3.5.2 Nature and Characteristics of Detection Mechanisms

The primary interaction of neutrons in the scintillator is proton recoil, which is highly favoured by the 67% atomic abundance of hydrogen in the organic material. An energy from

0 to the neutron energy is transferred in the interaction, the magnitude depending only on scattering angle. The proton energy is then dissipated in ionization, creating metastable states in the phosphor which ultimately decay by light emission with a mean decay time of the order of 1 nsec.

The scintillator is optically coupled to a fast photomultiplier. Light from the phosphor released ~ 100 photoelectrons/MeV electron energy from the cathode. These are amplified by the dynode chain and result in a charge pulse of the order of 10^{-10} coul/MeV at the phototube anode.

3.5.3 Characteristics of the Neutron Response

In discussing the detailed response characteristics of the scintillator, consideration must be given to 1) efficiency, 2) pulse height response, and 3) time response.

1) Efficiency

For a detector of dimensions large compared with the mean free path of recoil protons, the efficiency of the detector is primarily determined by the probability of a neutron-proton scattering event. This may be expressed as⁽⁴⁴⁾:

$$N_1(E_0, L) = N_0(n_H \sigma_H) L(1 - (e^{-aL})) / aL \quad (3.9)$$

where N_1 = no. of proton events/cm²

E_0 = neutron energy , N_0 = neutron flux

L = thickness of detector

n_H, σ_H = no. of hydrogen atoms/cm³, hydrogen cross section
at E_0

$$a = n_H \sigma_H + n_C \sigma_C. \quad (3.10)$$

A graph of this efficiency for a detector of 1" thickness is shown in Fig. (6). The curve is not regular because of the fluctuations in the carbon cross-section, but indicates an efficiency of ~ 0.5 for the second counter at all energies of interest. The calculation assumes no multiple-scattering, and no loss of efficiency by edge effects, and ignores the important consequence of a finite detection threshold on the detector efficiency. This last effect would serve to reduce the efficiency significantly at low neutron energies by an amount dependent on the threshold.

2) Pulse height response

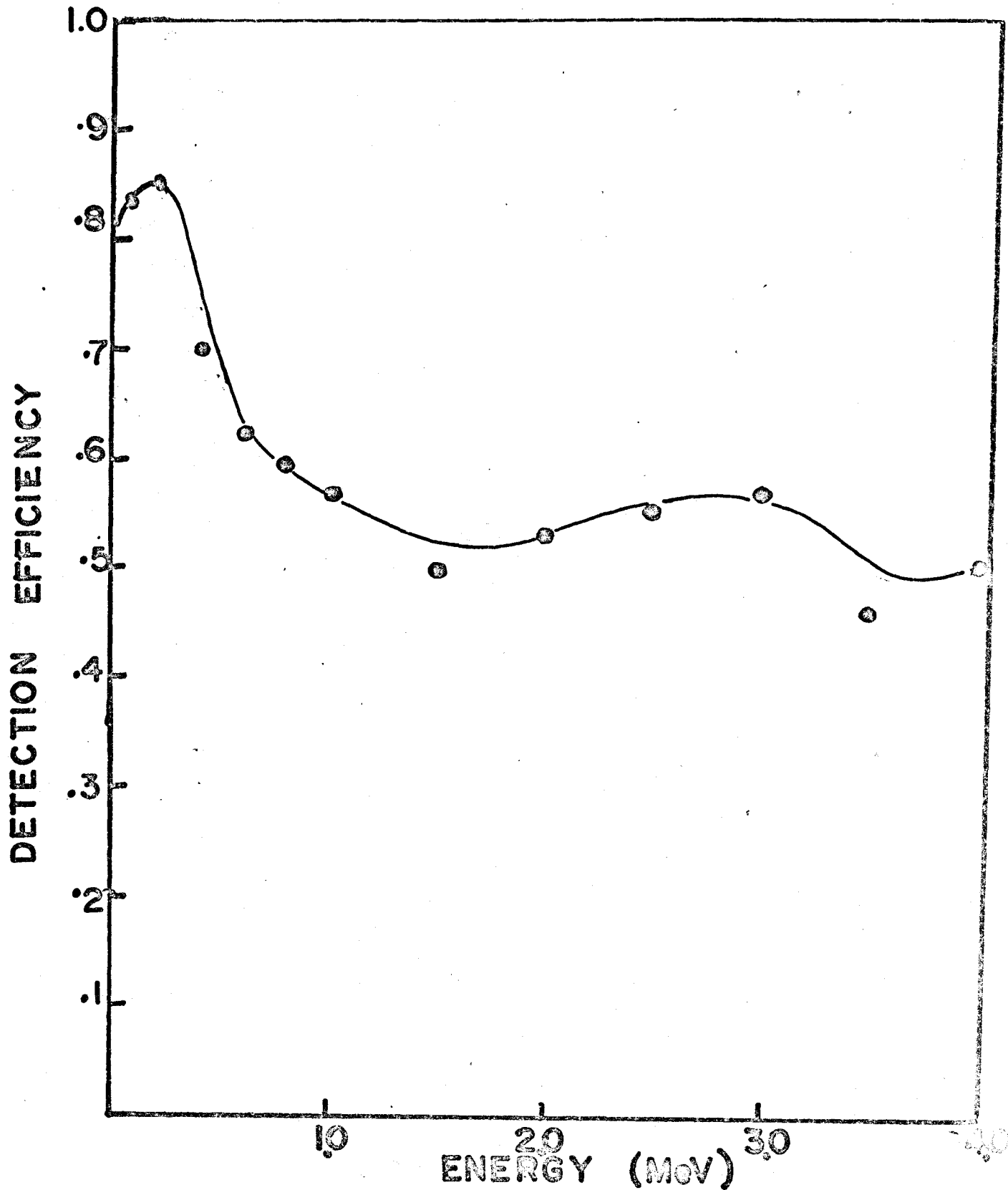
Because the elastic scattering cross-section of hydrogen is isotropic in the center of mass for the energy region under consideration, a monoergic neutron source interacting in a hydrogen scintillator results in a distribution of proton energies of the form

$$\begin{aligned} N(E_p) dE &= \frac{N_0}{E_0} dE & E &\leq E_0 \\ &= 0 & E &> E_0 \end{aligned} \quad (3.11)$$

However because the scintillation efficiency is not linear with energy as a result of the high ionization density

FIG.6

EFFICIENCY OF ORGANIC SCINTILLATOR.
FOR A DETECTOR OF 2.5 CM. THICKNESS, AS A FUNCTION OF
NEUTRON ENERGY.



of the recoil proton, this equation does not adequately describe the pulse height response of the scintillator. The pulse height response will be discussed in detail in subsection 5.

3) Time response

Four distinct processes contribute to the time resolution of the detector system. These are:

- (1) Variation in transit time of the neutrons before interaction in the scintillator.
- (2) Statistical fluctuations in the pulse height response of the signal at the output of the photomultiplier.
- (3) Time spread resulting from the continuous pulse height response of the (n,p) interaction in the scintillator.
- (4) Variations in transit time across the face of the photomultiplier tube.

The first may be regarded as an uncertainty in the flight path. Since the initial beam has a diameter < 1 cm, this uncertainty is generated primarily by the "stop" counter, and is expressed as

$$\frac{\Delta(t)}{t} \approx \frac{x}{D} \quad (3.12)$$

where x = scintillator thickness

D = flight path.

This equation assumes the mean path of neutrons in the scintillator $\lambda \gg x$. By restricting the thickness of the stop counter

such that x/D is less than the errors arising from sources (2) and (3) above, this uncertainty may be minimized.

The second phenomenon, statistical fluctuations in pulse height response, originates in the quantum nature of the interaction. Let us consider a single recoil proton of energy E_0 and further assume a constant energy E_I required to excite a metastable state in the phosphor. Then in the ideal case:

$$E_0 = nE_I. \quad (3.13)$$

Because of the statistical nature of the process, the true energy transferred to metastable states has the form of a gaussian probability function with mean E_0 and $\sigma = F\sqrt{n} E_I$.

The factor F is the Fano⁽⁴⁵⁾ factor, $1 < F < \infty$, which is an expression of the probability of an ionization event resulting in the formation of a metastable state, with detectable light output. The design of a scintillating phosphor is intimately related to the existence of trapping centres within the phosphor medium, from which light emission may occur with low probability of reabsorption. Because the density of these trapping centres is low, relatively few ionizations will result in the formation of a metastable state in a trapping site. Thus the Fano factor in a scintillator, $F \gg 1$.

This process is not the only statistical process existing in the transformation from neutron energy to electric charge pulse, however. In fact, in the above process, the number

of metastable states produced, $n \approx 10^4/\text{MeV}$, so the spread in pulse height on this basis is only of the order of 1%. The dominant process is the transformation from light in the scintillator to photoelectron emitted at the cathode of the photomultiplier tube, which is governed by the Einstein equation. Thus:

$$E_o = nE_I = n'(E_p + E_\infty) \quad (3.14)$$

where E_p = kinetic energy of photo electron

E_∞ = threshold for emission of photo electron.

MacDonald and Gedke (46) have indicated a figure of $n'/E_o \approx 110$ electrons/MeV equivalent electron energy for the XP1040 phototube. Hence a 1 MeV proton, whose equivalent electron energy is ~ 200 keV will release on the average ~ 22 photoelectrons.

The pulse height resolution is therefore $\frac{\sigma}{P} = \sqrt{n}/n = 0.21$.

Thus, a monoenergetic proton interacting in the scintillator results in a response function gaussian in shape whose standard deviation, σ , is of the order of 20% of the pulse height.

The situation is further complicated by the kinematics of the knock on process previously outlined, in which a single neutron energy results in a proton ranging in energy from 0 to the neutron energy.

Both these variables in the response function are evident as "walk" in the time response of the detector - that is to say a variation in the apparent detection time of the neutron

which is a function of the resulting pulse height. This comes about as follows.

The risetime of the output signal is the time required to collect the charge pulse resulting from amplification of the photoelectrons emitted at the photocathode. Neglecting other effects inherent in the phototube, this time is just the integral of the phosphor decay time. This may be described as

$$N_{\ell}(t) = k\mu\ell^{-\mu(t-t_0)} \quad (3.15)$$

t_0 = time of arrival of neutron

μ = phosphor decay const.

$N_{\ell}(t)$ = number of photons at time t

thus

$$C(t) = k(1 - \ell^{-\mu(t-t_0)}) \quad (3.16)$$

$C(t)$ = charge collected at cathode.

The pulse height dependence, therefore, of the rise time function is incorporated in the constant k . Normally, to utilize these pulses for time analysis it is desirable to convert them to a logic signal of fixed amplitude and rise time. Until recently the conversion was accomplished by sensing the time at which the pulse reached a certain level, and at this time, generating a logic pulse. It is this process which results in the transformation from non-unique pulse height response, to finite time resolution. This is illustrated in Fig. (7). The problem may be circumvented by

FIG. 7. ILLUSTRATION OF TIMING WALK.

THE UPPER PORTION OF THE DIAGRAM SHOWS THE DETECTION THRESHOLDS D1,D2,D3 SUPERIMPOSED ON TWO PULSES P1,P2.

THE LOWER PORTION SHOWS THE LOCATION IN TIME AT WHICH LOGIC PULSES ARE GENERATED FOR THE TWO PULSE HEIGHTS AT EACH DISCRIMINATOR LEVEL.

FIG. 7

DECAY CONST = 1.0 nsec

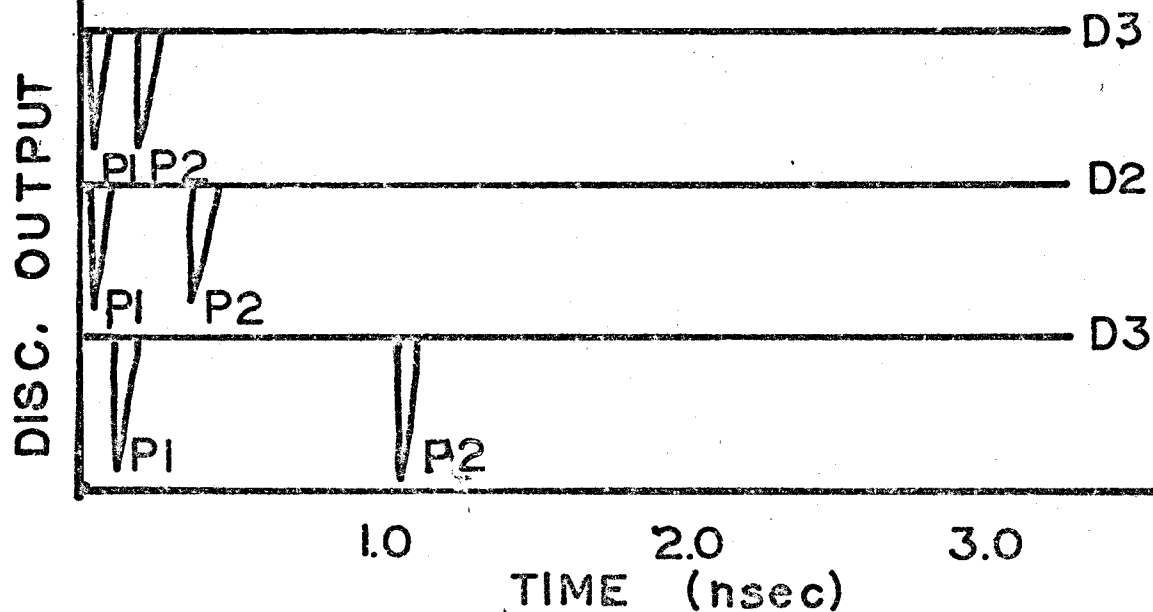
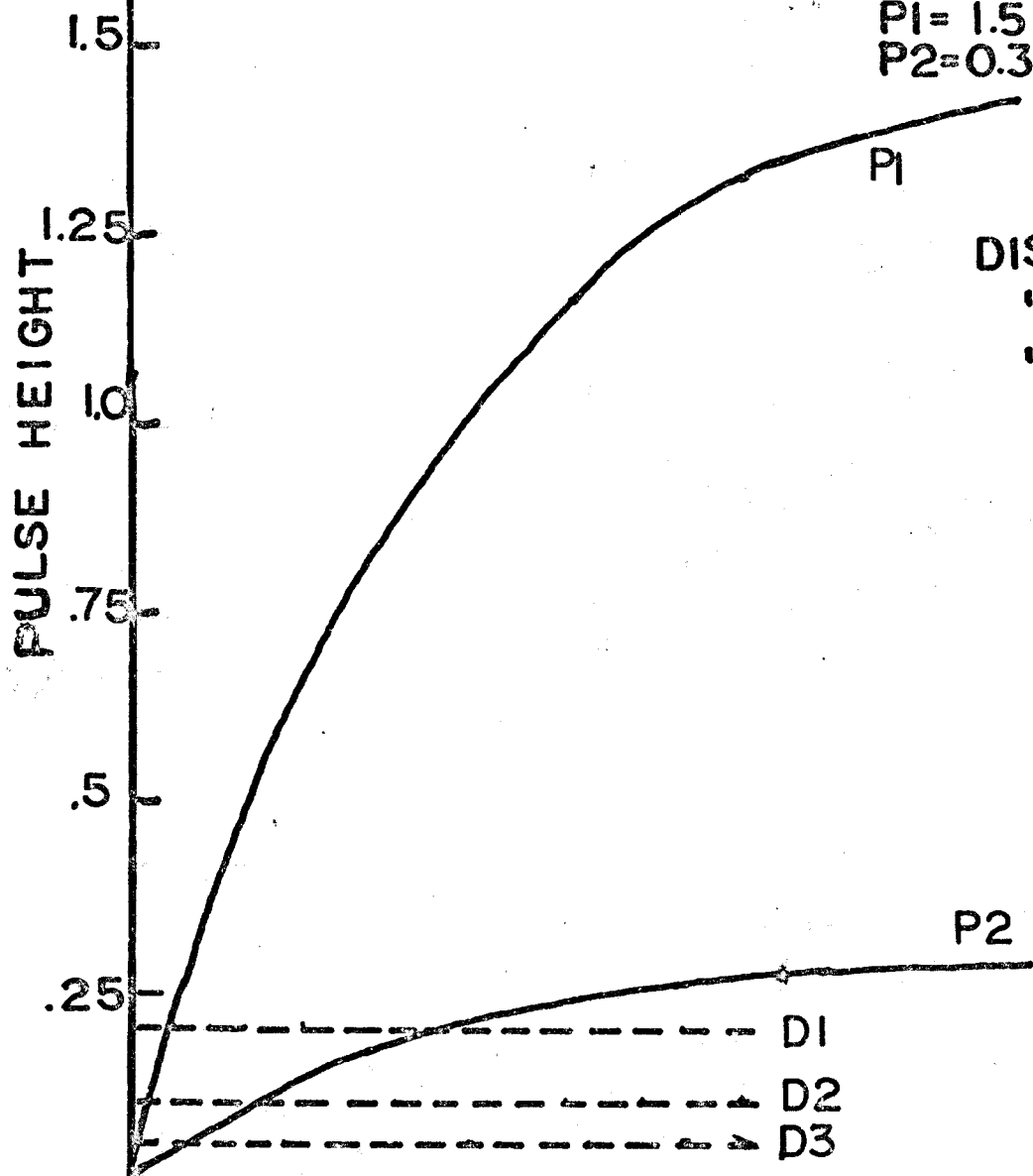
P1 = 1.5 V

P2 = 0.3 V

DISC LEVEL 1 = 0.2 V

" " 2 = 0.1 V

" " 3 = 0.05 V



using a pulse sensing circuit which triggers at a constant fraction of the pulse height, but in the present experiment it was decided to correct for this in a different manner by shifting time spectra of constant pulse height to compensate for the walk, at the time of data analysis. This will be described in detail in a later section.

In theory at least, with the availability of pulse height information, it should be possible to reduce this walk effect greatly, although the large dynamic range of the proton response makes the problem a difficult one.

One source of time spread remains; that is the variations in transit time with position on the photocathode face. MacDonald and Gedke⁽⁴⁶⁾ have determined this variation using a light pulser and scanning across the face of the tube. Their results are shown in Fig. (8) and indicate that the time resolution from this effect would be of the order of $\sigma_{tr} \sim 0.4$ nsec.

Fig.(9) is abstracted from the results of MacDonald and Gedke⁽⁴⁶⁾ and illustrates the overall system resolution obtained with an XP1040 tube, for a constant triggering level of $f = 0.1, 0.2$ and 0.4 at 1 MeV proton energy. The proton energy is plotted on the ordinate.

These time resolution curves have been obtained by recording time response as a function of pulse height in a

FIG.8.VARIATION OF TRANSIT TIME WITH RADIUS.

TIMES SHOWN ARE ELECTRON TRANSIT TIMES FOR XP1040
PHOTOTUBE RELATIVE TO MINIMUM VALUE.

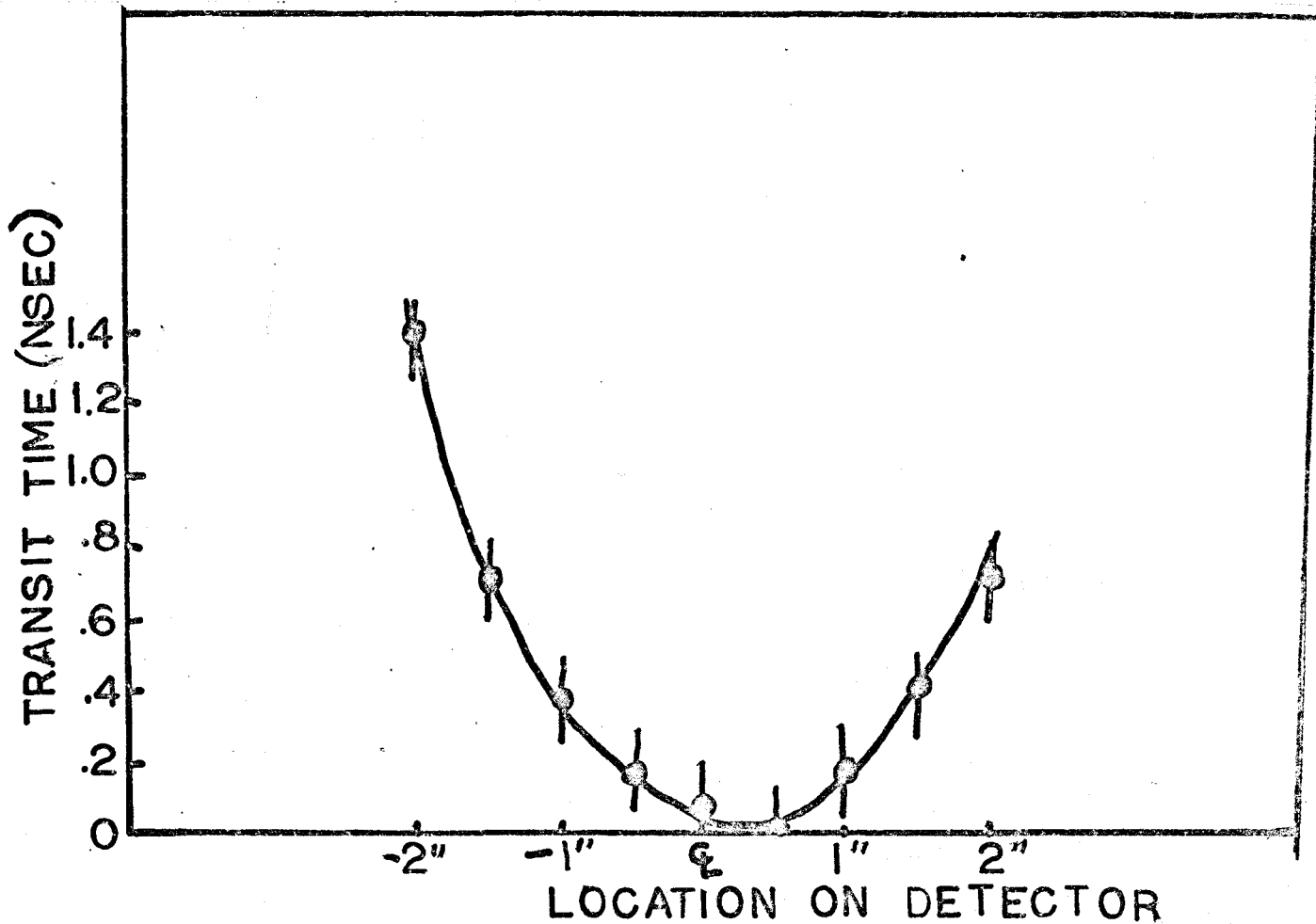
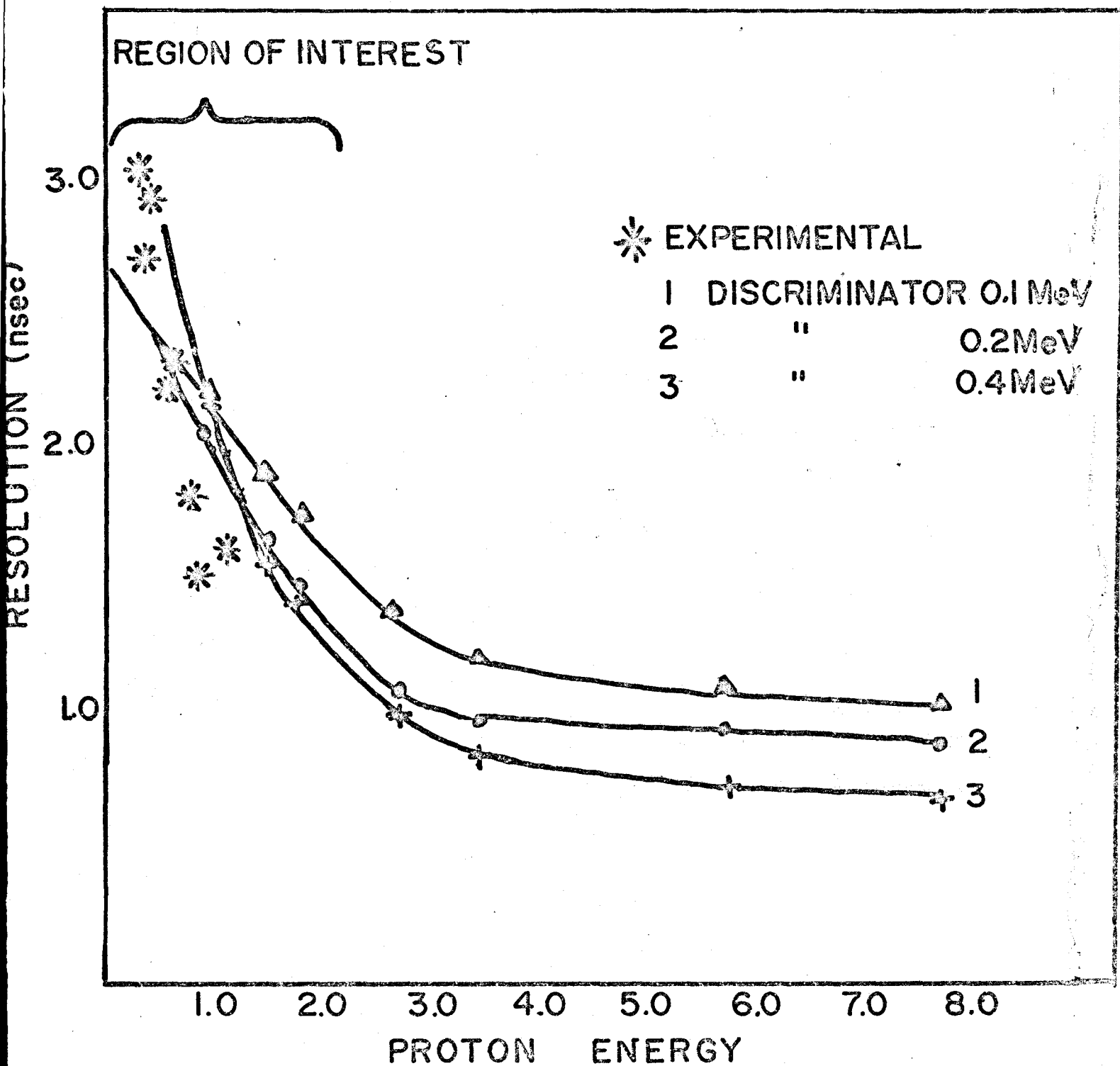


FIG.9.

OVERALL RESOLUTION OF STOP COUNTER.

CURVES ARE SHOWN AS A FUNCTION OF PROTON ENERGY
AND DISCRIMINATOR LEVEL. EXPERIMENTAL POINTS ARE SHOWN
AS X's.



two dimensional array, hence no walk effects are present in this determination. A similar approach was utilized in the present experiment, as will be described.

From these data, it was concluded that in the region of pulse heights encountered in the present experiment, time resolution had low dependence on triggering level, but the trend, evidenced by the variation in slopes, would yield a better result from low triggering levels. For this reason, and to maximize system efficiency, discriminator levels were set as low as possible commensurate with noise levels.

3.5.4 Application to experiment

From the configuration of the experiment, in which the scattering angle in the first detector is defined by the location of the second counter, it is evident that for the first counter the response function to a neutron of energy E_0 is no longer a continuum from 0 to E_0 , but is peaked at some pulse height corresponding to the monoenergetic proton recoil energy. Thus, since a unique correspondence exists between neutron energy (hence flight time) and pulse height, the walk function is restricted to the range of pulse heights defined by the counter resolution. Furthermore, the scintillator is of small dimensions, thus transit time variation is relatively low. And finally the photomultiplier used is extremely fast (RCA8575). These properties indicated that the second counter is responsible for the majority of the system resolution.

Efforts were therefore concentrated on maximizing the time resolution of the second counter.

To eliminate walk effects, the time spectra were recorded in coincidence with pulse height in the second counter. These time spectra were then shifted an amount equal to the variation in position of the prompt gamma ray peak appearing in each spectrum.

The time response was determined accurately to compare with the existing data, by conducting an experiment in which an Na^{22} source was placed in contact with the first detector. Analysis of this run yielded information about the timing walk as a function of pulse height, and the variation in system resolution as a function of pulse height. Fig.(10) is a plot of the prompt peak as a function of pulse height; the two-digit numbers on the right hand side represent the channel numbers in the pulse height dimension of the array.

If we assume the rise time of the charge pulse to have the form $C(t) = (1 - e^{-\mu(t-t_0)})$, it may be shown that the apparent time of an event can be expressed as:

$$(t-t_0) = \ln(1-F)/\lambda \quad (3.17)$$

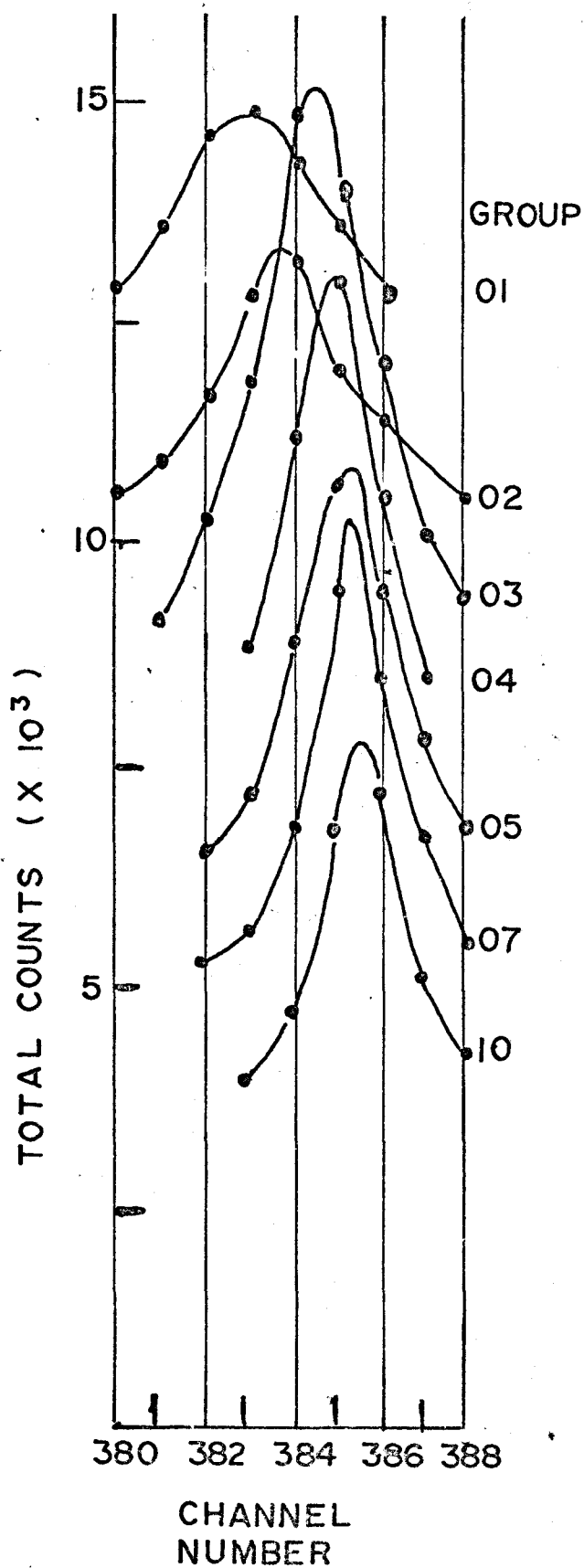
where $F = D/y$ - ratio of disc. level to maximum pulse height

λ = decay time of phosphor.

It has been found that using this expression with values of $\lambda = 5$ nsec and $D = y$ where y = group number, provides an excellent fit to the experimental walk function. This curve

FIG. 10

ILLUSTRATION OF PROMPT PEAK
FUNCTION OF PULSE HEIGHT
SHOWS THE CHANGE IN RESOLUTION
WITH PULSE HEIGHT, AND THE PULSE
HEIGHT-DEPENDENT "WALK FUNCTION"



GROUP	RESOLUTION (nsec)
01	3.3
02	3.0
03	3.2
04	2.5
05	2.6
07	1.7
10	1.8

is illustrated in Fig. (11).

As was indicated earlier, a property of the neutron distributions has made it possible to determine the energy calibration of the pulse height spectrum from the second counter . For a particular pulse height bin, it was assumed that event pairs (flight time-pulse height) occurred for all neutrons for which the maximum energy of recoil proton corresponded to a pulse height greater than or equal to the equivalent pulse height of the bin. Thus, the low energy limit in the time distribution was exactly equivalent to the pulse height of the bin. And since the low energy limit was known precisely, the pulse height scale was calibrated. The results of this calculation are shown in Fig. (12).

Finally, the resolution of the stop counter as a function of pulse height was investigated, to compare with the previous results cited. These data were obtained simply by measuring the widths of the prompt peaks in the Na^{22} experiments⁽⁵⁾. The results are plotted as asterisks on Fig. (9) previous, and show good agreement with the previous results.

3.6 General Considerations of Experiment Design

Before discussing the configuration, and the components of the experiment, it is necessary to delineate the rationale underlying some of the procedures. Specifically, detailed analysis must be given to choice of:

Fig.11.

TIMING WALK FUNCTION OF PULSE HEIGHT

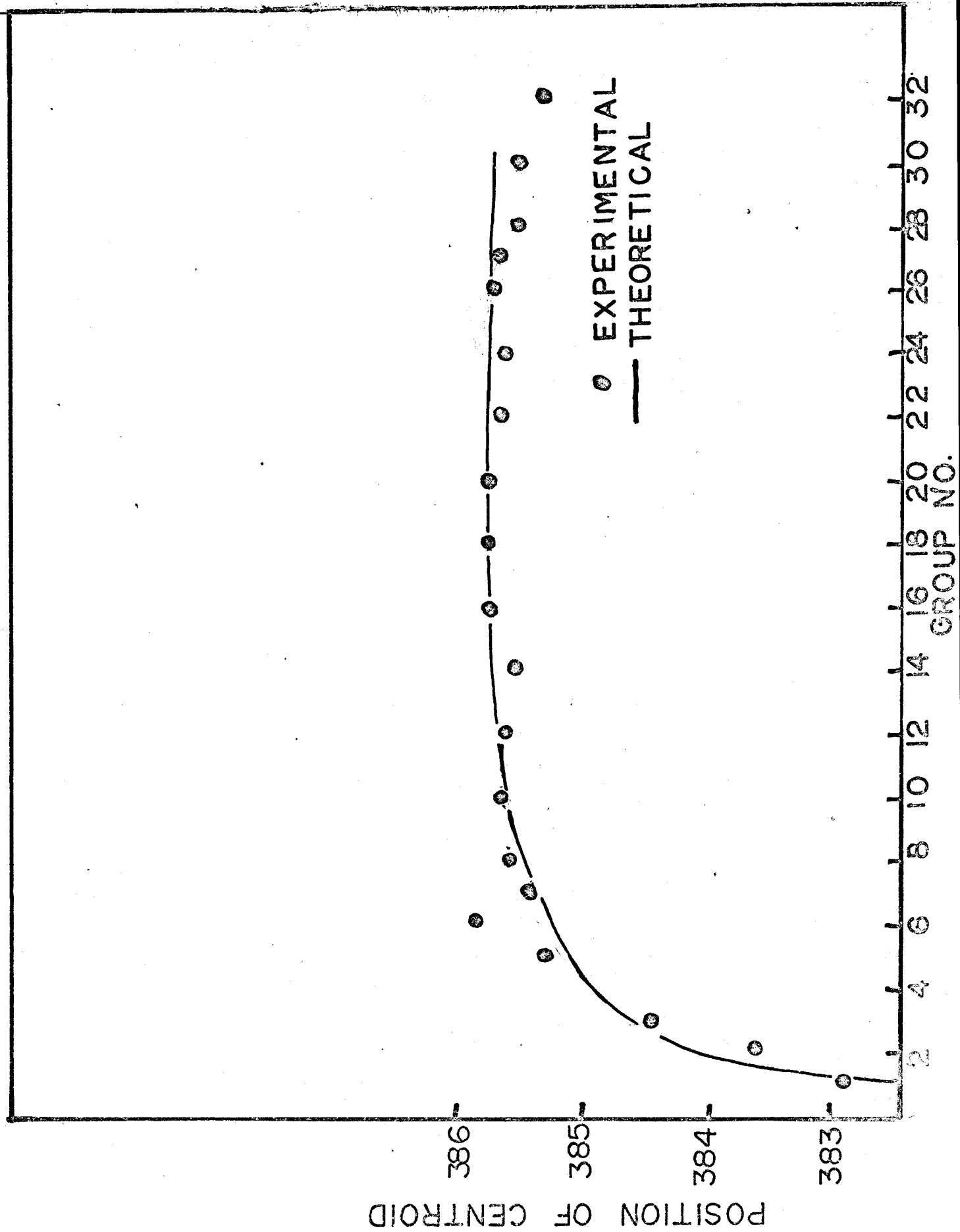
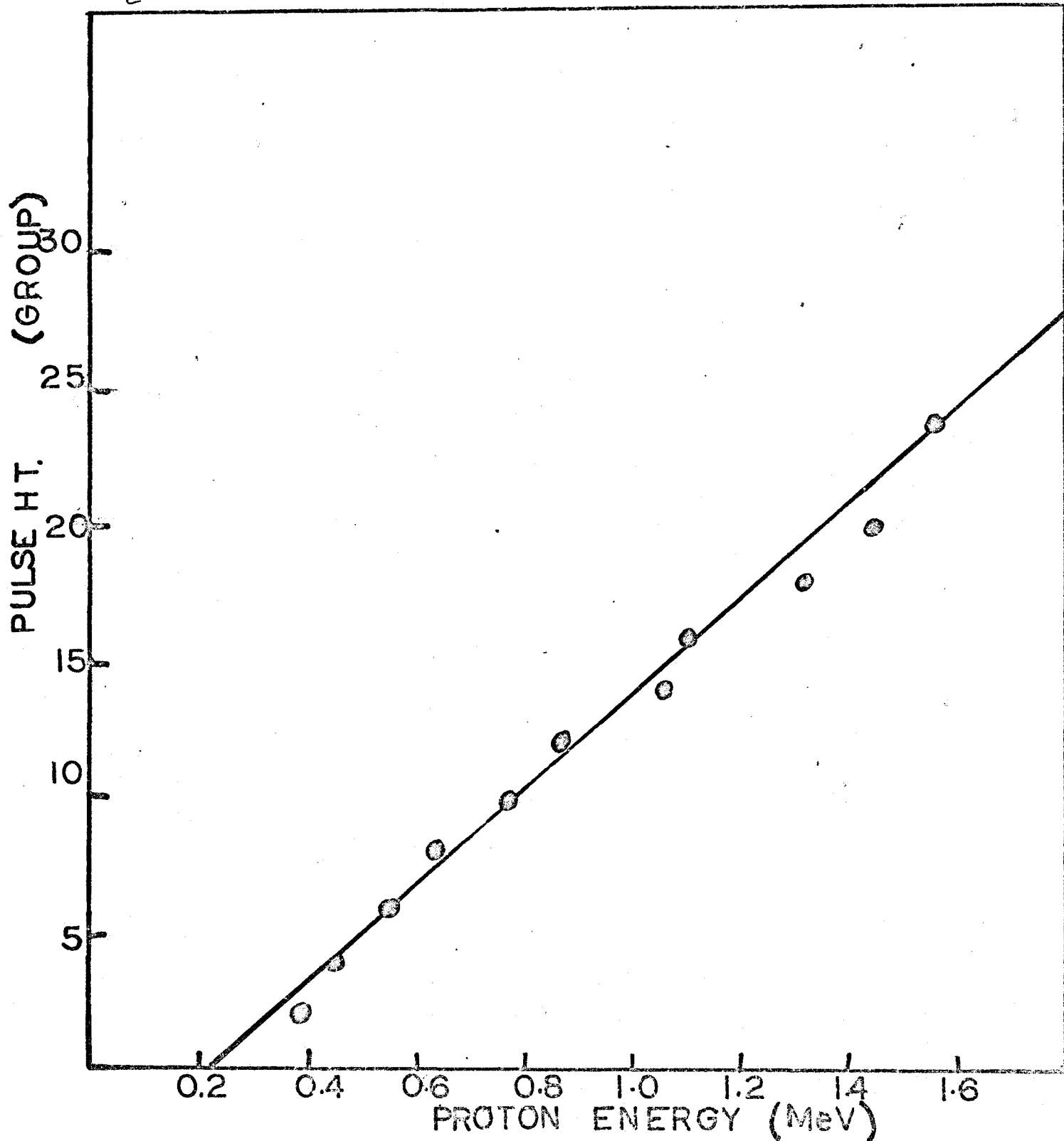


Fig.12

CALIBRATION-PULSE HEIGHT VS. PROTON ENERGY

PROTON ENERGIES ARE DETERMINED FROM THE LOW ENERGY CUT-OFF OF THE NEUTRON TIME DISTRIBUTION, AND PULSE HEIGHTS ARE THE CORRESPONDING GROUP NUMBER



- (1) Sample thickness.
- (2) Sample in and out times.
- (3) Time reversal of start and stop counter.
- (4) Sample placement.

The choice of optimum sample thickness and optimum sample in and out times are both related to certain other parameters of the experiment, primarily the ratio of signal to background.

Foster and Glasgow⁽²⁶⁾ have analysed this optimization in detail, expanding on a theory developed by Bratenahl et al⁽⁴⁷⁾. These results are presented below, and modified in light of the present experimental design.

For a pure sample, with a relative background ratio b , expressed as a fraction of the rate of true events, a sample of thickness y , mean free paths, and a fraction f of the total running time devoted to measuring the unobstructed beam, the optimum choice of sample thickness is a solution of the coupled transcendental equations:

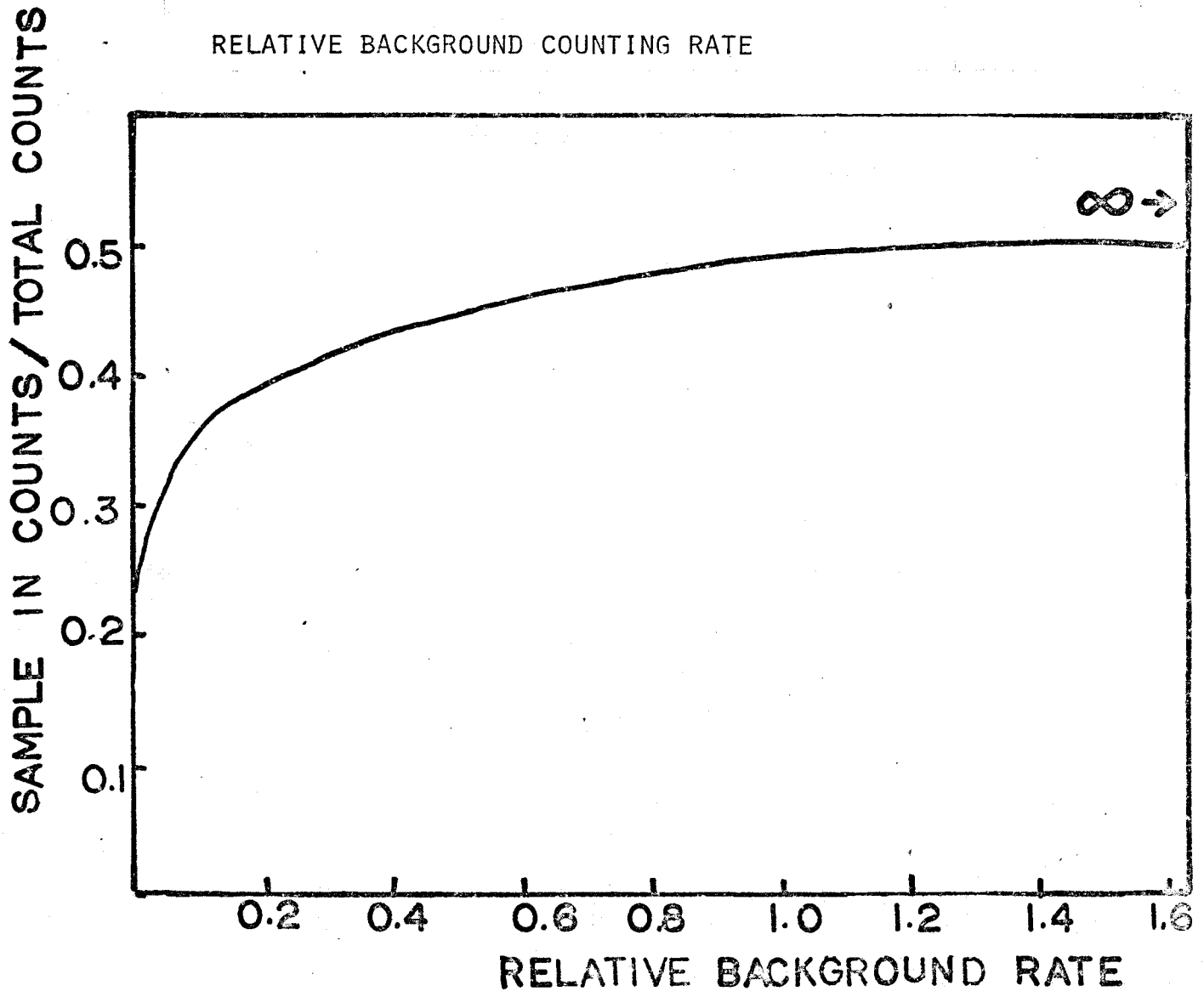
$$\frac{2}{y} = \frac{1+2b\ell^y}{1 + b\ell^y + \frac{f(1+b)}{(1-f)\ell^y}} \quad (3.18)$$

$$\frac{f}{1-f} = \frac{\ell^y + b\ell^{2y}}{1 + b\ell^y} \quad (3.19)$$

Fig.13

OPTIMIZED ACCUMULATED COUNTS SAMPLE IN AND OUT

THE RATIO OF THE OPTIMUM NUMBER OF EVENTS WITH SAMPLE
IN PLACE TO THE TOTAL NUMBER OF EVENTS AS A FUNCTION OF
RELATIVE BACKGROUND COUNTING RATE



In the present experiment, sample in and sample out times are determined by the time required to fill a 384 word buffer memory in the pulse height analyser. Thus the criterion of optimum times must be transformed to a criterion of relative number of events accumulated in the sample-in and sample-out positions. Fig. (13) is a graph of these relative accumulated sums as a function of relative background rate, obtained by multiplication of sample in time by the transmission factor e^{-Y} , and renormalizing. These results indicate that for zero background, approximately 20% of the total accumulated counts is devoted to sample-in counts and this fraction rises rapidly to about 50% for large background. In the present experiment, the relative background rate is $\sim 25\%$, and for this ratio, the optimum sample in total accumulated count rate is $\sim 40\%$. Implicit in this derivation is the assumption that the background is not attenuated by the sample, an assumption valid in the present experiment in which the background arises chiefly from random coincidences between neutron events in the start counter and events due to room background in the stop counter.

Reference to Fig. (13) indicates an optimum sample thickness of about 1.5 mean free paths for the present experiment configuration.

Location of sample

One correction which must be applied to cross-section measurements obtained by transmission is the so-called "in scat-

tering" correction; that is the measured cross section will differ from the actual cross section by an amount corresponding to small angle scattering of neutrons into a detector of finite solid angle by a sample of finite dimensions. The exact calculation of the amount of this correction will be deferred to the discussion of data analysis, but this correction has an influence on experimental design in that the magnitude of the correction may be minimized by an appropriate choice of sample location relative to the neutron source and neutron detector.

It can be shown⁽⁴⁸⁾ that the intensity at the counter position due to all singly scattered neutrons is expressed as:

$$I_1 = \frac{\pi Q}{4} \left(\frac{dL}{L_1 L_2} \right)^2 n t \sigma_n(0^\circ) e^{-nt\sigma_T} \quad (3.20)$$

where Q = flux in direction of detector/unit solid angle/sec.
 $L = L_1 + L_2$
 $\sigma_n(0^\circ)$ = diff. cross section at 0° , nt = sample thickness
 d = detector diameter, L_1, L_2 = source-sample, sample-detector distance
 Then, since the sample-out flux is $I_0 = Q$, the transmission due to singly-scattered neutrons is:

$$T_1 = \frac{\pi}{4} \left(\frac{dL}{L_1 L_2} \right)^2 n t \sigma_n(0^\circ) e^{-nt\sigma_T} \quad (3.21)$$

from which the apparent decrease in total cross section becomes

$$\frac{\Delta\sigma_T}{\sigma_T} = \frac{\pi}{4} \left(\frac{dL}{L_1 L_2} \right)^2 \frac{\sigma_n(0^\circ)}{\sigma_T} \quad (3.22)$$

Now the minimum sample diameter to just obscure the detector, under the criterion of small source diameter and large detector diameter is $d = d_o + \frac{L_1}{L} D_2$.

On this basis, it may be shown that the condition for minimum inscattering becomes:

$$\frac{L_1}{L} = \left(\frac{d_o}{D_2}\right)^{1/2} \left(1 + \left(\frac{d_o}{D_2}\right)^{1/2} - 1\right) \quad \begin{array}{l} d_o = \text{source dia.} \\ D_2 = \text{detector dia.} \end{array} \quad (3.23)$$

In the present experiment where $d_o = 2.5$ cm, $D_2 = 12.5$ cm, this results in a ratio $L_1/L = 0.30$, or a sample placement about $1/3$ of the flight path from the first counter.

Dead Time Considerations and Reversal of Start and Stop Signals.

Because of the property of the time-to-amplitude converter that a "start" signal with no "stop" signal within the predetermined time scale results in a paralysis of the convertor for a time of ~ 7 μ sec, serious consideration has been given to the effect of TAC dead time on system counting efficiency.

If there are no correlated stop signals, the live time of the system is just the probability that the system will be unparalysed for a time after the system has been initially paralysed by the arrival of a start signal; in other words, the live time is determined by the probability of an interval greater than 7 μ sec between start signals.

This probability is just $e^{-N_1 \tau_{\text{dead}}}$, which in the present experiment is about 0.001, because of the very high start counter rate. However by delaying the start signal a time just equal to the full scale time of the TAC, and then initializing the TAC with the signals from the second detector, this problem of extremely low live time is circumvented, and the live time becomes, for a stop rate in the present case of $\sim 200/\text{sec}$, greater than 99%. The method of delaying the start signal must, in addition to meeting the obvious requirements of time stability, be in itself non-paralysable. This criterion eliminates the choice of logic elements such as monostable flip flops; however a standard delay line meets these requirements. Rise time and pulse amplitude losses in the delay line are severe, and it is necessary to retard only logic signals of uniform shape and to regenerate the signal at the output of the line.

3.7 Experiment Configuration - Physical Layout

Fig. (5) is a scale drawing of the components of the time of flight facility. A beam of $\sim 10^6$ neutrons/sec emerges from the reactor, and after traversing about a 1 metre flight path, strikes the start counter which is a 2.5 cm diameter by 2 cm long NE111 plastic scintillator directly coupled to an RCA8575 phototube operating at 2300 V. Scattered neutrons emerge through a port in the 40 cm thick water-filled shielding wall, and pass through, or are deflected by, the sample. Solid

samples are mounted directly between two horizontal aluminum bars which extend in such a manner that the beam views the same amount of sample holder with the sample in or out. Powdered samples are encased in thin wall aluminum cans, are are mounted between the sample-holder bars with a dummy can in the sample-out position. The sample holder is coupled to an air piston controlled by a relay-controlled air valve operated indirectly by signals from the analyser.

The stop counter is a 12.5 cm diameter by 2.5 cm thick NE111 scintillator coupled to a Phillips XP1040 phototube operated at 2900 V. The detector is heavily shielded with paraffin and lead, as described in Section 3.4.

The flight path between the scintillators is 3.68 m, and the sample is situated 1.0 m from the start counter, a position reasonably near the optimum position of $0.30 \times \text{total flight path}$.

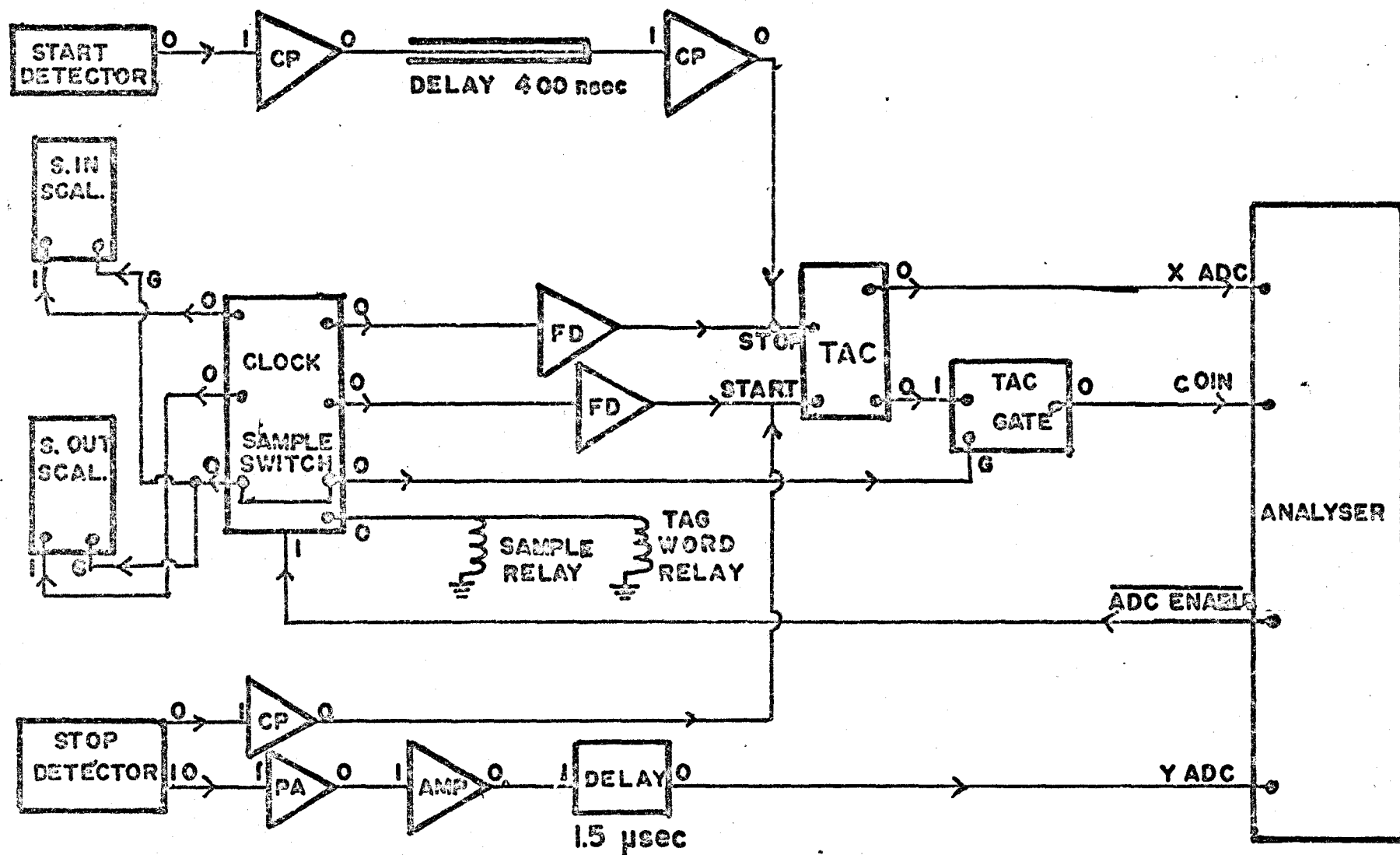
3.8 Experiment Configuration-Instrumentation

Fig. (14) is a block diagram illustrating the main components of the experimental instrumentation. The mode of operation is as follows.

Signals resulting from the detection of an event at the start counter and stop counter are sensed at the photo-multiplier anodes. These fast signals are converted to logic signals by fast comparators built at this laboratory. The

FIG.14 SCHEMATIC-INSTRUMENTATION LAYOUT.

INDIVIDUAL COMPONENTS ARE DESCRIBED IN SECTION
3.8 FF.



ABBREVIATIONS

I	INPUT
O	OUTPUT
G	GATE
CP	COMPARATOR
FD	DISCRIMINATOR
PA	PREAMP
A	AMPLIFIER

FIG 14

signal from the start counter is passed down a delay line, where it is retarded 400 nsec, and regenerated at the output by a second comparator, and enters the stop side of the time to amplitude converter. The signal from the stop counter passes directly to the start side of the time to amplitude converter, an Ortec Model 437. The TAC output is a bipolar signal of height 0-10 V, the pulse height being directly proportional to the time difference between the arrival of logic signals from the start and stop counters. One TAC output is routed directly to the input of one side of a dual analog to digital convertor. The second output is used to generate a +5 V slow logic signal to be used as a gating pulse for the dual ADC.

The second ADC is used to record the pulse height of the second counter in order to apply a walk correction to the time scale, as described previously in the discussion of the detection mechanism. Signals are extracted from the dynode chain at a point several stages up from the anode by a circuit with long time constant. Because the signal is still relatively small at this stage, charge saturation effects are minimal and the charge pulse is proportional to the scintillator light output. These pulses are amplified by a standard preamplifier-amplifier combination as used in scintillation spectroscopy. The bipolar output pulses are delayed 1 μ sec. to establish time coincidence with the TAC events, and are input to the second analog-digital convertor.

The design of the experiment controller module, which was constructed from Digital Equipment Corp. standard logic modules, encompassed four functions:

- (1) Sample-in time, sample-out time, monitor.
- (2) Time scale calibration.
- (3) Dead time monitor.
- (4) Sample switching controller.

The first three functions are realized by manipulations of pulses from an internal clock operating at about 1 cyc/sec. To monitor sample-in and sample-out time these clock pulses are routed to two scalars under control of the switching controller section. Pulses are only generated at each scalar when the sample is in the appropriate position, and a block signal inhibits the scalar during the time of sample switching.

The same clock pulses are used to generate monitor start and stop pulses at the same rate as the scalar pulses. Alternate stop pulses are delayed 50 nsec, and 400 nsec and these are routed to the inputs of the TAC. Thus, since these pulses are asynchronous with real events, and therefore, pulses in the y ADC, the time scale corresponding to zero pulse height contains two peaks, whose positions are a measure of the time scale calibration, and whose areas bear a direct relationship to the counts in the sample-in and sample-out scalars; the ratio of the sum of the peak areas to the scalar reading being simply the system live time.

By observing these monitor peak positions over a one

week time interval, the time stability of the system has been determined to be less than 0.1%.

The fourth function of the experiment controller is initiated by a signal generated in the analyser. The analyser is operated in the so-called "address-recording" mode in which the 12 bit x and y addresses of an event pair are stored in a 24 bit address in a small buffer memory. When the memory is filled, corresponding to 384 events, the contents of the memory are output on magnetic tape. During this time the analog-to-digital convertors are disabled. The disable signal is utilized by the experiment controller module to initiate a sample switching cycle. Thus the mode of switching after a pre-determined number of events, yields sample-in, sample-out times fairly close to the optimum times as discussed in Section 3.6.

The experiment controller module performs three functions, when the ADC disable signal is detected.

The first is to change the state of a flip-flop whose output is used to set or reset a relay controlling the air supply to the sample-switching air piston.

The second function of the experiment controller is to generate a 5 V blocking signal applied to the time monitor scalars, and the TAC gate module. This signal is of 0.5 sec duration to encompass the time necessary for the magnetic tape transport and the sample holder to complete their operations, and serves to disable the entire data acquisition system during the transition time.

The third function of the module is necessary to permit recognition of buffer dumps on the tape corresponding to sample-in and sample-out dumps. Each dump of 384 address pairs is preceded by a 36 bit label or "tag word". The experiment controller, by switching a DPDT relay, changes the state of the lowest order bit of the label. Thus a 1 state of this bit corresponds to sample in, and a 0 bit to sample out record.

The last element in Fig. (14) is the analyser, which, as has been indicated, functions to convert the pulse heights of the TAC and stop counter to binary integers, to accumulate these digitized pulse heights in a buffer memory, and to output the contents of the memory onto magnetic tape. These functions of the analyser describe only the particular mode of operation of the analyser system which is applicable to this experimental application.

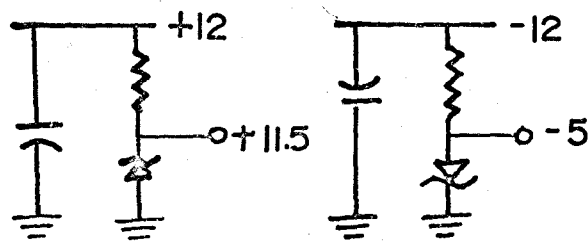
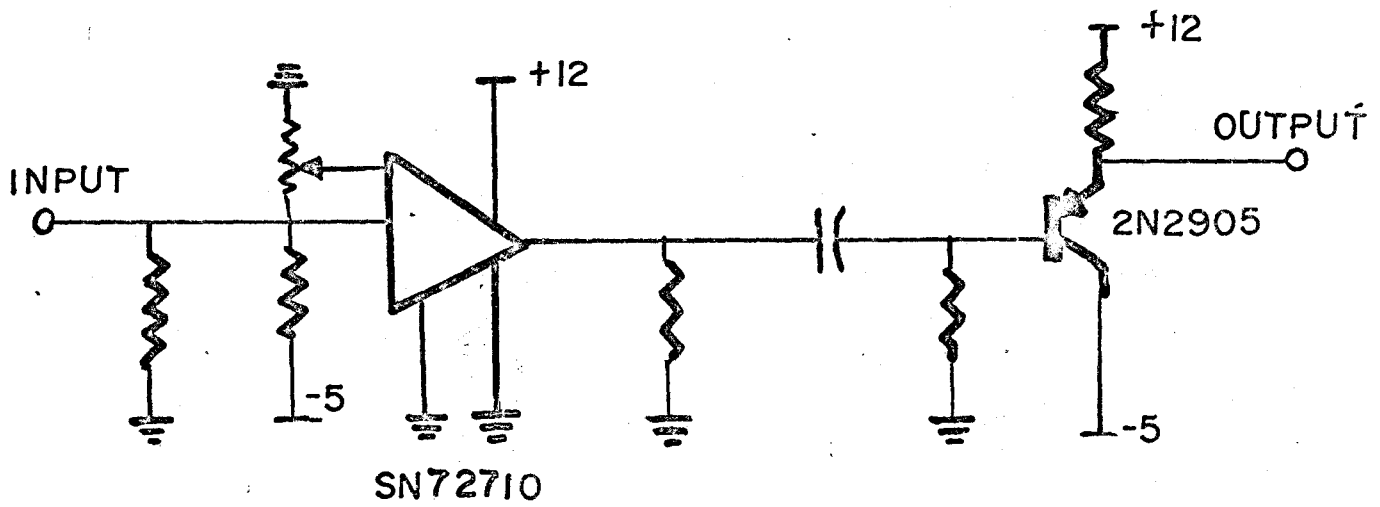
3.9 The Fast Comparator Circuit

Fig. (15) is a circuit diagram of the fast comparator circuit. The circuit was based on a Motorola SN72710 integrated circuit comparator, followed by an emitter follower stage. The input signal was terminated in $50\ \Omega$, and compared at the input of the comparator to a voltage level determined by the $2K\Omega$ potentiometer and the $25K\ \Omega$ fixed resistor. When the difference voltage changed sign, the comparator switched states,

FIG.15

SCHEMATIC - FAST COMPARATOR CIRCUIT

FAST COMPARATOR



LEVEL VOLTAGE SUPPLY

in this configuration dropping from +1.5 V steady state to 0.3 V. The comparator remained in the opposite state for the duration of the polarity reversal of the input difference signal, or for a time determined by internal components of the IC, whichever was longer. In the present experiment, the pulse width was determined by internal parameters, and the output pulse was approximately rectangular in form. The rise time of the output pulse was ~ 20 nsec, but because of the uniformity of the output, this time was not the limiting factor in system resolution. The output signal was applied to a series capacitor with resistor to ground, to shift the output level to negative polarity.

To increase the driving capability of the comparator, this output signal was fed to the base of a 2N2905 transistor in an emitter-follower configuration. The output of the emitter follower was used directly as the input to other modules.

3.10 Time-to-Amplitude Convertor

The time-to-amplitude convertor was a commercial unit, the Ortec 437. The principle of operation was similar to an analog to digital convertor, that of linear charging of a capacitor initiated by an input pulse; however in the TAC operation, the limit of the charging duration was determined by the arrival of a second pulse, rather than by comparison of the voltage level with the height of the input peaks.

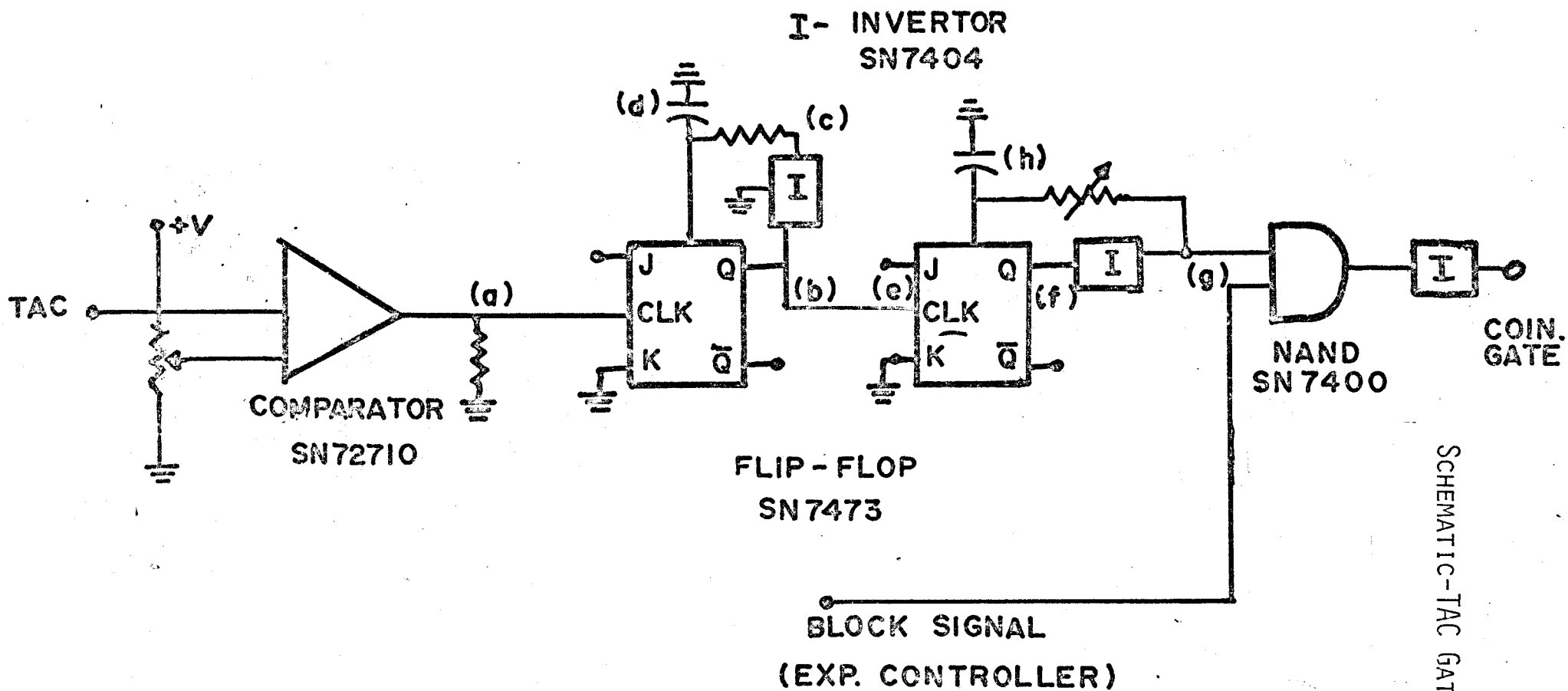
Following the arrival of the second pulse, the charging circuit was switched off, and the charge on the capacitor, and hence, the potential difference across the capacitor plates was proportional to the time interval between the arrival of the two pulses. Additional circuitry then shaped this level to a standard bipolar signal of height 0-10V, and 2 μ sec width.

3.11 The TAC Gate Module

In operating the analyser in the coincidence configuration, whereby address pairs were analysed simultaneously, the analyser was supplied with a +5 V logic signal, enabling the ADC inputs. Since events in the second counter due to background radiation could occur in the absence of a TAC event, but since every TAC event, which originated in an event in the start and stop detectors, was accompanied by a pulse height event, this coincidence signal was generated from the TAC output in the TAC gate module. A second function of the TAC gate module was the disabling of the analysis system, by inhibiting the generation of the coincidence signal, during sample switching.

The circuit diagram of the TAC gate module is shown in Fig. (16). The bipolar TAC output signals were applied to one input of the comparator. The operation of the comparator has been described in Section 3.9.

Fig. (17) illustrates the signals at various points



SCHEMATIC-TAC GATE MODULE

Fig. 16

FIG.17.

SIGNALS IN TAC GATE MODULE.

SIGNALS ARE CODED TO LOCATIONS
IN FIG.16.

(a)



(b)



(c)



(d)



(e)



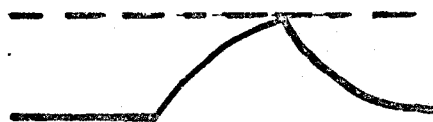
(f)



(g)



(h)



TIME →

in the circuit.

The positive-going trailing edge of the comparator output was used as a strobe for the J-K flip flop. This strobe resulted in a ground level appearing at the Q output, (b). This signal was inverted, (c) and passed through an R-C network with variable time constant to the "clear" input (d). When the signal height exceeded the logical "1" threshold, the flip-flop was cleared, returning the Q output to a 1-state.


The trailing edge of the Q output then strobed a second J-K flip flop, which operating in a similar manner, resulted in a final output, at (g) consisting of a 5.0 V signal delayed a time determined by the time constant of the first feedback network, with width determined by the time constant of the second feedback network.

This output, which was utilized as the analyser gate signal, was used to paralyse the analyser during sample-switching by performing an AND condition between the gate signal and the system BLOCK signal originating at the experiment controller module.

3.12 The Experiment Controller Module

The function of the experiment controller has been described. This module was constructed of Digital Equipment Corporation Flip Chips, which are self-contained logic modules mounted on standard sized phenolic boards. These boards are

retained by strip connectors connected in racks to a power supply. Hardware programming was performed by patch wires to pins leading from these connectors.

A basic element common to all of these logic modules is the gated input symbolized by . This input is enabled by a logical 1 (gnd) level, and disabled by a logical 0 level (-3 V). When enabled, the input is sensitive only to positive-going pulses, thus the standard logic pulse is a pulse quiescent at -3 V, rising to ground with a rise time of ~ 30 nsec. and remaining at ground potential for about ~ 100 nsec. In many applications, one particular module, the pulse amplifier, acts primarily in this function of sensing a positive going level change and converting this to the standard pulse. Thus the pulse amplifier acts as a sort of logical differentiator, generating standard pulses in response to level changes.

The experiment controller module in the present experiment consisted of the two discrete functions, that of generating a monitor signal for time monitoring, live time monitoring, and system gain monitoring, and that of sample switching and system paralysis in response to a block signal from the analyser.

The controller logic diagram is drawn in Fig. (18). The upper half of the diagram represents the time monitor circuitry, and the lower half, the sample switching circuitry.

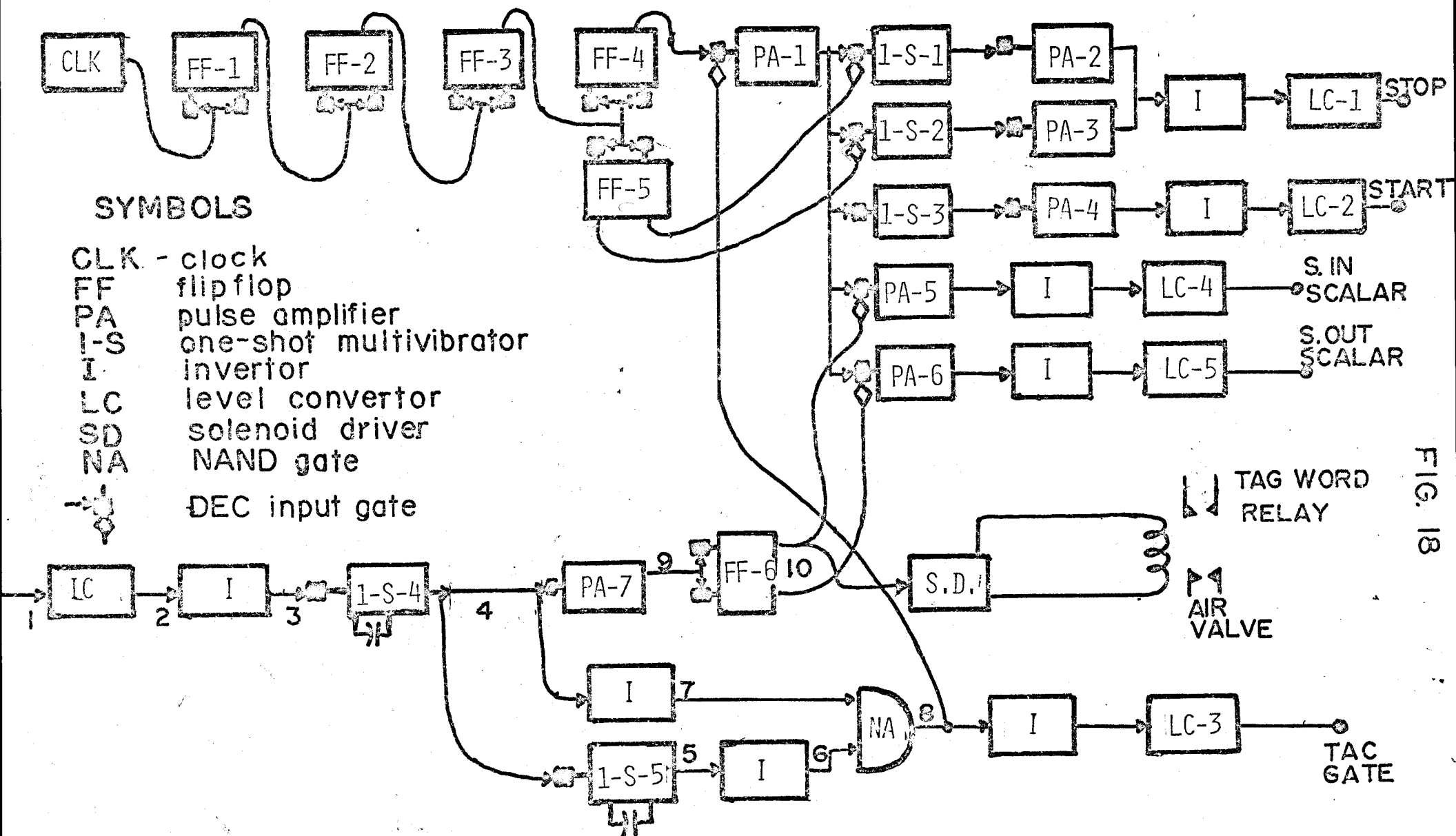


FIG. 18

FIG.18.SCHEMATIC-EXPERIMENT CONTROLLER MODULE.

LOGIC ELEMENTS ARE CONSTRUCTED OF DEC "FLIP CHIP" ELEMENTS

The time monitor circuit was initiated by a variable frequency clock (R401). The lowest repetition rate of this clock was about 15 Hz, therefore it was necessary to scale down this rate by using four flip-flops in series acting as a four-bit shift register. Clock output pulses were applied simultaneously to the pulse inputs of the first flip flop, causing it to change state. One output of the first flip flop was connected to the inputs of the second flip-flop in turn. Although this level was changing state at the clock rate, because the pulse inputs of the second flip-flop fired only on positive-going pulses, the resulting frequency of the state change of this flip flop was one-half the clock frequency. Similarly by routing the clock through four such flip flops, the clock frequency was reduced by 2^4 at the output of the fourth flip flop.

This signal was routed to the pulse input of a pulse amplifier (PA-1) whose level input was coupled to the sample switching circuitry in such a manner that it was disabled during the time of sample switching. The output of the pulse amplifier, then, was a standard signal with frequency 1/16th of the clock frequency, present only when the sample was in position, in or out of the beam. This signal was routed to five circuits which ultimately provided start and stop monitor signals for the time to amplitude convertor, and monitor pulses for the sample in and sample out scalars.

The module labelled (1-S-3) was a one shot multi-vibrator whose output changed from a logical one state to logical zero at the time of arrival of the standard pulse, and returned to a logical one state after a time determined by a variable potentiometer in an RC network. The delayed state change was sensed by a pulse amplifier whose output was inverted to facilitate conversion to conventional fast logic levels in the W998 module, which was a standard comparator circuit previously described. Thus, these components resulted in a standard fast logic signal, generated at 1/16th the clock frequency, and delayed a fixed time of 50 nsec.

Similar networks, those containing the one-shots 1-S-1 , and 1-S-2 , were used to generate fast logic signals delayed 100 nsec and 450 nsec with respect to the pulse amplifier output. These networks differed in one respect, however, in that the inputs to the one-shots were enabled by the outputs of the flip-flop FF-5 , which was changing state at the scaled clock frequency. Thus the OR output of these two networks was fast logic signals at the scaled clock frequency, with alternate signals delayed 100 nsec and 450 nsec with respect to the pulse amplifier (1-2) signal.

Using these signals as input to the "stop" side of the TAC, and the first fast logic signal as input to the "start" side, resulted in two peaks appearing on the time axis of the time of flight spectrum at times of 50 nsec and 400 nsec respectively.

The output of the pulse amplifier PA-1 was also fed into two circuits to generate signals used as scalar inputs. The first logic element in these networks was a pulse amplifier which was enabled by a level generated in the sample-switching side of the controller, such that one pulse amplifier was enabled during the time the sample was in the beam, and the other pulse amplifier, while the sample was out of the beam. These pulse amplifier outputs were inverted and input to W601 convertors which resulted in +5 V signals, suitable as scalar inputs.

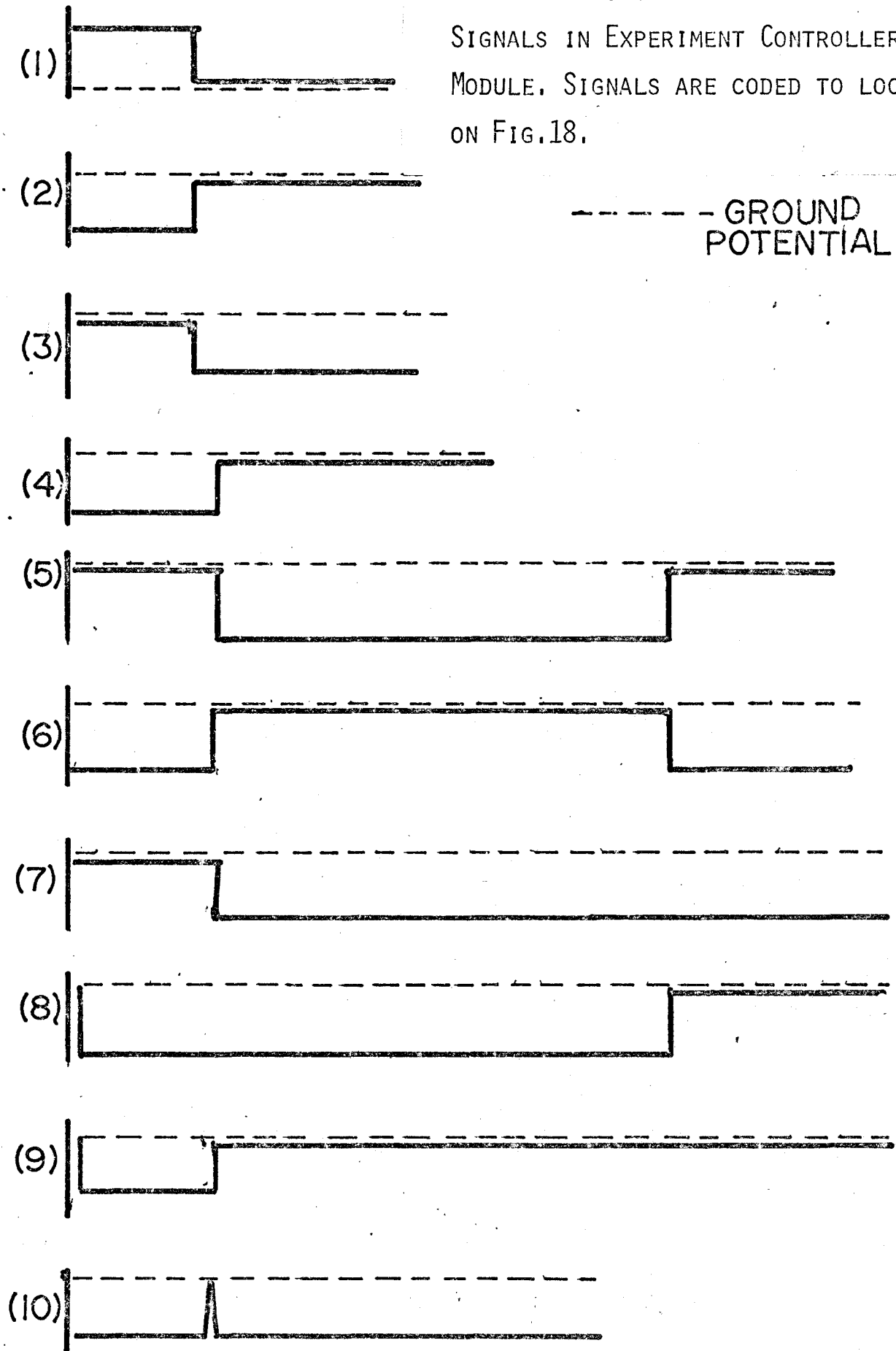
The counts accumulated in the sample-in and sample-out scalars served as a monitor of the relative sample-in and sample-out times.

Furthermore since a start-stop signal pair was produced simultaneously with the scalar signal, by summing the amplitudes of the two monitor peaks appearing in the time spectrum (sample-in or sample-out), and comparing this sum to the appropriate scalar reading, the system live time was obtained directly for the sample-in and sample-out spectrum.

The operation of the sample-switching side of the controller is best understood with reference to Fig. (19). A sample switch cycle was initiated by the ADC disable signal from the analyser. This signal was converted to a negative-logic signal in the W510 input convertor (2), and inverted in the R107 module (3). This signal fired a one-shot multi-

FIG.19

SIGNALS IN EXPERIMENT CONTROLLER
MODULE. SIGNALS ARE CODED TO LOCATIONS
ON FIG.18.



vibrator, which resulted in a negative signal of 100 msec duration (4). The trailing edge of this pulse was input to a pulse amplifier, resulting in a narrow ground signal delayed 100 msec from the start of the cycle. This signal was used to change the state of a flip-flop, whose output levels controlled the scalar monitor pulse generators. In turn, one output, driving a W040 solenoid driver connected to a relay, controlled the air supply to the sample-switching piston, and changed the state of the tag word identifier bit through a second relay with DPDT contacts. Thus, 100 msec from the start of the cycle, the tag word switch and air piston were actuated. This delay was necessary to ensure tag word switching in the middle of a tape dump cycle, as ambiguities developed when the tag word was switched simultaneously with the beginning or end of a tape dump cycle.

The remaining components were utilized in generating the block signal applied to the TAC gate module. The one shot (1-S-5) generated a 400 msec negative signal (6) on the trailing edge of the input pulse. This signal was OR'ed with the signal (5) by inversion and input to a NAND gate. Thus the output of the NAND gate (9) was a 500 msec duration signal, initiated by detection of the analyser block signal. This output was inverted, and converted to a positive signal in the LC-3 module, and was, in addition, used as the level input to the PA-1 carrying the monitor pulse. The positive

signal was utilized as a block signal on the TAC gate module and the scalars, thereby immobilizing the data acquisition system for the duration of the sample-switching cycle.

3.13 The Multichannel Pulse Height Analyser

The pulse height analyser is comprised of the main logical elements shown in Fig. (20). Inputs to the two analog-to-digital convertors, labelled ADC1 and ADC2 were bipolar pulses of 2 μ sec duration with continuous pulse heights, varying over the range 0-10 V. The ADC's were enabled by a linear gate at the input, which was closed during the analysis time for an event pair, and was in turn enabled by a 5 V logical signal generated by the TAC gate molecule.

The ADC functioned to convert the continuous pulse height signal to a quantized time signal, by triggering a ramp circuit when the signal was sensed, and comparing the height of the linear ramp to the initial pulse height. Thus the pulse was converted to a time interval, whose duration was proportional to the initial pulse height. During this time interval, a precise high frequency clock was enabled, and the number of clock pulses generated was a quantized measure of the initial pulse height. These clock pulses were accumulated in a 12 bit register, labelled the "address scalar", thus the pulse height was recorded as a binary number in the range 0-4095. This process is known as analog-to-digital conversion.

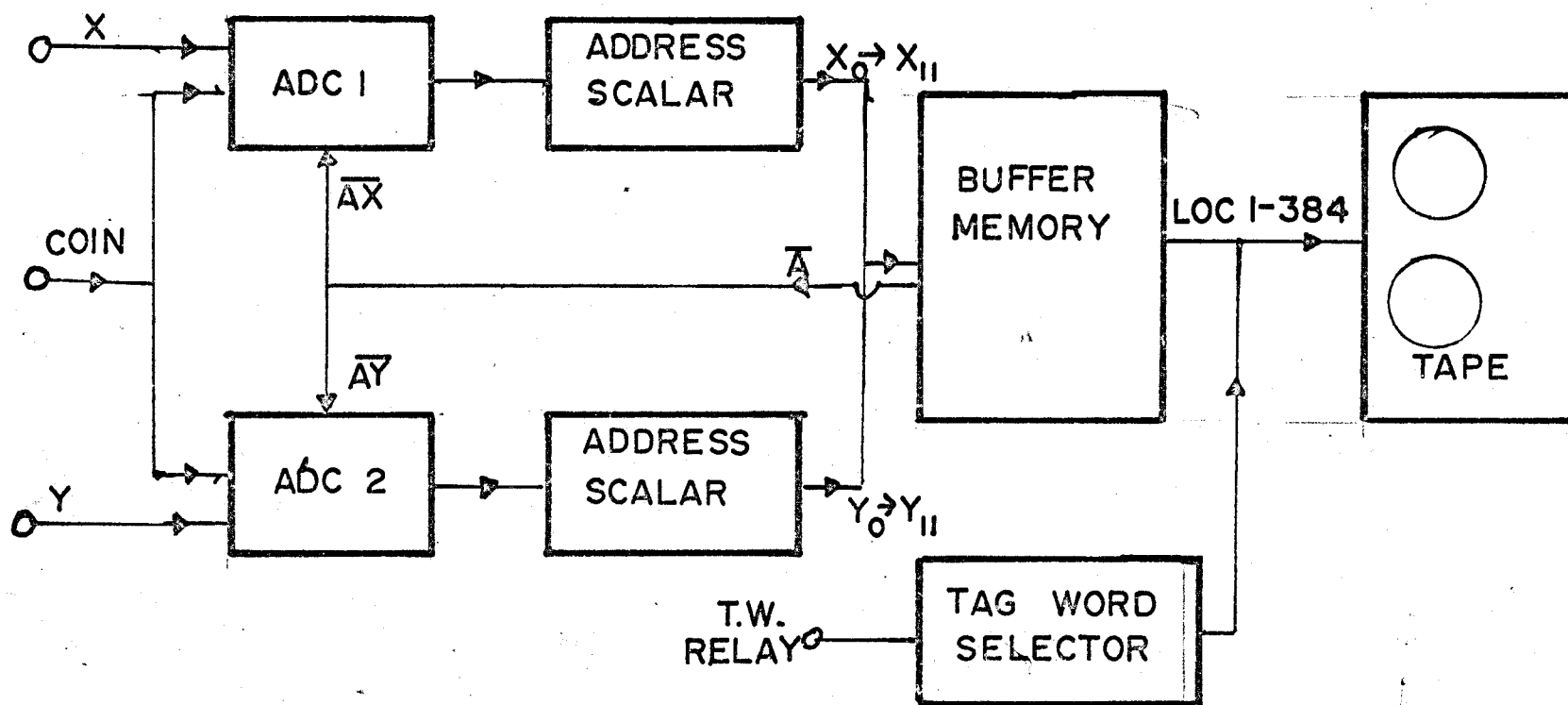


FIG. 20

FIG. 20. SCHEMATIC - PULSE HEIGHT ANALYSER.

ANALYSER IS OPERATED IN THE "ADDRESS-RECORDING" MODE.

In the present experiment, these address pairs were stored in sequential 6 bit "bytes" of a 1536 ^{byte} bit core memory. Thus, an event resulted in two twelve bit addresses stored in four bytes of the buffer memory. When this memory was full, corresponding to 384 event pairs, a signal was sent to the ADC's, disabling their operation and the contents of the memory were output on magnetic tape.

In order to facilitate recognition of this record at a later time, the record was preceded by an identifier consisting of two identical 36 bit words. The uppermost 12 bits of the identifier were set by the analyser and indicated the machine function and the ADC pair resulting in this record. The lower 24 bits were available to the experimenter as an experiment label, and as indicated in the discussion of the experiment controller module. In the present experiment, the lowest order bit was used to identify sample-in and sample-out dumps.

Tape Totalize Mode

During the course of a single experiment, approximately eight 2400' tapes were filled with address-recorded data. This physical volume of data is unmanageable as computer input requiring excessive I/O time with consequent cost excesses. As a first step in data reduction, the analyser was used in the tape totalize mode, in which the address pairs stored on tape were utilized as input to the central memory of the analyser instead of the usual on-line analysis using address pairs

generated by the ADC's.

Since the address pair would require a memory size of $2^{12} \times 2^{12}$ words, the x and y addresses were truncated to 9 bits and 5 bits respectively, resulting in a 512 channel time scale and a 32 channel pulse-height scale. The uppermost bits of the address pair were selected by appropriate wire patching of a configuration plug.

In the present experiment the tape was scanned twice, selecting, in the first pass, sample-out dumps with even tag word, and in the second pass, alternate dumps with sample-in, which had odd parity tag words.

On each pass, the accumulated data, which had been stored in the 18 bit words of the central memory, were dumped onto magnetic tape. Thus the totalized record consisted of 2^{14} (= 16384) 18 bit addresses corresponding to the accumulated counts in each address of the 512×32 array, preceded by the repeated 36 bit label. These data were utilized as input to a series of computer programs, and were readily handled by available I/O subroutines in the existing program library.

CHAPTER IV

DATA ANALYSIS

4.1 Cross Section Calculation

The nomenclature "cross-section" finds its origin in an elementary interpretation of macroscopic interaction properties based on physical cross-sectional area presented by a nucleus to a beam of incident particles. From this elementary consideration the cross section has evolved into a fundamental property of nuclear systems, but the basic interpretation is adequate in deriving the relation between the transmission through a thick sample and the nuclear cross-section.

In an element of thickness dx of sample medium, the number of beam particles interacting with sample nuclei, and thus removed from the incident beam is proportional to the product of the number of nuclei in the elemental segment and the cross-section area of each nucleus.

$$\text{Thus} \quad dI = I(x) \frac{N}{W} \rho \sigma dx \quad (4.1)$$

N = Avogadro's no.

W = atomic weight

ρ = density

σ = cross section

I = beam intensity at x .

and integrating from $x = 0$ to the sample thickness t

$$I = I_0 e^{-\frac{N}{W} \rho \sigma t} \quad (4.2)$$

Thus, the cross section is related to the transmission of the sample by:

$$\sigma = -\frac{W}{N \rho t} \ln T \quad (4.3)$$

This simple relationship is the basis for the cross-section calculation in the present neutron transmission experiment.

Time-Energy Relationship

Since neutrons with energies of 800 keV \rightarrow 3 MeV have velocities approaching 0.1 C, it is necessary to use relativistic mechanics in calculating the time-energy relationship. Thus, the kinetic energy of the neutron, in relativistic form, is

$$T = mc^2 - m_0 c^2 \quad (4.4)$$

$$= m_0 c^2 \left(\frac{1}{\sqrt{1 - \frac{v^2}{c^2}}} - 1 \right) \quad (4.5)$$

$$= 939 \left(\frac{1}{\sqrt{1 - \frac{v^2}{c^2}}} - 1 \right) \quad (4.6)$$

This relationship was calculated for each point in the time spectrum.

4.2 Data Reduction - General Considerations

Although in essence, the transformation from neutron time of flight spectra of an incident and transmitted beam to a time spectrum of neutron transmission and thence to a cross section involves elementary calculations, in practise, several additional manipulations are necessary in the calculation of the cross section from the experimental data.

The measured spectra are in the form of a two parameter array. $S(x,y)$, the first subscript relating to the time axis and the second to the second counter pulse height.

The transformations, analytically, are the following.

- (1) A correction for walk in the second counter, which is evidenced in the initial spectra as an apparent shift to longer times with decreasing pulse height. Thus, if $\Delta(y)$ is the walk function in channels T_1 : $S(x,y) \rightarrow S(x+\Delta,y)$. (4.7)
- (2) Removal of background from the raw spectra. The background contribution to $S(x,y)$ is of the order of 15 → 30%, and is a component resulting from random coincidence between background events in the second counter and events in the first counter. Because of the random nature of these events, the time distribution is exponential, and an exponential function is fitted to the time channels beyond the range of the neutron spectra, using the methods of regression analysis.

Thus if $B(x,y)$ is the fitted function.

$$T_2: S(x+\Delta, y) \rightarrow S(x+\Delta, y) - B(x, y) \quad (4.8)$$

- (3) Pulse height dependence of the time spectra has now been removed, and the summation over y is performed

$$T_3: S'(x) = \sum_y S(x+\Delta, y) - B(x, y) \quad (4.9)$$

- (4) The individual spectra are corrected for dead time, which is calculated by the relative amplitudes of the monitor peaks to the scalar counts in each mode

$$T_4: S'(x) \rightarrow S'(x)/L \quad L = \text{live time fraction} \quad (4.10)$$

- (5) Accumulated counts in the transmitted beam and incident beam have been obtained for different total running times. The run time is proportional to the accumulated accounts in the related monitor scalar. Thus, before the transmission can be calculated, the transmitted spectrum is multiplied by the inverse ratio of run times

$$T_5: S_o'(x) \rightarrow RS_o'(x) \quad R = \frac{\text{scalar cts. sample in}}{\text{scalar cts sample out}} \quad (4.11)$$

- (6) The raw spectra have now been reduced to the point where a transmission and cross-section calculation is straightforward. Therefore the remaining calculations are:

$$T_6: T(x) = \frac{S_o'(x)}{S_I'(x)} \quad (4.12)$$

$$T_7: \sigma(x) = -\frac{1}{nt} \ln T(x) \quad (4.13)$$

$$T_8: \sigma(E) = \sigma(x) \quad \text{where } E \text{ and } x \text{ are related by the relativistic energy equation.} \quad (4.14)$$

4.3 Computer Calculations

Experimental measurements conducted to determine neutron total cross sections were characterized by two 512×32 arrays, one corresponding to events with the sample in the beam and the other with the sample out of the beam. Each element in each array consisted of an 18 bit word containing the accumulated events in the matrix element (x,y) where x corresponds to the neutron flight time and y, the pulse height in the second counter. The data was recorded on seven track magnetic tape in a format compatible with computer records.

Cross section calculations were performed on a scientific computer, the CDC 6400, from these data, using additional parameters provided by the experimenter on punched cards.

The data analysis was performed using two computer programs. The first program performed manipulations on the individual dumps to reduce the array to a pure time-of-flight spectrum with background subtracted and walk correction applied. The second program used these spectra as input data and calculated the transmission, cross section, and energy of calibration.

The data manipulations will be described in more detail in the following sections.

4.3.1 Calculations with individual spectra

The calculations performed by the first program are flow charted in Fig. (21). Since, on the average, each cross-

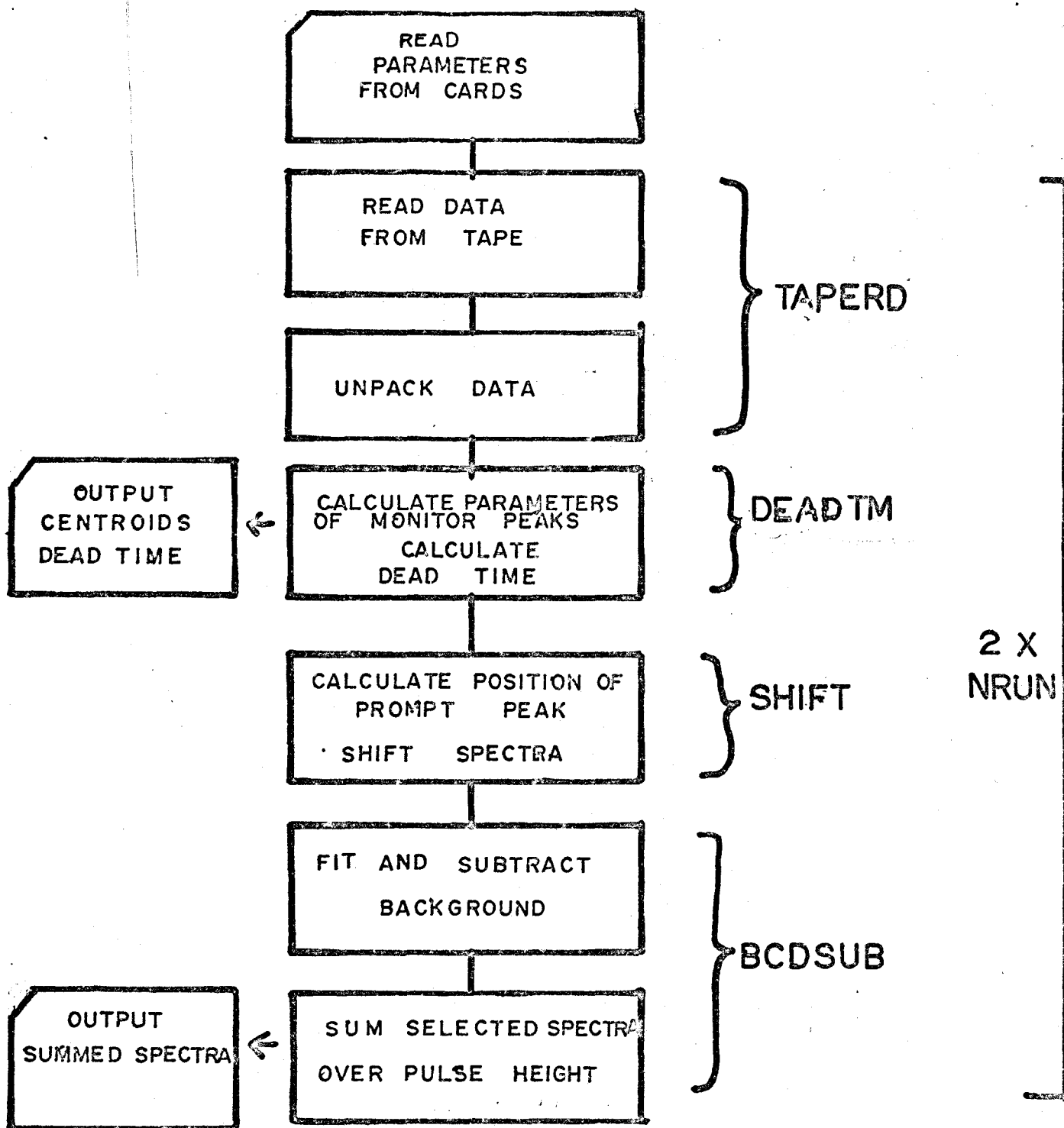


FIG.21.

FLOW CHART OF FIRST PROGRAM

PROGRAM REDUCES DATA OF INDIVIDUAL SPECTRA BY REMOVAL OF BACKGROUND, CORRECTION FOR WALK, ETC.

section measurement resulted in from six to eight tapes of address-recorded data each containing $\sim 3 \times 10^6$ events, the computer input data from an experiment, therefore, consisted of the same number of arrays of sample-in and sample-out data. Thus, the calculations were performed 12 to 16 times.

By convention, we will refer to the address locations of the time-of-flight spectra as "channels" and those of the pulse height spectrum as "groups".

The input parameters were the following:

- (1) Tag words of each Record
- (2) Monitor scaler readings for each record
- (3) Low group, high group of time-of-flight spectra
- (4) Channel numbers of background regions, and neutron spectra
- (5) Estimate of centroid of prompt peak, low monitor peak, high monitor peak.

The subroutine performed the following functions.

TAPERD. Data from the magnetic tape was read into 4917 successive 60-bit words of central memory. Each record was checked for consistency of tag word with the specified tag word, and presence of file marks or parity errors. If the data were accepted, they were then unpacked into 16384 words of central memory by successive shifts so that each computer word was equivalent to the corresponding 18 bit analyser word.

DEADTM . The O group contained two peaks generated by the experiment controller module. Because events in these peaks were produced by the same clock which produced the scalar pulses for the time monitor scalars, the ratio of the integrated amplitude of these peaks to the scalar value was a measure of the system live time.

Furthermore, the separation of these peaks was used for time scale calibration.

Subroutine DEADTM calculated the area of these peaks by subtracting a background determined by the accumulated events on either side of the peaks and calculated the centroid by a numerical summation of the first moment of the distribution. The centroids and system live times were output on punch cards as input data to the second program.

SHIFT. This subroutine shifted the time-of-flight spectra in each group an amount determined by the fitted "walk" function detailed in section 3.5. After shifting was completed, the region of channels containing the prompt peak was summed over all groups and the summation printed as a check on system resolution and walk correction.

BCDSUB. In a point-by-point determination of cross-section, the backgrounds present in this experiment would be intolerable. However, because of the continuous nature of the primary neutron beam, the backgrounds, although high, arose chiefly from random "coincidences" between events in the start counter and background or uncorrelated events in the stop counter."

Since these background events arose from random time coincidences, it is expected that the background function would resemble an exponential with time constant equal to the mean time between events in the start counter. However, a knowledge of the form of the background function is of little value unless the method is present to evaluate the parameters of the function.

In the present experiment, the time scale corresponded to flight times between 0 and 400 nsec. The flight times represented by the extremes of the neutron energy spectrum, 700 keV and 3 MeV were 320 nsec and 1.35 nsec respectively. Thus the time channels located outside this time range, comprising approximately half the channels in the time spectrum, contained a pure background contribution.

Subroutine BCDSUB fitted an exponential background to these channels using a linear regression analysis applied to logarithms of the channel contents. Individual groups are fitted separately, as the low energy extremum of the neutron spectrum increased with increasing pulse height. Thus, the range of channels used in the regression analysis was varied with pulse height using the analytical expression for the low-energy limit described in section 3.5. Once a fitted function was obtained, it was subtracted from the channel contents of the appropriate group, and at the completion of

the background subtraction, the groups were summed to obtain the final time-of-flight spectrum. The groups contributing to the final spectrum were selected by input parameters, so that only those groups containing a significant neutron contribution were utilized. As this selection was made consistently for sample-in and sample-out spectra, no distortion of the cross-section resulted.

Finally these summed spectra were printed and output on punch cards to be used as input data to the second program.

4.3.2 Cross section calculation

The second program calculated the transmission point by point, the cross-section with associated error, and the energy calibration, and produced tabular and plotted output.

The flow chart for this program appears in Fig. (22).

Input data consisted of:

- (1) Physical parameters
 - (a) Sample thickness, density, atomic weight
 - (b) Flight path and time separation of monitor peaks
 - (c) No. of runs
 - (d) Scalar readings
- (2) Calculated parameters*
 - (a) Centroid of prompt peaks and monitor peaks
 - (b) Low and high channel of neutron spectrum
 - (c) Accumulated background counts at low and high channel.

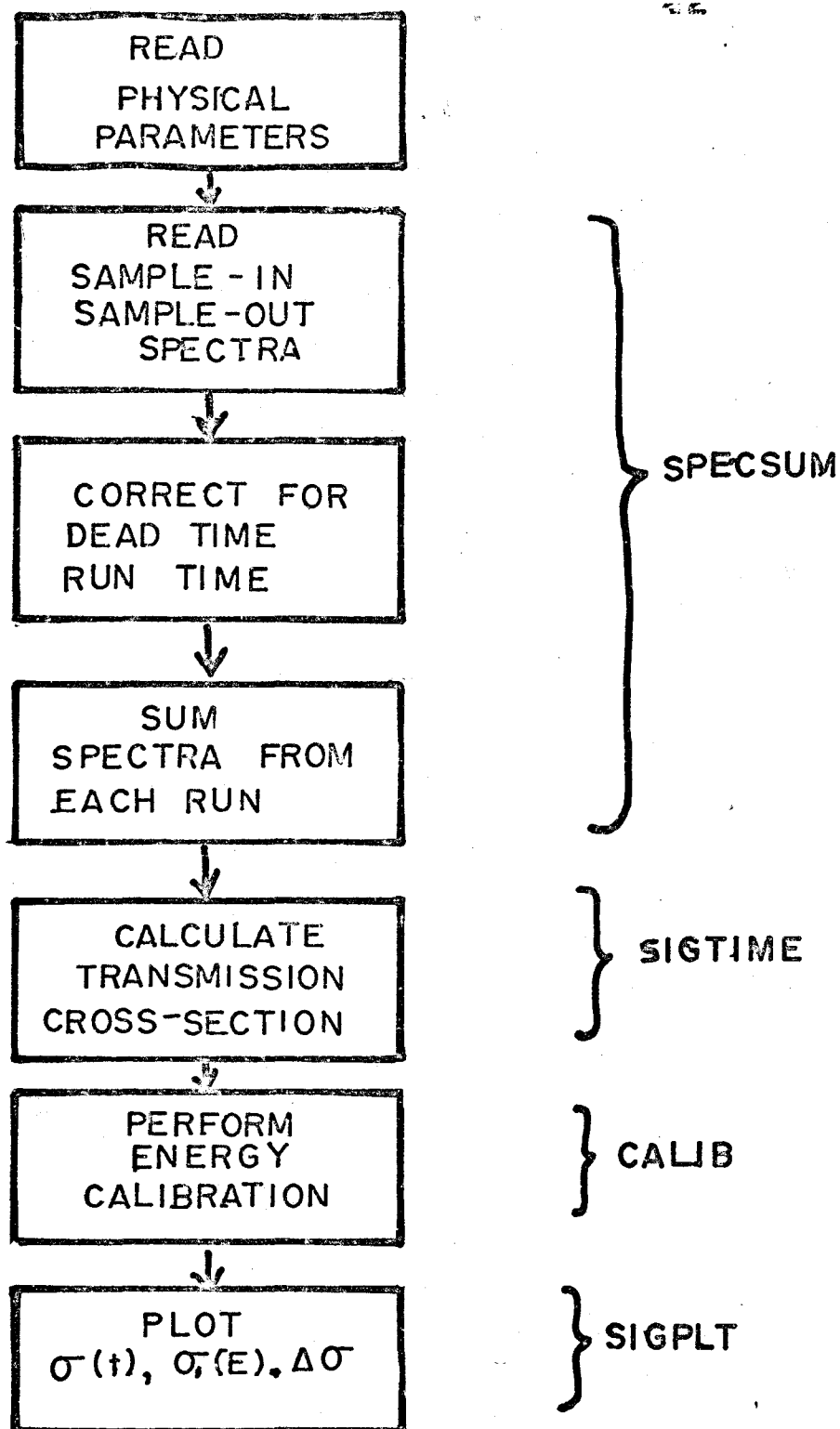


FIG.22

FLOW CHART OF SECOND PROGRAM

PROGRAM CALCULATES CROSS-SECTION FROM SUMMED SAMPLE-IN AND SAMPLE-OUT SPECTRA CALCULATED IN FIRST PROGRAM.

(d) System live time

(3) Reduced neutron spectrum data*

*generated as output from first program.

The calculations performed by each subroutine are described below.

(1) SPECSUM

Individual runs of time spectra were corrected for dead time, and sample-out data were multiplied by the ratio of run times sample-in to sample-out.

The resulting time spectra for each run were accumulated, and the total spectrum printed. Because of stability of the system it was not found necessary to correct for gain shifts between runs, as would be detected by a shift in the positions of the monitor peaks, but if such shifts occurred, a correction could be applied in the subroutine.

SIGTIME

Using the accumulated neutron spectra from SPECSUM, the sample transmission, simply the ratio of sample-in to sample-out accumulated events, with background removed, was calculated at each time channel. From this transmission, and the physical parameters, the cross-section was calculated at each channel position. The statistical error in each experimental cross-section was calculated using a formula derived in section 4.4.

CALIB

This subroutine performed the time scale calibration using the location of the monitor peaks to determine the time conversion gain and the location of the prompt peak for location of the zero time position. The latter is simply:

$$PC = \frac{D}{C} \cdot g^{-1} \quad (4.15)$$

PC = centroid of prompt

D = flight path

c = speed of light = 0.3 m/nsec

g = system gain (nsec/ch)

A calibration of the overall time scale was performed using a TAC calibrator module developed at this lab. The outputs of this module, used as input to the TAC, resulted in a series of narrow peaks separated by a pre-selected, and accurately determined, time interval. The peaks appeared over the entire range of the time spectrum. Thus the channel separations between peaks provided an estimate of the time calibration present at each interval. Higher order coefficients in the calibration curves were evidenced as differences between channel separations.

Fig. (23) is a display of the non-linearity determined by this method. As this non-linearity is small by comparison with the time resolution, it was decided to fit the time scale by a linear function whose slope and intercept were derived from the calibrated curve.

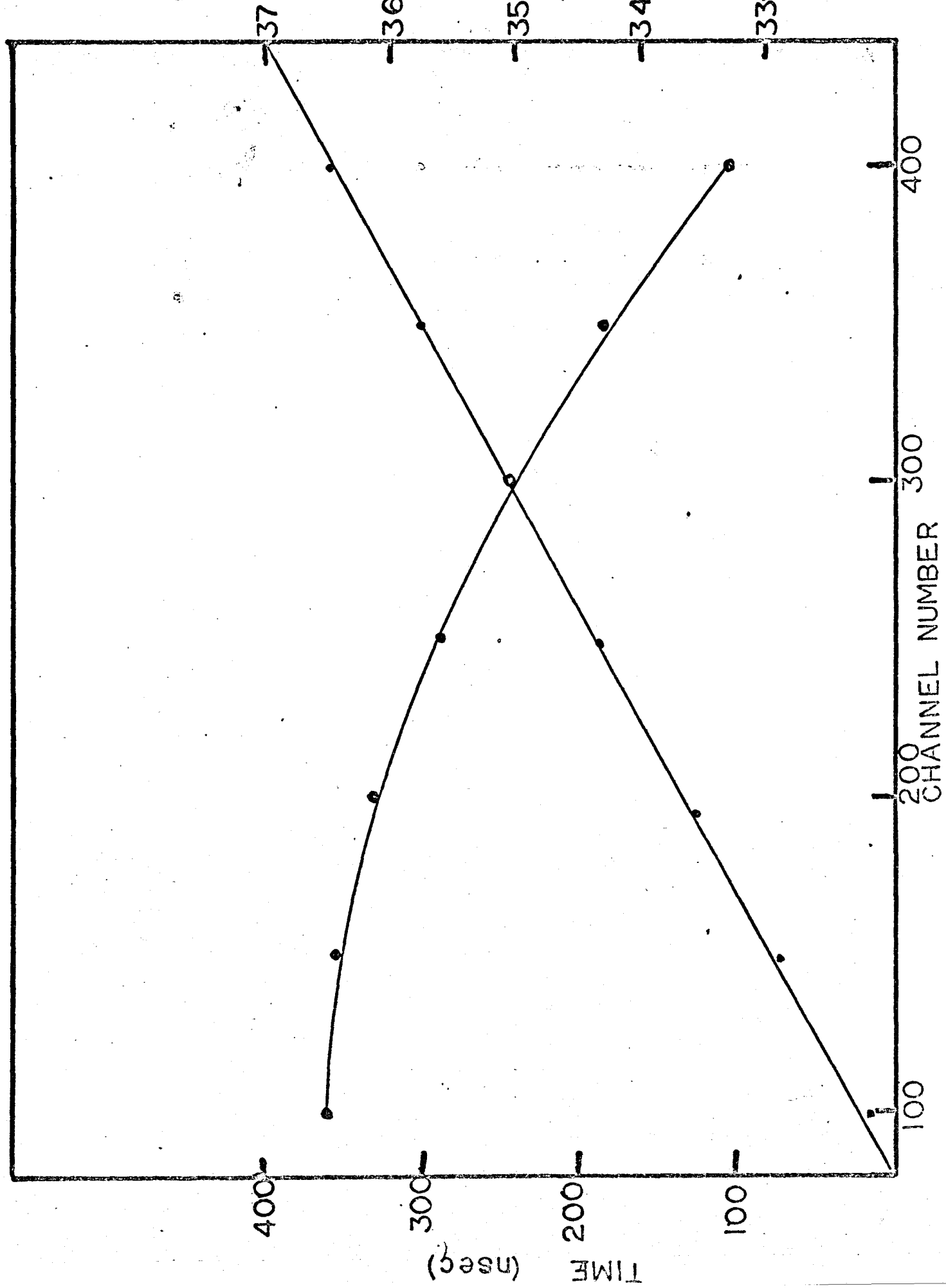
Using the flight times at each channel, the equivalent energy of each channel was calculated from the relativistic time-energy relationship derived in Section I.

FIG.23 NON LINEARITY OF TIME SCALE

INTEGRAL LINEARITY IS SHOWN AS A STRAIGHT LINE FROM THE ORIGIN,AND THE DIFFERENTIAL LINEARITY IS THE CURVED LINE.

FIG. 23

DIFFERENTIAL LINEARITY (chan/40nsec)



SIGPLT

An off-line plotting facility was utilized to generate plots of cross-section as a function of time and energy with associated errors, from the calculated cross-sections, with statistical errors, and the time and energy data .

The input to the plotter was a magnetic tape containing coding generated by the library subroutines called from subroutine SIGPLT.

4.4 Discussion of Errors

Uncertainties in the determination of the cross-section as a function of energy are introduced in three broad areas: errors in the magnitude of the cross-section of a statistical or systematic nature; errors in the energy calibration, resulting in a displacement of the cross section as a function of energy; and errors in measurement of cross-section fluctuations resulting from the finite time resolution of the experiment. These may be viewed consistently as an uncertainty in $\sigma(E)$, E , and $\frac{d\sigma}{dE}$. The quantities are not completely separable, as, for example, an incorrect determination of $\frac{d\sigma}{dE}$ will result in an error in the magnitude of the cross section in a region where the period of fluctuations is comparable with the energy resolution. Similarly, a displacement in the energy calibration will result in an obvious systematic deviation of the experimentally determined $\sigma(E)$.

In the discussion of these uncertainties, the three areas will be treated separately, as the sources of error in each category are distinct.

4.4.1 Errors in magnitude of cross-section

Errors in the magnitude of the cross-section, in regions where the cross-section is not fluctuating significantly with energy, are of two types, the statistical error associated with the counting process, and systematic errors arising from uncertainties in the subtraction of the fitted background function and measurement error in the determination of sample thickness. An additional systematic displacement of the observed cross-section from the true cross-section results from the scattering of neutrons by elastic and inelastic processes into the solid angle subtended by the detector at a scattering angle of 0° .

Statistical Errors

Consider a single channel in the time domain. If the number of events in the channel following subtraction of the analytical background are N_i and N_o for sample-in and sample-out spectra respectively, and the corresponding background contributions are B_i and B_o , then the calculated cross section is expressed as

$$\sigma_T = \frac{-1}{nt} \ln \frac{N_i}{N_o} \quad \text{where } nt = \text{no. of atoms/cm}^2. \quad (4.16)$$

Then
$$\Delta\sigma_T = \left[\left(\frac{\partial\sigma_T}{\partial N_i} \right)^2 \sigma_{N_i}^2 + \left(\frac{\partial\sigma_T}{\partial N_o} \right)^2 \sigma_{N_o}^2 \right]^{1/2} \quad (4.17)$$

Since the statistical error in N_i , (N_o) is the root of the accumulated counts in the corresponding channel, N_i+B_i (N_o+B_o), and no statistical error results from the background subtraction, then the error in the cross-section is:

$$\Delta\sigma_T = \frac{1}{nt} \left[\frac{(N_i+B_i)}{N_i^2} + \frac{(N_o+B_o)}{N_o^2} \right]^{1/2} \quad (4.18)$$

This equation was used in calculating the statistical error in the cross section (section 4.3).

Systematic Errors

The chief source of systematic error arises from the use of an analytical model to describe the background function. Some estimate of the magnitude of this effect is obtained by the value of the χ^2 goodness-of-fit parameter, which is calculated by the computer fitting program. Typical values for χ^2/f for the fit to the time spectra at each pulse height yield a mean of 1.70, $\sigma_{\chi^2} = .45$.

From the definition of the χ^2 distribution, it follows that the average deviation of the fitted function from the experimental background function, is $\sqrt{1.70}\sigma = 1.3\sigma$. Thus, on the average, the systematic error introduced by fitting an analytical background to the experimental curve is $\sim 0.3\sqrt{B_i}$. For

the energy regions where the statistical error is dominated by the background, $B_{i,0} \gg N_{i,0}$, therefore, the systematic error introduced by this source is about 1/3 of the calculated statistical error. In the "best" region, statistically $N_{i,0} \gg B_{i,0}$, the corresponding systematic error is significantly less than this quoted upper limit.

Finally, it is a reasonable assumption that systematic deviations will be similar for the sample-in and sample-out spectra, consequently the transmission will resemble

$$T_i \approx \frac{N_{i,0} - \Delta_i}{N_{o,0} - \Delta_o} \quad \text{where } \Delta_{i,0} = \text{systematic deviation} \quad (4.19)$$

and the net effect of these deviations in individual spectra tends to cancel in the transmission measurement.

A second source of systematic error arises from the calculation of sample thickness (atom/cm²). The sample thickness in this unit is equal to:

$$nt = \frac{N_o}{A} \rho x = \frac{N_o}{A} \frac{W}{\pi r^2} \quad (4.20)$$

ρ = density of sample

A = atomic weight

N_o = Avagadro's number

W = sample weight

r = radius of cylindrical sample.

In most instances, the sample, in powder or liquid form,

is contained in an aluminum can. The errors in weight of the fitted and empty cans are ~ 0.3 gm, resulting in sample weights of ~ 300 gm ± 0.4 gm, or a systematic error of $\sim 0.15\%$. Measurement of the radius of the sample holder yields a value of 3.50 ± 0.02 cm, or a fractional error in the determination of the sample thickness of $\sim 1\%$. Thus the systematic error introduced by this source is significantly less than the statistical and systematic errors from other sources, and can be neglected. An assumption inherent in this calculation is one of constant sample density. Obviously the presence of voids or density gradations in the sample introduces an additional systematic error, which is difficult to measure by techniques less complex than radiographic inspection. Considerable effort was expended towards eliminating this variable, involving careful tamping and packing in constructing powdered samples, silicone sealing of volatile liquid samples (e.g. CCl_4), and inspection of samples during the course of a run for visual signs of uneven packing. In any case, it has been indicated by Foster and Glasgow⁽²⁷⁾ that the effects of small variations in sample density will tend to cancel, and this source of error may be disregarded.

The final source of systematic deviations in the experimental measurement results from the distortions introduced by small-angle scattering into the second detector, the so-called in-scattering correction mentioned with relation to sample

placement in section 3.6. The apparent decrease in the measured cross-section due to singly-scattered neutrons, is given by⁽⁴⁹⁾

$$\frac{\Delta\sigma_T}{\sigma_T} = \frac{\pi}{4} \left(\frac{dL}{L_1 L_2} \right)^2 \frac{\sigma_n(0^\circ)}{\sigma_T} \quad (4.21)$$

The difficulty encountered in applying this correction is associated with obtaining an exact value of the magnitude of the scattering cross-section. Results for the extrapolated value of $\sigma_n(0^\circ)$ for elements in this mass region, obtained from the data of Monahan and Elwyn⁽³⁹⁾ suggest a range of 0.5 → 1.0 bn/sr. Using the upper limit of 1.0 bn, the in-scattering correction in the present geometry is:

$$\frac{\Delta\sigma_T}{\sigma_T} \approx .015 \quad (4.22)$$

Thus the in-scattering correction in the present experiment is of the order of 1.5%, and may be neglected in terms of errors present from other sources.

4.4.2 Errors in energy calibration

The determination of the energy scale involves firstly a calibration of the time scale using the separation of the monitor peaks for the coefficient of slope, and the position of the prompt peak, resulting from Compton-scattered gamma radiation, to locate the time intercept. The time calibration is then used to calculate corresponding neutron energies using

the measurement of the flight path and the relativistic relationship between energy and velocity already described.

The major uncertainties introduced in the energy calibration are present in the transformation from channel position to flight time. The statistical errors result from calculation of the centroids of the prompt and monitor peaks; and systematic errors are present in the assumption of time scale linearity, a distortion of the time scale resulting from timing walk in the first counter, and drifts in the separation of the monitor peaks resulting from instabilities in the electronics used to generate the monitor pulses.

The positions of the monitor peaks calculated in the data analysis over the duration of an experiment have been found stable to within 0.5 channels, an error considerably less than errors from other sources. The stability of these peaks, indicates that the errors resulting from the calculation of the centroids of these peaks and drifts in the monitor electronics are minimal. Similarly, the calculated position of the prompt peak has been found stable to within one channel over the course of the experiments.

The non-linearity of the time-to-pulse height conversion has been shown to result in a distortion of ~ 2 channels over the time scale. Thus the error in the energy calibration resulting from electronic drifting and time scale non-linearity amount to ~ 3 channels, which is equivalent in energy to ~ 15 keV

at 800 keV, ~ 35 keV at 1.4 MeV and ~ 50 keV at 2 MeV.

4.4.3 Error in $(d\sigma/dE)$ - energy resolution

A determination of the energy resolution of the system is of major consequence to the calculation of the widths and amplitudes of resonances in the observed cross-section. Therefore a careful estimate of the resolution is necessary. There are two sources contributing to the overall system resolution: the time resolution of the detection system, and the uncertainty introduced in the neutron flight path by the finite detector thickness.

The time resolution of the system may be assumed constant for all neutron energies, and is equal to the resolution of the observed prompt gamma-ray peak accumulated over all pulse heights of the second counter. An analysis of the experimental spectra indicates a constant system resolution of 2.1 nsec. This value corresponds to the accumulated sum of counts recorded in the peak over the eight runs comprising a single measurement.

The second factor, the effect of finite detector thickness, is more difficult to determine accurately. At all but the lowest energies, its contribution to the overall energy resolution is reduced. An uncertainty in the flight time is introduced by the uncertainty in the location of a neutron interaction within the scintillator. Because of the narrow

beam incident on the first detector, contribution of the first detector to this uncertainty is small, relative to the contribution of the second detector. The response function, in distance, therefore, corresponds roughly to an exponential absorption curve with decay constant equal to the product $n\sigma$ of atoms in the detector, truncated at a distance x corresponding to the detector thickness. The transformation into time space yields

$$R'(t) = \frac{1}{v} R(x) = \frac{t}{D} R(x) \quad (4.23)$$

v = neutron velocity

t = neutron flight time

D = flight path.

Therefore, the contribution of this term to the time resolution is linearly proportional to flight time, and is maximized in the extremum where the corresponding energy resolution is minimized.

The overall resolution function is obtained by the convolution of the intrinsic time resolution with the function $R'(t)$ defined above. For ease of computation, the intrinsic resolution was assumed to have a gaussian form with standard deviation σ , and the resolution function due to flight path uncertainty was assumed rectangular with width equal to tx/D where x is the detector thickness.

The resolution function, analytically, is expressed by

$$\begin{aligned}
 R(t) &= \frac{1}{\Delta} \int_{t-\Delta/2}^{t+\Delta/2} e^{-\frac{(t'-t)^2}{2\sigma^2}} dt' \\
 &= \frac{\text{erf}(t+\Delta/2) - \text{erf}(t-\Delta/2)}{\Delta}
 \end{aligned}
 \tag{4.24}$$

From this function the variance of the resolution function is just equal to

$$\sigma^2(R) = \frac{\int_{-\infty}^{\infty} R(t) t^2 dt}{\int_{-\infty}^{\infty} R(t) dt}
 \tag{4.25}$$

A computer program was written to evaluate the variance for values of the parameter $\xi = \Delta/2.35\sigma$. The integrations were performed numerically using a fixed interval of 0.2σ , and summing to $x = 5.0\sigma$. The ratio $\sigma(R)/\sigma$ is plotted in Fig. (24) as a function of ξ .

From this curve, and the measured time resolution, obtained from the experimental width of the prompt peak, the energy resolution of the experiment was calculated for $0.600 \text{ MeV} < E < 3.0 \text{ MeV}$. This resolution is shown in Fig. (25). The upper curve is an approximate resolution calculated assuming a gaussian resolution function for the flight path uncertainty, and using an overall variance equal to the sum of component variances.

This resolution function is used in the analysis of resonance parameters, discussed in Chapter VII.

FIG.24

ENERGY RESOLUTION FUNCTION OF ξ

THEORETICAL RESOLUTION (UNITS OF FWHM) AS A FUNCTION OF THE RATIO OF THE WIDTH OF THE RECTANGULAR COMPONENT TO THE FWHM OF THE INTRINSIC RESOLUTION.

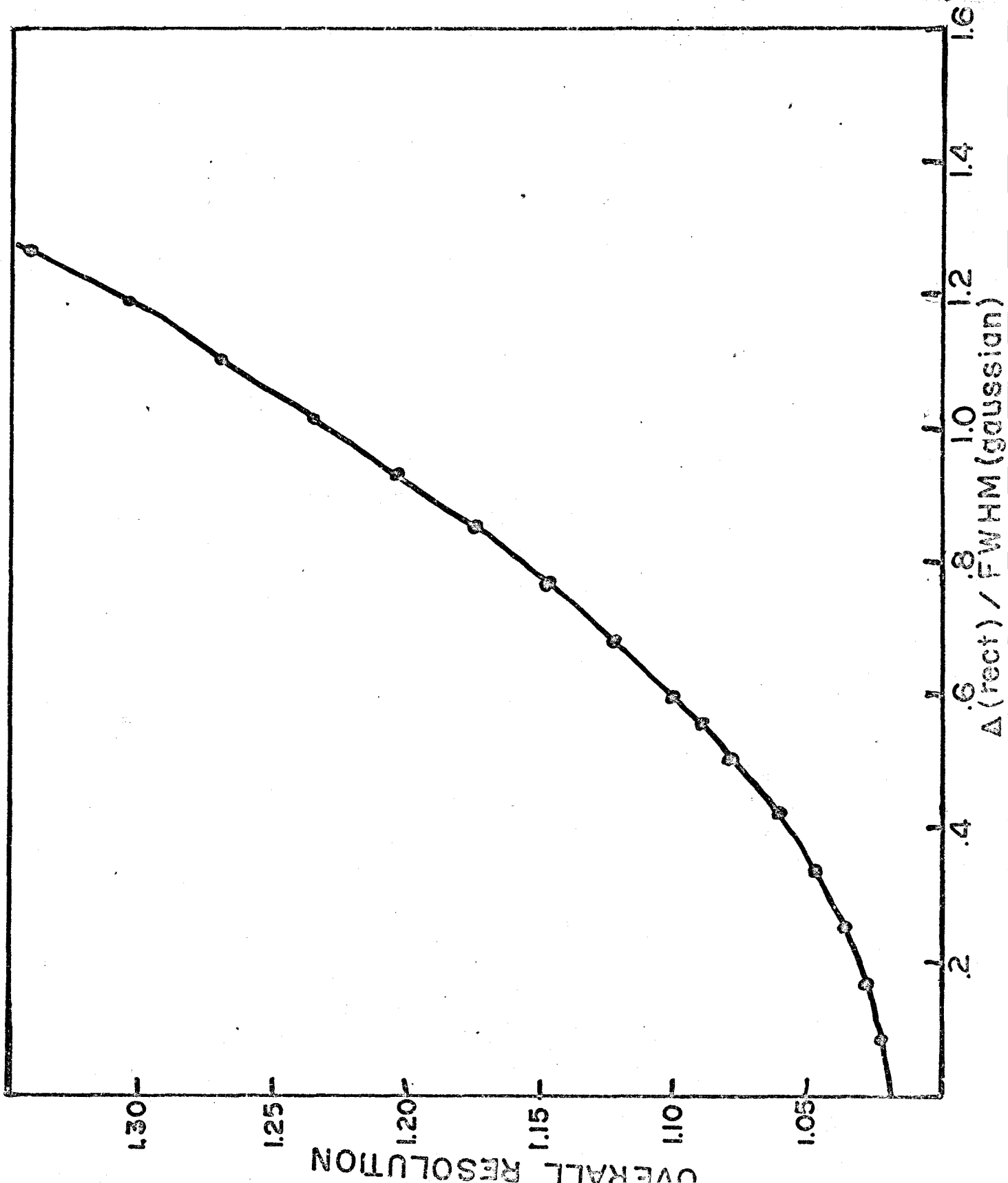
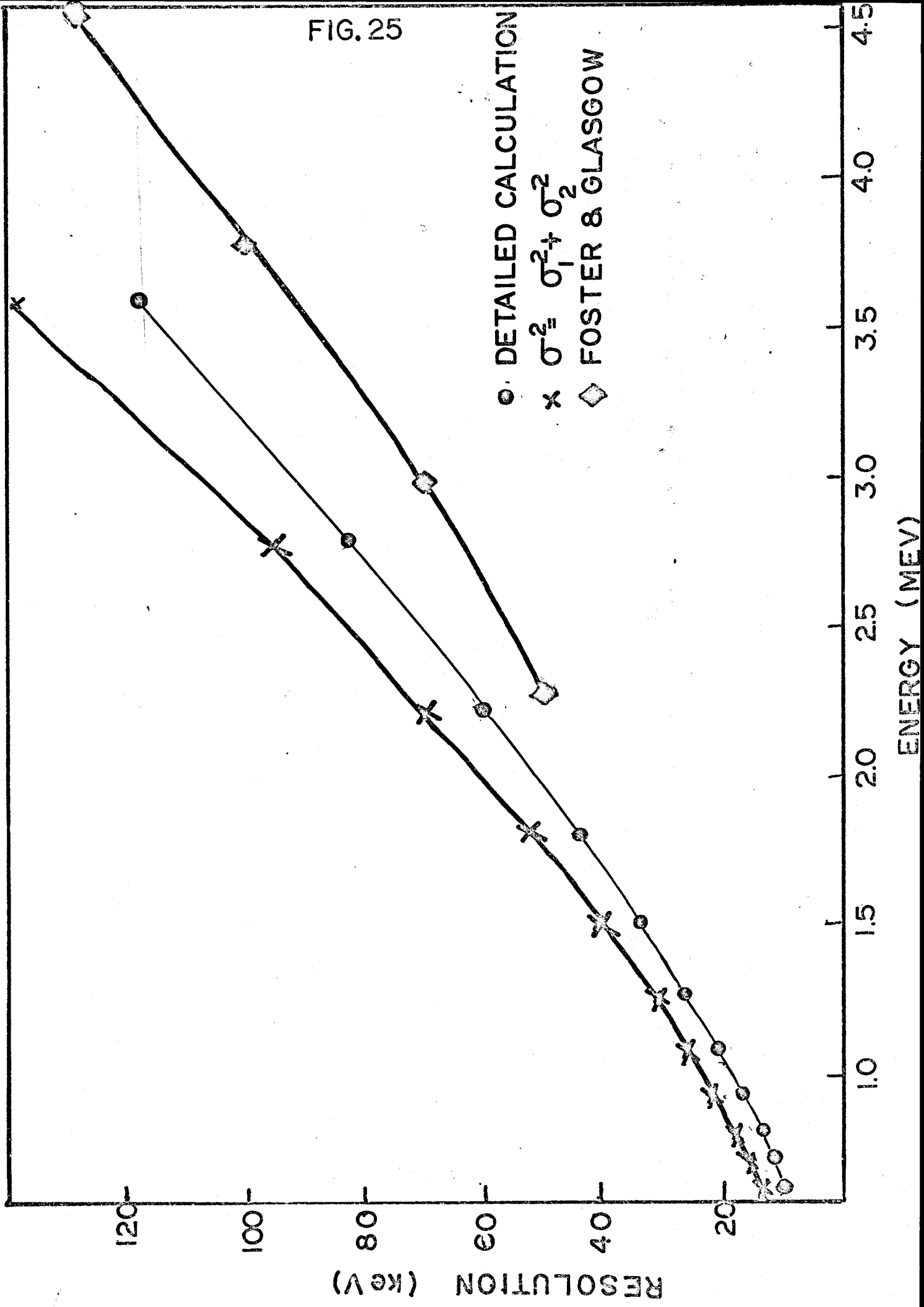


FIG.25.OVERALL SYSTEM ENERGY RESOLUTION.

CALCULATED SYSTEM RESOLUTION OBTAINED BY CONVOLUTION OF GAUSSIAN AND RECTANGULAR FUNCTIONS (CROSSES) AND SIMPLE SUM OF SQUARES (X'S). ALSO ILLUSTRATED IS THE RESOLUTION OF FOSTER AND GLASGOW'S EXPERIMENT.

FIG. 25



CHAPTER V

RESULTS

5.1 Selection of Sample Elements

As one objective of the present investigation was to examine the systematics present in the resonance structure observed in the total cross-sections at energies of a few MeV, samples were chosen in order to provide a continuous mass distribution of cross-section data over a limited region of the periodic table. The region chosen was within the 2s-1d shell, in which comparable data existed for the elements fluorine, sodium, magnesium, silicon, and sulphur. As a check, the first cross-section measured was magnesium, and the results compared favourably with the previous data of Frier et al⁽¹⁸⁾. The elements chosen to study, therefore, were magnesium, aluminum, phosphorous, chlorine, potassium and calcium.

With the exception of Cl, the samples were in the form of granular or powdered elemental form. The chlorine sample was in the form of CCl_4 , necessitating the subtraction of the carbon cross-section, which has been investigated by several authors^(49,50). The encapsulation of the potassium sample presented some difficulties because of the oxidizing properties of the metal, but was circumvented by encapsulating

the molten metal under heated oil, and covering the cooled surface with a thin layer of silicone grease.

The sample thicknesses were chosen to be as near as practical to two half-thicknesses, in some cases being limited by the physical size of the sample container. The thicknesses (in atoms/cm²) are listed in Table 1.

5.2 Experimental Cross Section Results

The experimental data for the cross-sections are shown in Figs. (26) to (31). A qualitative discussion of the features of each cross section will be preceded by some general remarks.

The results from the present experiment show clearly the characteristic form of time-of-flight data, namely a gradual broadening of the energy mesh as one proceeds to higher energies. As a result of this effect, the present data are resolution-limited for energies much above 3.0 MeV. This is not a severe limitation, as the data of Foster and Glasgow^(26,27) provide a coverage to a lower limit of ~ 2.4 MeV, and are included in the present results to provide a continuous measurement to 4.0 MeV.

Additionally, the characteristics of the neutron spectrum utilized in the present experiment are evidenced in the noticeable increase in the statistical error at the low and high energy limits of this data. Statistical errors in the present results vary from a minimum of $\sim .05$ bn $\sim 2\%$ at about

Size of Samples used in Present Experiment

Also shown is a calculated half-thickness based on
an average cross-section of 2.5 barn

Sample	Thickness g/cm^2	Half Thickness (g/cm^2)
Mg	7.154	6.75
Al	10.228	7.50
P	7.391	8.60
Cl	8.697	9.84
K	10.95	10.85
Ca	9.861	11.13

FIG. 26

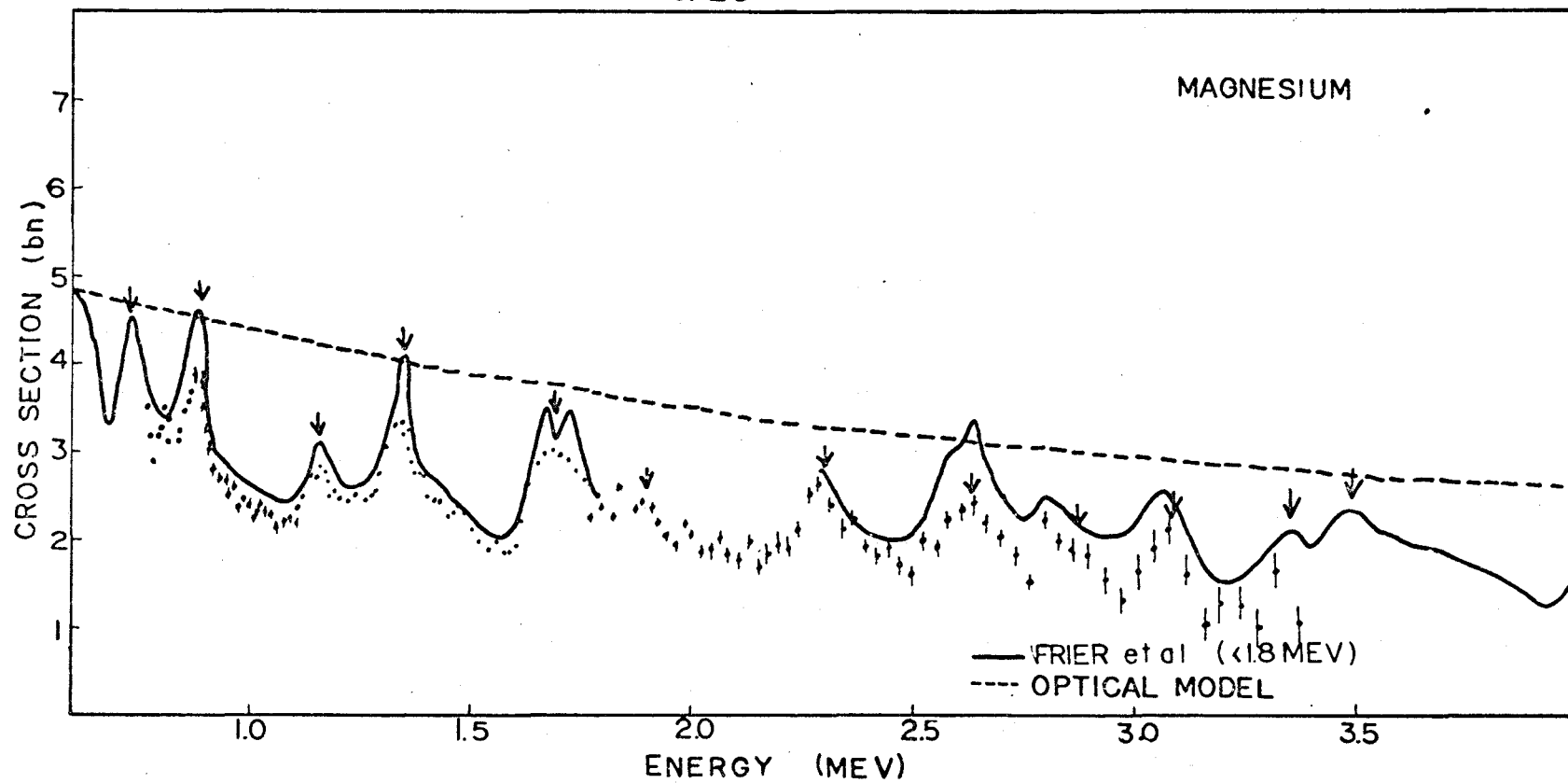


FIG.26 CROSS-SECTION OF MAGNESIUM 0.8-4.0 MEV

FIG 27

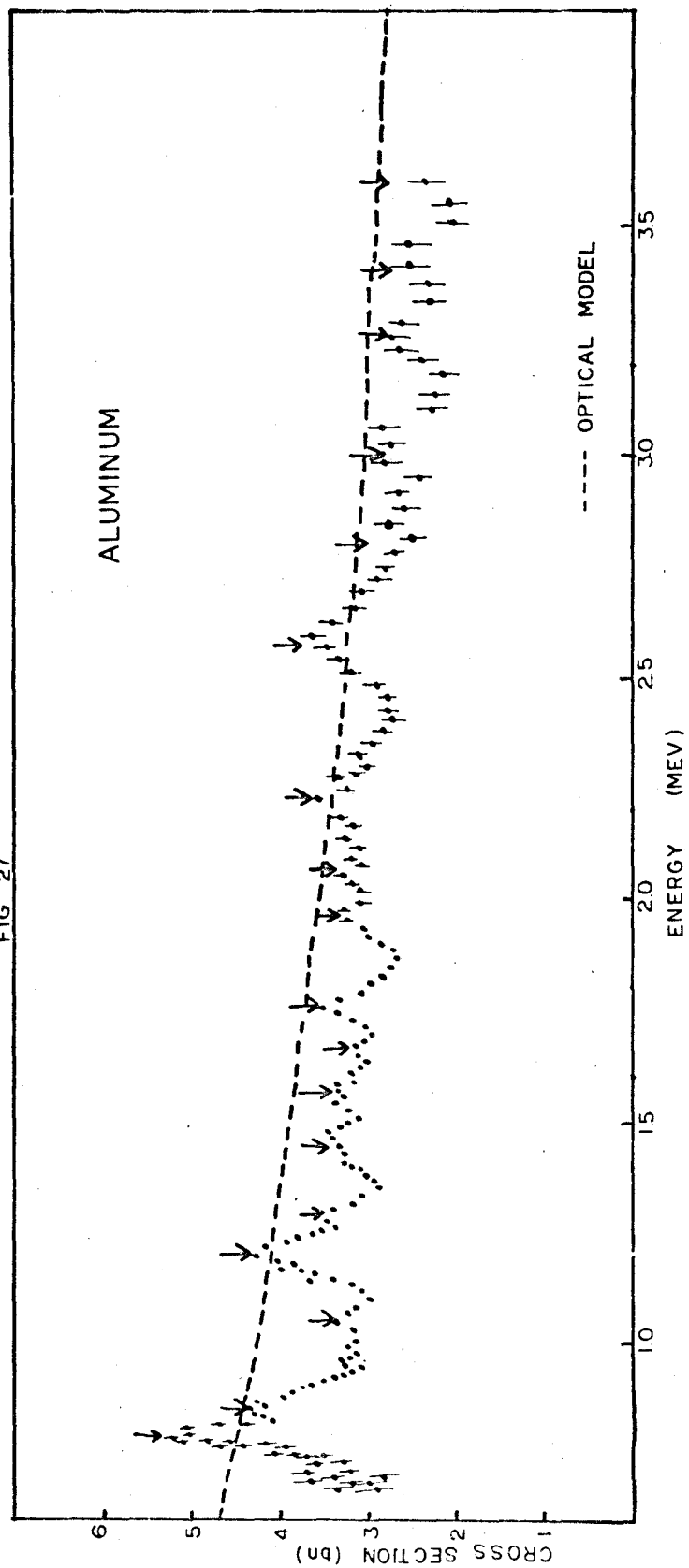


FIG.27 CROSS-SECTION OF ALUMINUM 0.8-4.0 MEV

FIG. 28

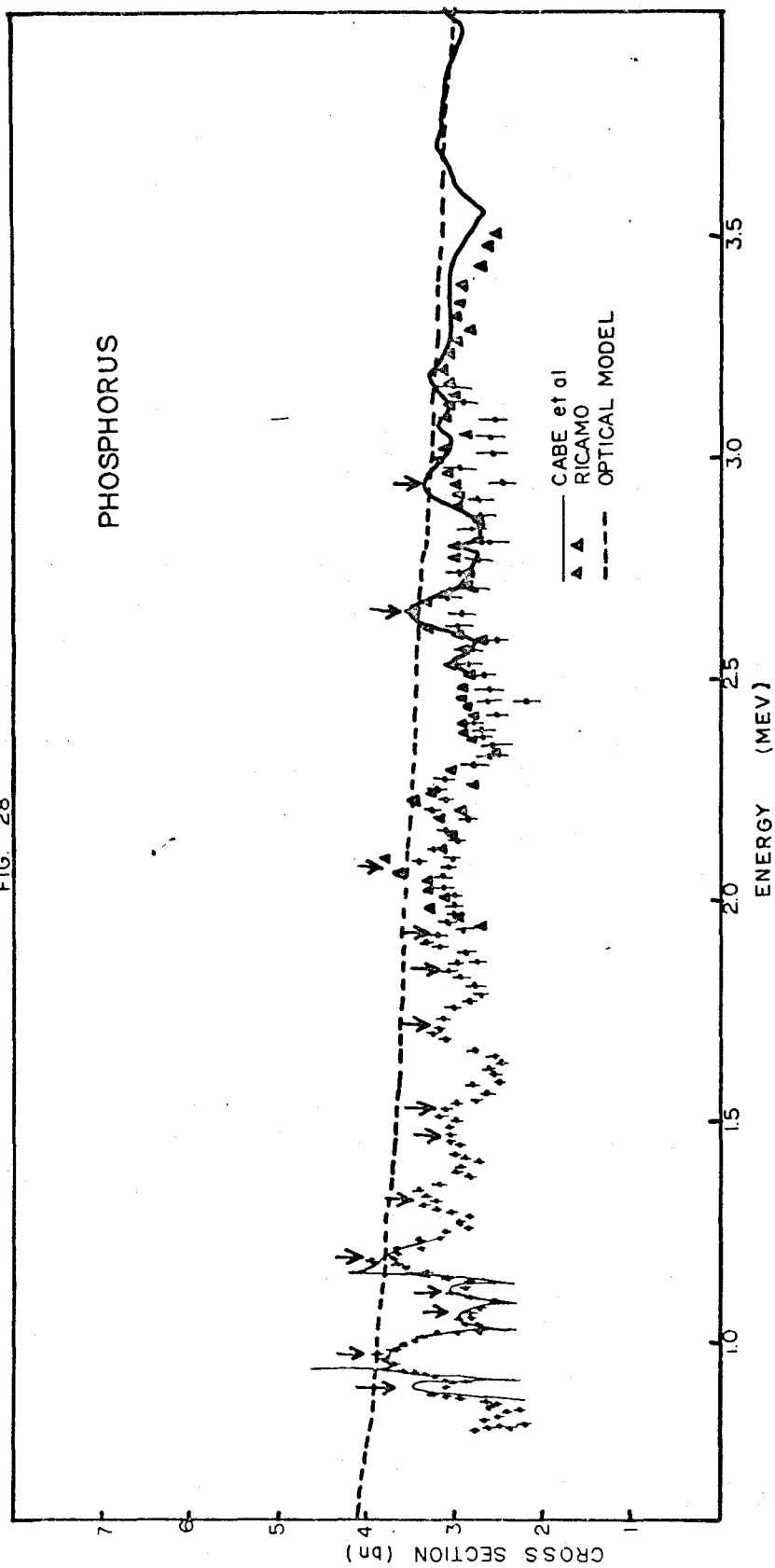


Fig.28 CROSS-SECTION OF PHOSPHORUS 0.8-4.0 MEV

FIG 29

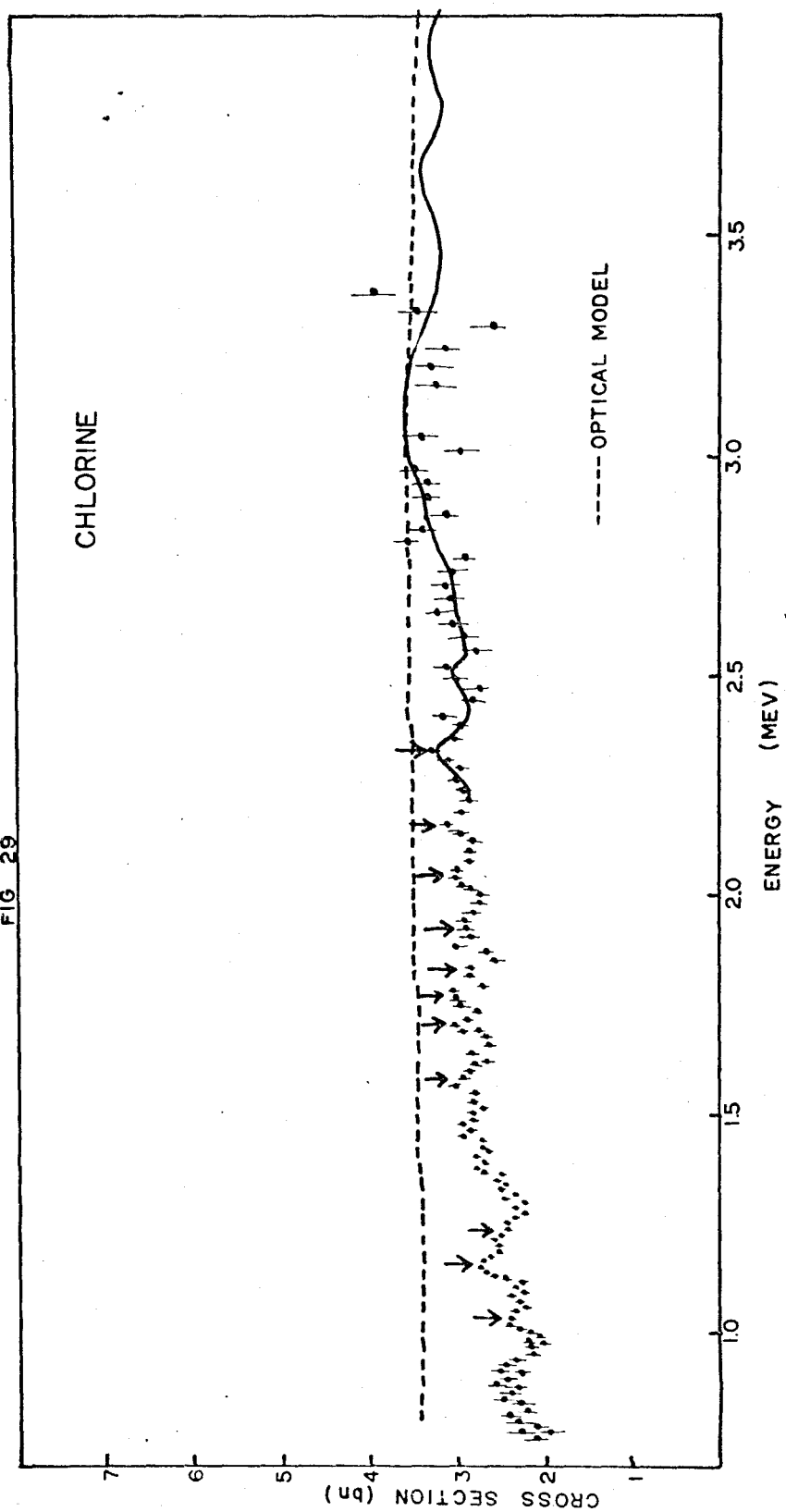


Fig.29 CROSS-SECTION OF CHLORINE 0.8-4.0 MEV

FIG. 30

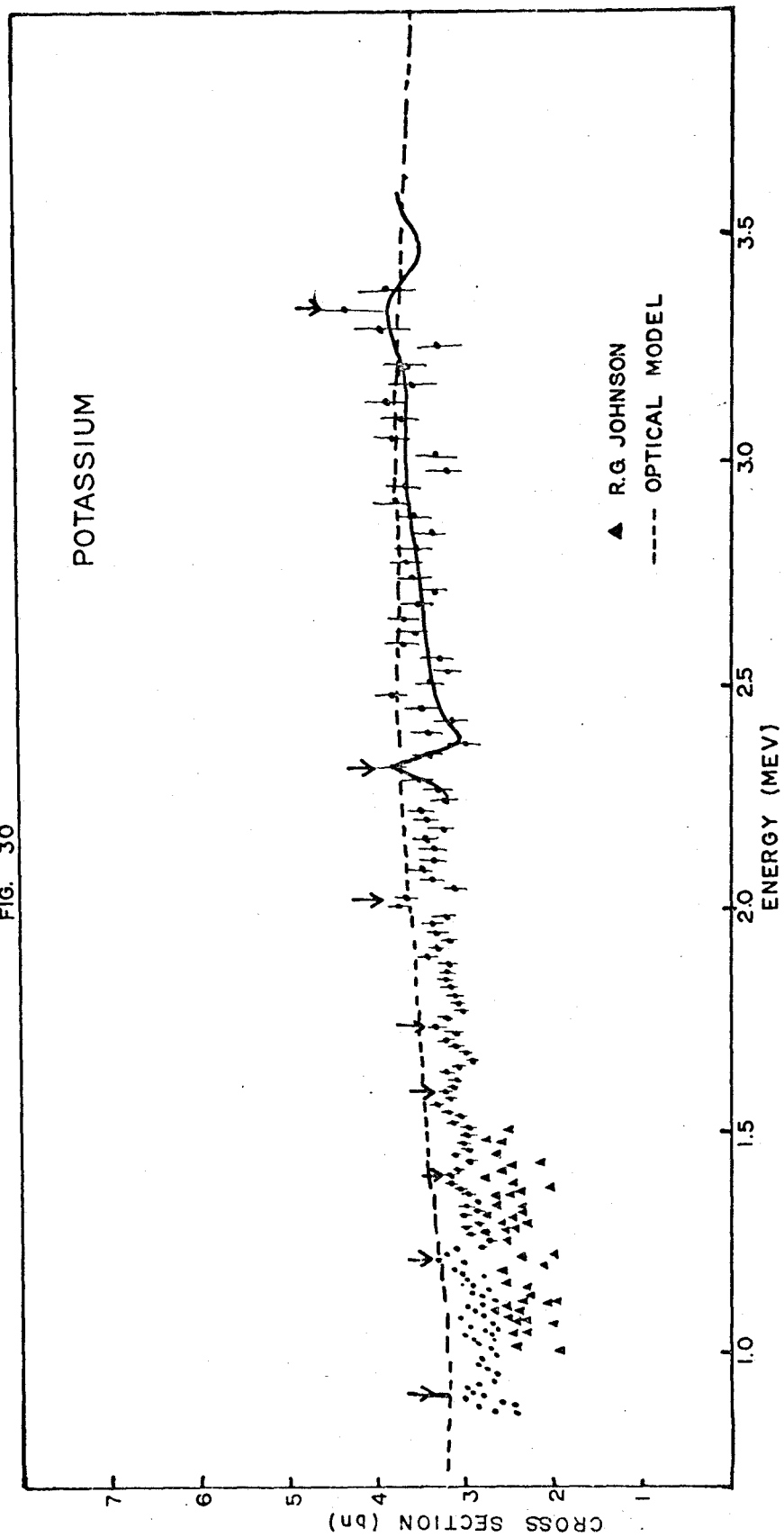


Fig.30 CROSS-SECTION OF POTASSIUM 0.8-4.0 MEV

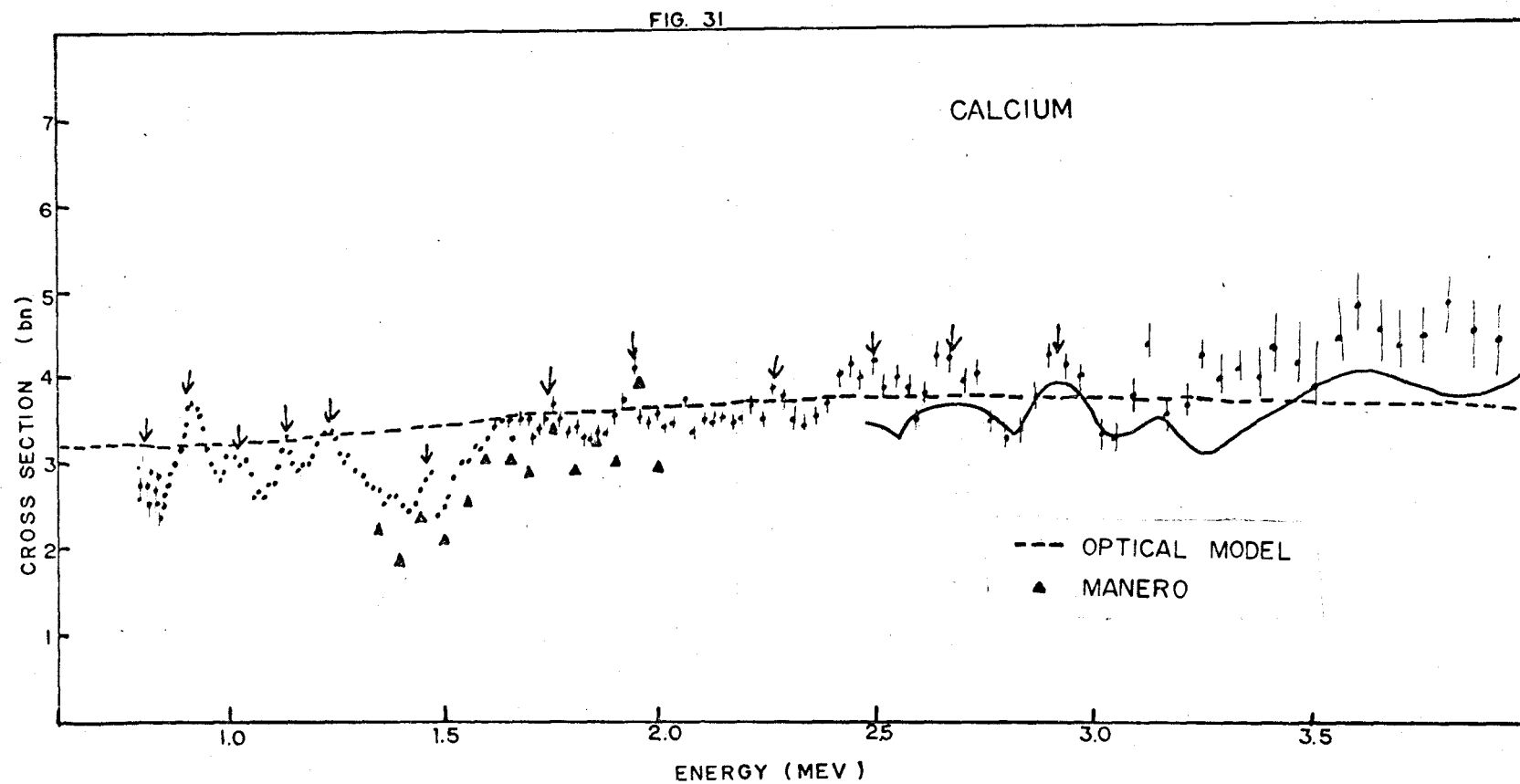


Fig.31 Cross-SECTION OF CALCIUM 0.8-4.0 MeV

1.5 MeV, to a maximum, in the region < 3 MeV of $\sim .4$ bn $\sim 10\%$. An additional systematic error of about the same magnitude is present in these results, as discussed in section 4.4.1.

Where comparable data exists, as in the case of Mg and P over limited energy regions, this is included. The agreement with previous work in these cases is acceptable and provides reasonable confirmation of the derivation of systematic errors in Section 4.

Also shown on these figures are the optical model fits to these data. These are evidenced by a dashed smooth line. The discussion of the calculations leading to these fitted functions will be deferred to Chapter VI.

5.3 Discussion of Individual Cross Section

Magnesium

Magnesium was the first element to be examined, as the data of Frier⁽¹⁸⁾ et al provided a check on the accuracy of the present measurements.

The present data agrees well in magnitude with Frier's results for energies less than 1.8 MeV. It is apparent that our resolution, although comparable, is not quite as good as in the previous work, since the peaks at 880 keV and 1340 keV are lower in magnitude, and the doublet at 1.7 MeV is not resolved. However, the agreement provides confirmation of the validity of the present series.

The data above 2.3 MeV do not agree in magnitude with

previous data as well as the low-energy results. However the discrepancy lies within the limits imposed by statistical and systematic errors in the present data, and the fluctuations in both sets of results indicate comparable resolution.

Aluminum

The aluminum cross-section, although slightly larger in magnitude than the magnesium cross-section, exhibits similar trends with energy, as expected from optical model considerations, and the fluctuations are of a similar order.

No previous comparable low-energy data exists for this nucleus, but the cross-section about 2.4 MeV is in close agreement with the results of Foster and Glasgow⁽²⁷⁾, both in magnitude and in structure.

Phosphorous

The cross-section shows fluctuations of slightly lower magnitude than the previous two nuclides. Additionally, the trend to a lower cross-section at higher energy is absent and the averaged cross-section is virtually flat over the entire energy region.

The data of Cabe, Laurat and Yvon⁽²⁰⁾ in the region from 0.8 → 1.2 MeV is shown for comparison. This very high resolution data showed more prominent "valleys" than the present results, but the resolved resonances agree remarkably well in magnitude. Also shown for comparison is the data of Ricamo⁽²³⁾ above 1.9 MeV. A resonance in their data

at 2.08 MeV remains undetected in the present work, but this may be due either to the relatively poor distribution of experimental points in their work, or to the resolution of the present work, which is comparable with the indicated width of this peak.

Agreement of the present work and Foster and Glasgow⁽²⁷⁾ above 2.5 MeV is fairly good, but this experiment is unable to resolve fine structure from limitations of both statistics and resolution.

Chlorine

The systematics of the chlorine cross-section show a trend to higher values at higher energies, in contrast to the cross-sections of the previous elements. Fluctuations present in this measurement are reduced in magnitude, a feature explained at least in part by the 25% isotopic abundance of the $A = 37$ isotope.

No previous data exists for energies less than 2.5 MeV, and the agreement with Foster and Glasgow⁽²⁷⁾ at higher energies is once again reasonable.

Potassium

The data for potassium repeat the positive trend with energy. The fluctuations present in this measurement are considerably reduced in comparison with other elements, and since potassium is nearly monoisotopic, it is apparent that

some mechanism must exist to explain this phenomenon.

The results of Johnson⁽⁵²⁾ between 1.0 and 1.5 MeV are included. These data are obviously statistically poor and yield information only about the average value of the cross-section. Once again, the fit with Foster and Glasgow⁽²⁷⁾ at higher energies is adequate.

Calcium

The cross-section of calcium shows more prominent resonance structure than the previous two nuclides. Multiple peaks are present, and are well resolved. Comparative data of Manero et al⁽⁵²⁾ from 1.4 → 2.0 MeV are shown, and would indicate that this measurement is systematically lower than the present results by ~ 0.5 bn. The data of Foster and Glasgow⁽²⁷⁾ does not yield this systematic variation, and provides support for the results of the present experiment. Fluctuations in the present data appear slightly enhanced over the work of Foster and Glasgow⁽²⁷⁾ but the fits over all values of the cross-section lie within experimental error of the present work.

5.4 Additional Data

As already indicated, the results obtained in the present experiment were chosen to provide a complete set of cross-section measurements over the mass region from $A = 19$ to $A = 40$. Fig. (32) to Fig. (35) illustrate the previous data for fluorine, sodium, silicon and sulphur. In all cases

FIG. 32

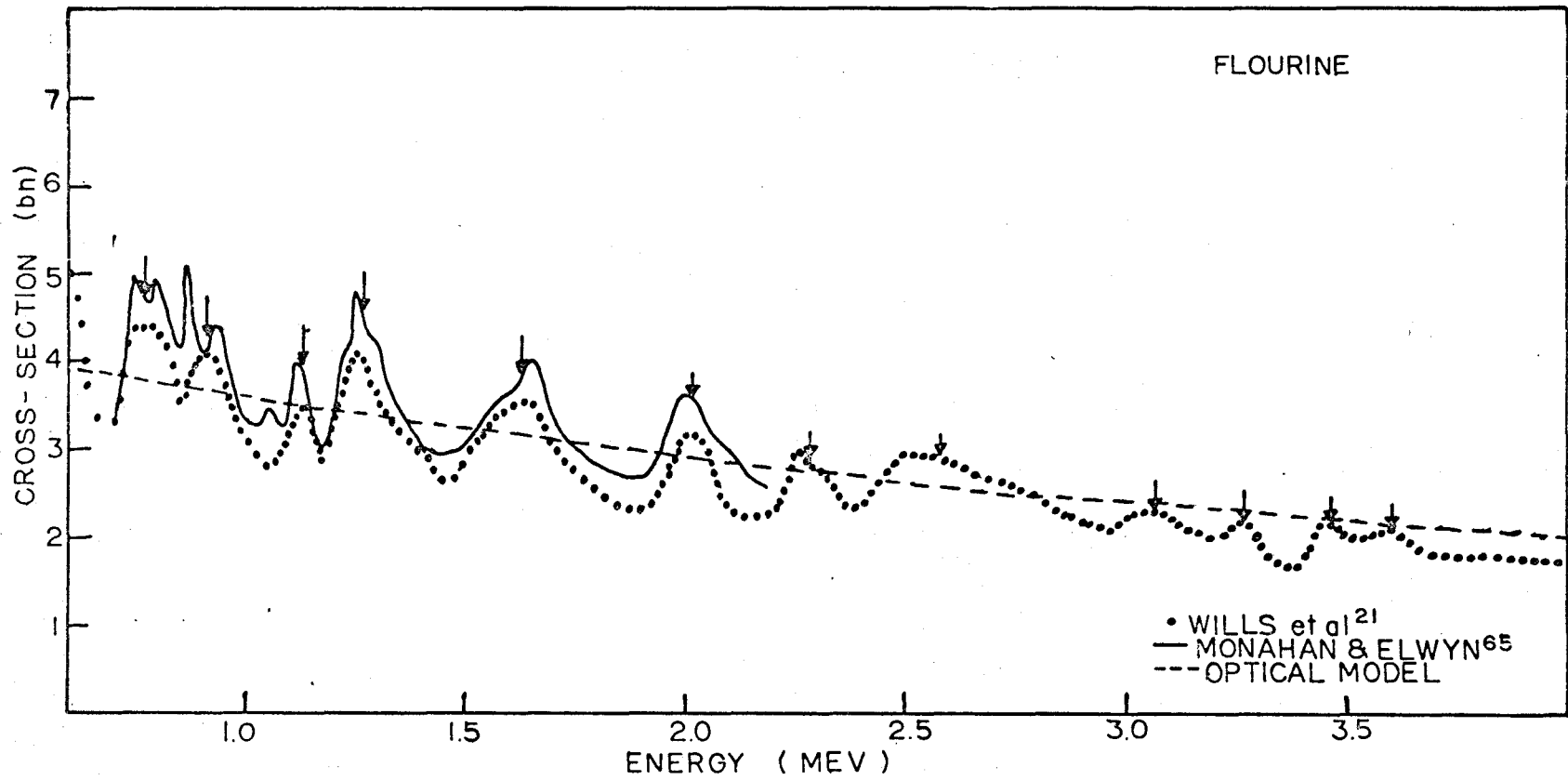


FIG.32 CROSS-SECTION OF FLOURINE 0.8-4.0 MeV

FIG. 33

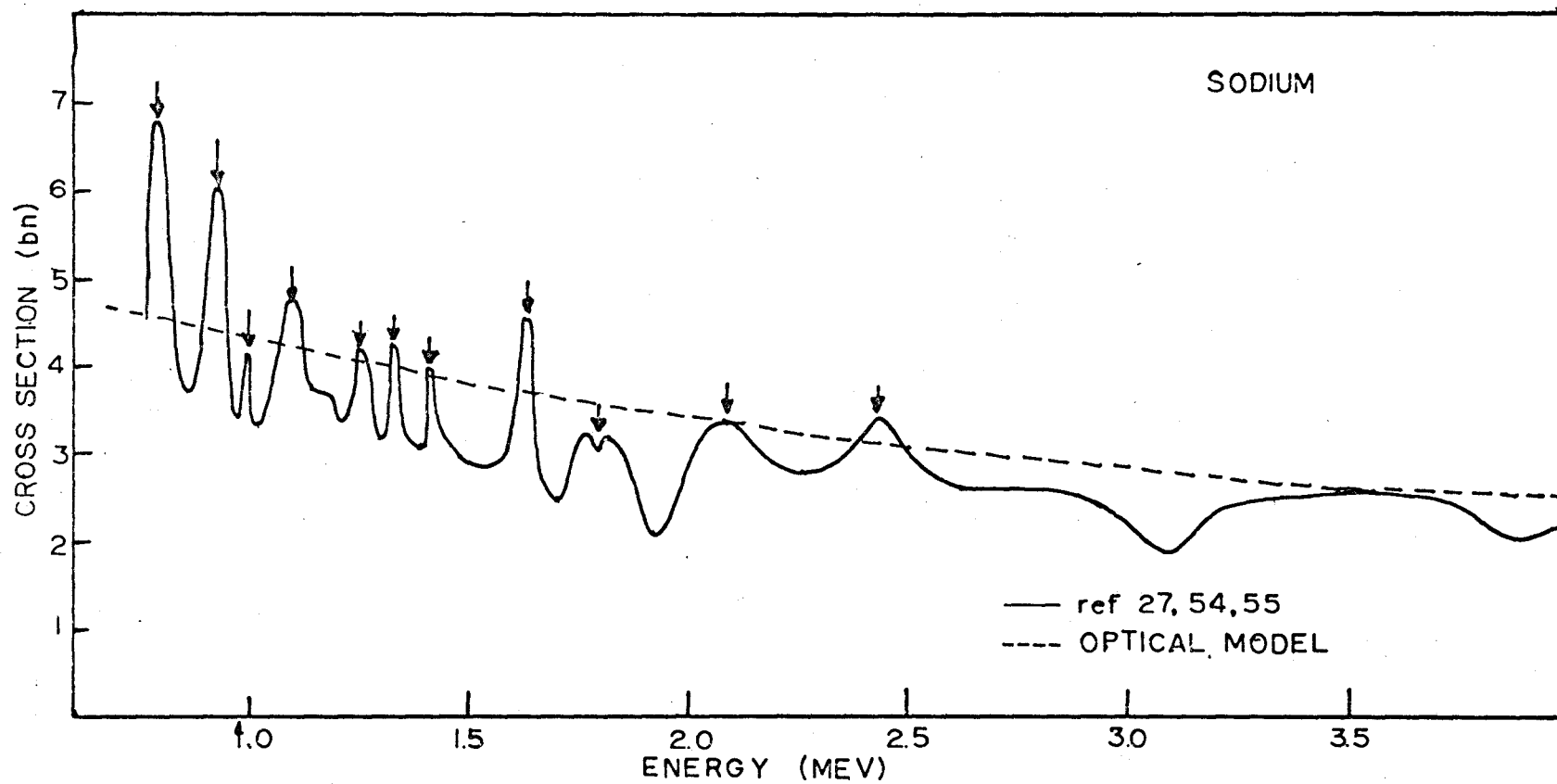


FIG.33 CROSS-SECTION OF SODIUM 0.8-4.0 MEV

FIG 34

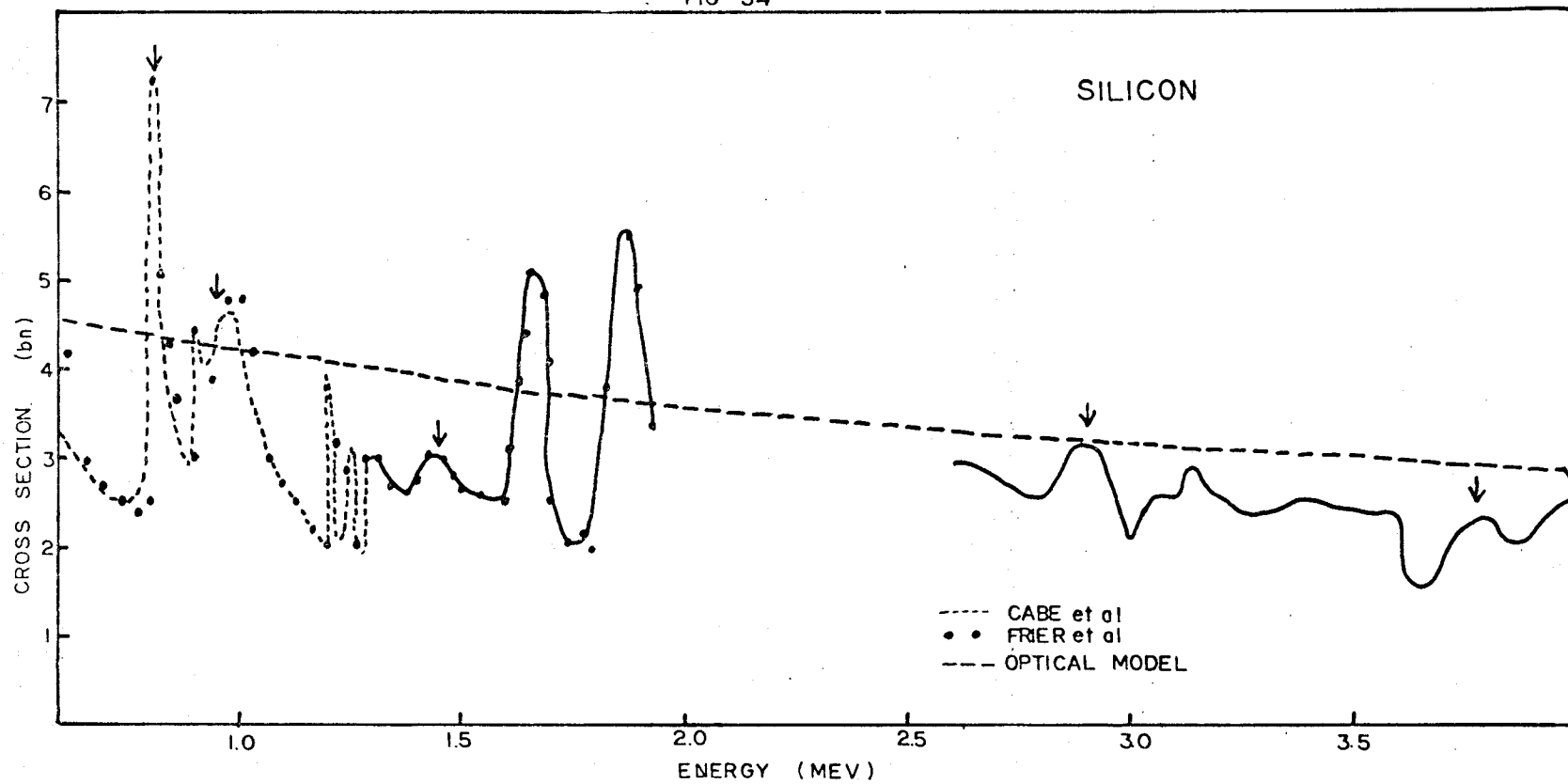


FIG.34 CROSS-SECTION OF SILICON 0.8-4.0 MEV

FIG. 35

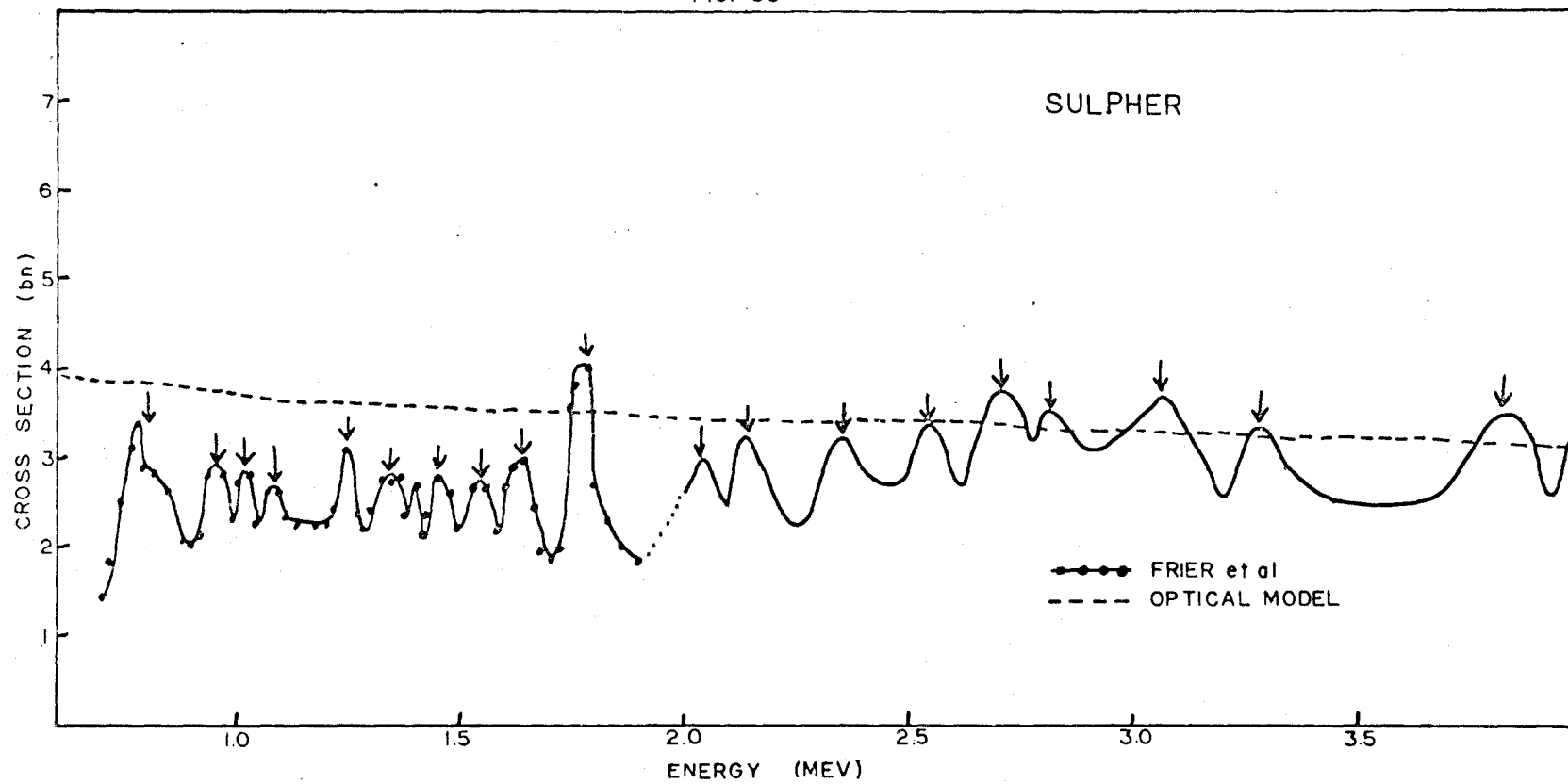


Fig.35 CROSS-SECTION OF SULPHUR...0.8-4.0 MEV

the data above 2.5 MeV are from Foster and Glasgow⁽²⁷⁾, whereas the low energy data is obtained from various sources. These are detailed in the table below.

Table II
Previous Experimental Results in 2s-1d shell

<u>Element</u>	<u>Energy</u>	<u>Author</u>
F ¹⁹	0.5 → 5 MeV	Wills Bair Cohn and Willard ⁽²¹⁾
Na ²³	0.9 → 2.0 MeV	Towle and Gilboy ⁽⁵³⁾ Johnson ⁽⁵⁴⁾
Si ²⁸	0.6-1.8 MeV	Frier et al ⁽¹⁸⁾
S ³²	0.6-1.8 MeV	Frier et al ⁽¹⁸⁾
	1.9-3.5 MeV	Ricamo ⁽²³⁾

No specific qualitative comments will be directed at these data, however several characteristics are evident from a study of the cross-sections presented in this chapter.

(1) A systematic variation of the average cross-section with atomic weight. This property is related to the presence of single-particle resonances, and can be interpreted in the optical model of particle interactions. A detailed analysis of these trends will be deferred to a later chapter.

(2) The presence of prominent resonance structure in all nuclides. This resonance structure has apparent widths of 75 → 100 keV, and lies outside the range of widths expected for

compound nucleus resonances. It is evident that these resonances may be interpreted as "doorway states" from the model of Feshbach⁽²⁴⁾. A more detailed analysis follows in Chapters VII and VIII.

(3) Nucleus-dependent characteristics of the resonance structure.

The magnitude of the cross-section fluctuations varies from a minimum in the case of K and Cl to a maximum for Si. In addition the widths of the resonances apparently are nucleus-dependent, with F^{19} showing broad resonance structure, with average width of ~ 150 keV, and the resonances of S^{32} , for example, are characterized by an average width of the order of 50 keV. The analyses to follow, therefore, are directed to investigating the mechanism underlying these systematic trends in the measured cross sections. In Chapter VI, the behaviour of the average cross-section will be examined by using an optical model potential. Chapter VII will present an analysis of the parameters of individual resonances, and from the distributions of resonance parameters, will show evidence for the interpretation of the resonance structure in terms of the "doorway state" hypothesis. In Chapter VIII, a method will be presented for parametrizing the resonance structure, yielding an experimental strength function estimate using the methods of Fourier analysis and statistical averaging techniques. This strength function estimate will be used to infer certain properties of the distributions of widths and spacings in the

resonance structure, and to compare the experimental results with predicted variations of the doorway state strength function in terms of dependence on mass number, energy, ground state spin, etc.

CHAPTER VI

ANALYSIS OF AVERAGE CROSS SECTION

6.1 Introduction

The historical development of the optical model has been described in Chapter I and II. Perhaps the most conclusive evidence of the success of this model in explaining the average behaviour of nuclear cross-sections lies in the work of Foster and Glasgow⁽²⁷⁾, who, using the Perey-Buck⁽⁴⁾ potential with a single parameter set, satisfactorily fitted the cross section for 78 elements between 2.5 and 1.5 MeV.

However, it was felt worthwhile to extend this analysis to lower energies, at least for the limited mass region reported by the existing experiment. To this end, an existing optical model program developed by Smith⁽⁵⁵⁾ was modified for inclusion of the local approximation to the non-local optical model potential, elimination of parameter search, and elastic scattering coefficients, and inclusion of calculations of total reaction and scattering cross-sections.

6.2 Theoretical

The Schroedinger equation for a nucleon moving in the field of a nucleus has the form:

$$-\frac{\hbar^2}{2m} \nabla^2 \psi(r) + \int V(r, r') \psi(r') dr' = E \psi(r) \quad (5.1)$$

where the kernel of the integral may be visualized as the potential at \vec{r} resulting from the presence of nucleons at \vec{r}' . The non-locality of the potential is a result of the postulated two-body type of interaction, in which the presence of a nucleon at \vec{r} affects the probability of finding nucleons at \vec{r}' in the vicinity of \vec{r} . This then modifies the potential at \vec{r} from the remaining nucleons.

Perey and Buck⁽⁴⁾ chose a separable form for the non-local potential

$$V(\vec{r}, \vec{r}') = U\left(\frac{|\vec{r} + \vec{r}'|}{2}\right) H\left(\frac{|\vec{r} - \vec{r}'|}{B}\right) \quad (5.2)$$

where B is the range of the non-locality.

H was chosen to have gaussian form

$$H(|\vec{r} - \vec{r}'|) = \frac{1}{\pi^{3/2} B^3} e^{-\left(\frac{|\vec{r} - \vec{r}'|}{B}\right)^2} \quad (5.3)$$

which is normalized to unity. The form of the potential dependent on the average position of the two nucleons is:

$$U(\vec{r}, \vec{r}') = (V + iW_I) f_S\left(\frac{|\vec{r} + \vec{r}'|}{2}\right) + iW_D f_D\left(\frac{|\vec{r} + \vec{r}'|}{2}\right) \quad (5.4)$$

where f_S , f_D are the usual Wood-Saxon and Saxon derivative form factors commonly used in optical model calculations, and V , W are the real and imaginary components of the optical potential. From the Pauli exclusion principle, nuclear collisions are excluded deep inside the nuclear surface, consequently, the imaginary term W_I is set equal to zero, and only the

derivative imaginary term, peaked at the nuclear surface, is retained.

A more comprehensive treatment of the interaction contains a local spin dependent term containing a Saxon-derivative form factor. Thus the complete Schroedinger equation is:

$$\left(\frac{\hbar^2}{2M} \nabla^2 + E\right) \psi(r) = -[(U_{so} + iW_{so} S(r) \vec{L} \cdot \vec{\sigma}) \psi(r) + \int U(\vec{r}, \vec{r}') H(|\vec{r} - \vec{r}'|) \psi(r') dr'] \quad (5.5)$$

where $S(r)$ is a normalized derivative Woods-Saxon potential with range a_s , and U , H , are defined by equations (5.3) and (5.4).

The non-local potential presents difficulty in a solution of the wave equation, but there exists a local approximation to this potential which yields virtually identical values of the observable nuclear properties. This approximation, as described in the original paper of Perey and Buck⁽⁴⁾, is a solution to the equation:

$$U_L(r) \exp\left[\frac{MB^2}{2\hbar^2} (E - U_L(r))\right] = U_{NL}(r). \quad (5.6)$$

In the computer analysis, the solution for the local parameters was obtained at each r by an iterative procedure, using as a zeroth order approximation, the first two terms of the Taylor expansion of the exponential. The solution is then obtained iteratively, and after five iterations, the final estimate is obtained by Aiken's delta process,

$$V \approx V_6 - \frac{(V_6 - V_5)^2}{V_6 - 2V_5 + V_4} \quad (5.7)$$

6.2 Solution of Schroedinger Equation

The solution of the wave equation is obtained from the subprogram SCAT supplied by Smith⁽⁵⁵⁾. Essentially the program first solves the wave equation for the internal radial wave function $\psi_\ell(r)$ starting at $r=0$ and proceeding to some radius beyond the nuclear potential. Thus $\psi_\ell(r)$ is a solution of

$$\psi_\ell''(r) + \left\{ k^2 + \frac{2m^*}{\hbar^2} V(r) - \frac{\ell(\ell+1)}{r^2} \right\} \psi_\ell(r) = 0. \quad (5.8)$$

The wave function of a particle outside the nuclear surface is a sum of regular and irregular Coulomb functions F_ℓ , G_ℓ respectively: Thus the asymptotic form is:

$$\psi(R) = F_\ell(R) - B_\ell [F_\ell(R) + iG_\ell(R)] \quad (5.9)$$

where B_ℓ is the "boundary matching constant". Then the requirements of continuity of the wave function and its derivative yield the equations

$$C\psi_\ell(R) = F_\ell(R) - B_\ell [F_\ell(r) + iG_\ell(r)] \quad (5.10)$$

$$C\psi_\ell(R+\delta) = F_\ell(R+\delta) - B_\ell [F_\ell(r+\delta) + iG_\ell(r+\delta)] \quad (5.11)$$

These equations are then solved for B_ℓ . The elastic scattering, absorption and total cross-sections are in turn related to the boundary matching constants by the following equations:

$$\sigma_E = \frac{\pi}{k^2} \sum_{\ell=0}^{\infty} (2\ell+1) 4 |B_\ell|^2 \quad (5.12)$$

$$\sigma_R = \frac{\pi}{k^2} \sum_{\ell=0}^{\infty} (2\ell+1) T_\ell \quad (5.13)$$

$$\sigma_T = \frac{2\pi}{k^2} \sum_{\ell=0}^{\infty} (2\ell+1)^2 \text{Re} B_{\ell} \quad (5.14)$$

where T_{ℓ} , the transmission coefficient, is defined as

$$T_{\ell} = 1 - |1 - 2B_{\ell}|^2 \quad (5.15)$$

Optical model calculations were performed, using the numerical values of potential parameters given in ref. (4), Set A, Table 4, p. 363. These are the same parameters used by Foster and Glasgow⁽²⁷⁾. The cross sections were evaluated in 200 keV steps from 0.600 MeV to 4.0 MeV. Total execution time for all nuclides was 55 sec on the CDC 6400 computer.

6.3 Optical Model Results

Results are shown superimposed as a dotted line on the measured cross-sections in Figs. 26 to 35. The model calculations appear to predict accurately the trends in cross-section, but in some instances, particularly Mg and S, the theoretical calculations lie above the average experimental cross-section by as much as 1 bn. Two effects may account for the discrepancy - the first being the effects of nuclear deformation, which are not compatible with the optical model, and the second being the uncertainty in the experimentally observed average cross section from the resonance structure present in all cases. However, the quality of the fit appears to show little relation to the magnitude of the fluctuations in cross-section, as for example, the neighbouring nuclei Mg^{24}

and Al^{27} , which exhibit similar order of fluctuations, show average deviations from the true cross section of ~ 1.5 bn and ~ 0.7 bn respectively.

Substantiation of the second underlying cause, nuclear deformation, is provided by the excellent fit obtained to the spherical nucleus Ca^{40} . Foster and Glasgow⁽²⁷⁾ have attempted to explain the deviations of the calculated optical model cross-sections in terms of the effect of fluctuations, showing a better fit in this region where fluctuations are reduced. Although this conclusion appears unequivocal at higher energies, support for this statement does not exist in this energy region, for the deviations present in chlorine, the cross-section with the lowest fluctuation, are of the same order as those in aluminum, which shows strong resonance behaviour. Similarly, the cross-sections of sodium and fluorine, which exhibit strong resonances, are closely approximated by the model.

In conclusion, it has been shown that the non local optical potential of Perey and Buck⁽⁴⁾ leads to reasonably adequate predictions of observed cross sections in this mass and energy region, without variation of parameters. Qualitative arguments suggest that the deviations from the fitted function arise chiefly as an effect of nuclear deformation, which is not accounted for by the present theory.

CHAPTER VII

ANALYSIS OF INDIVIDUAL RESONANCES

7.1 Introduction

As mentioned in Chapter II, several experimental investigations have led to the observation of resonances with widths of the order of 100 keV. The authors of these investigations have then pursued analyses directed at establishing these states as doorway states, or alternately Ericson⁽⁵⁶⁾ fluctuations. In an experiment of medium resolution, that is resolution which is significantly larger than the average width of compound nucleus resonances, no clear method exists of differentiating compound nucleus resonances, or alternately statistical fluctuations from doorway states. The situation is perhaps best illustrated by the response of Feshbach⁽⁵⁷⁾ to an interested experimentalist at the International Conference on Nuclear Structure, Antwerp 1962. When asked for clear criteria for identifying a resonance as a doorway state, his reply (paraphrased) was "Anything with width greater than 50 keV probably is, anything with width less than 50 keV, probably isn't".

Clearly, as one proceeds to heavier nuclides, where the compound nucleus width becomes less than 1 keV the interpretation of doorway states becomes easier, in that a multi-

plicity of states with widths of 75 keV, as observed by Seth⁽³⁶⁾, are unexplainable on the basis of Porter-Thomas⁽⁶⁾ or Ericson⁽⁵⁶⁾ fluctuations. However in the 2s-1d shell, compound nucleus widths may be of the order of tens of keV, and the differentiation of intermediate structure from compound nucleus structure becomes more tenuous.

It was with the objective of establishing a clear separation between the resonances observed in these two interactions that a detailed analysis of the distributions of widths, amplitudes and spacings was undertaken.

7.2 Calculation of True Resonance Parameters

The unfolding of the resonance parameters of an observed resonance is not intrinsically obvious in a transmission experiment in which the width of the resolution function is a significant component of the observed width.

To determine the true width, for example, one may approximate the Lorentzian distribution by a Gaussian form, and then obtain the true width from the relationship between variances ie.

$$\sigma_{\text{total}}^2 = \sigma_{\text{true}}^2 + \sigma_{\text{resolution}}^2 \quad (7.1)$$

However the resolution function is normally distributed in transmission space only, and the width measured from the prompt peak applies to the transmission function. A transformation of a resonance dip in transmission into the cross-section domain results in an amplitude dependence of the relation between

true and observed widths. The problem is amenable to an analytical formulation, but the solution of the integral equations necessitates a numerical solution. We consider first the relation between the true and observed amplitudes. For this formulation, we follow the analysis of Merzbacher et al⁽⁵⁸⁾.

The resolution parameter defining the ratio of the resolution to the true widths is:

$$\xi = \frac{\Gamma}{2\sqrt{2}\delta} \quad (7.2)$$

Γ = true width

δ = S.D. of resolution function.

We are assuming a Gaussian resolution function. Although this is not exact in the present case, as the true resolution function is a result of folding a Gaussian intrinsic function with a rectangular function resulting from the uncertainty in flight path (see section 4.4), the approximation does not severely limit the analysis. The observed amplitude of the transmission dip is then the convolution of the Gaussian resolution function with the resonance function (in transmission space). One first defines a reduced transmission in terms of the constant background, σ_c , in the region of the peak and the transmission at the maximum of the resonance dip.

$$Z_{\sigma} = e^{n\sigma} c T(E_0) \quad (7.3)$$

Z_σ , therefore is the ratio of the transmission at resonance to the transmission far off resonance. Then, from the convolution, above, one obtains:

$$Z_\sigma = \frac{2\xi}{\sqrt{\pi}} \int_0^\infty \exp\left(-\xi^2 x^2 - \frac{\beta}{1+x^2}\right) dx \quad (7.4)$$

$$= \frac{1}{\sqrt{\pi}} \int_0^\infty \exp\left(-y^2 - \frac{\beta}{1+(y/\xi)^2}\right) dy \quad (7.5)$$

where $\beta = n\sigma_0$

σ_0 = true amplitude of peak

n = no. of atoms/cm²

Then the ratio of the observed to true cross sections at resonance is just

$$\text{RATIO} = \frac{\log(Z_\sigma)}{n\sigma_0} \quad (7.6)$$

In conventional peak height analysis of compound nucleus resonances, one then uses this ratio in conjunction with the theoretical amplitude of the resonance, which in the case of pure resonance scattering, is a function only of the neutron wave number and the statistical weight g , to extract the neutron width Γ .

However, if one assumes that the states observed in the present measurement consist at least in part of doorway states, in which no simplifying assumption may be made about

the partial widths to the various exit channels, then the amplitude at resonance may not be used as a constraint to yield the total width.

It is therefore necessary to extend the analysis to analytically express the relation between the observed width, resolution width, and true width Γ .

An extension of the preceding analysis to consideration of the convoluted cross section at points off resonance was utilized to extract the observed width.

The experimental reduced transmission at energy $E = E_0 + \Delta$, where E_0 is the resonance energy is expressed as:

$$Z_{\sigma}(\Delta) = \frac{1}{\sqrt{\pi}} \int_{-\infty}^{\infty} \exp\left(-x^2 - \frac{\beta}{1 + \frac{(x+\Delta)^2}{\xi^2}}\right) dx \quad (7.7)$$

The usual method of obtaining the width from a calculation of the second moment of the distribution is not useful in this instance, as the moment integral does not converge. Hence in the present analysis, the experimental width was determined as that value of Δ for which the cross-section, obtained from the logarithm of $Z_{\sigma}(\Delta)$, attains half its value at $\Delta = 0$.

It is evident from the presence of $\beta = n\sigma_0$ within the integral, that there is a coupling between the amplitude of the resonance, and the experimental observed width. There-

fore it is necessary to evaluate the ratio of true-to-observed width for each value of $n\sigma_0$. In fact, it was found that this dependence is not strong, and it was sufficient to evaluate the integral for only a few discrete values of $n\sigma_0$.

Two families of curves were calculated numerically, corresponding to the result of equations (7.6) and (7.7).

- (1) Γ/σ vs $\Gamma_{\text{tot}}/\sigma$ - the ratio of the true width to the standard deviation of the resolution function against the total width/resolution ratio.
- (2) $\sigma_{\text{oexp}}/\sigma_0$ vs Γ/σ - the ratio of the experimental amplitude to true amplitude against true width/standard deviation of resolution function.

These curves are illustrated in Figs. (36) and (37). Also illustrated is the curve obtained by assuming equation (7.1) for the relation between the true and observed widths. It will be noted that for a total width very nearly equal to the observed resolution width, this relation may lead to an error of $\sim 300\%$ in the estimate of the true width. A similar error exists for the ratio of true to observed amplitude in this limit. However, over the major extent of the curves, this relation leads to relatively small errors.

In addition it will be noted that the coupling, through the parameter β , does not result in a large dispersion of the curves, and therefore, a fairly crude estimate of the true peak

FIG.36. RELATION BETWEEN TRUE WIDTH,TOTAL WIDTH,& RESOLUTION.
RATIO OF TRUE WIDTH TO RESOLUTION WIDTH AS A FUNCTION
OF TOTAL WIDTH FOR VARIOUS AMPLITUDES.

FIG. 36

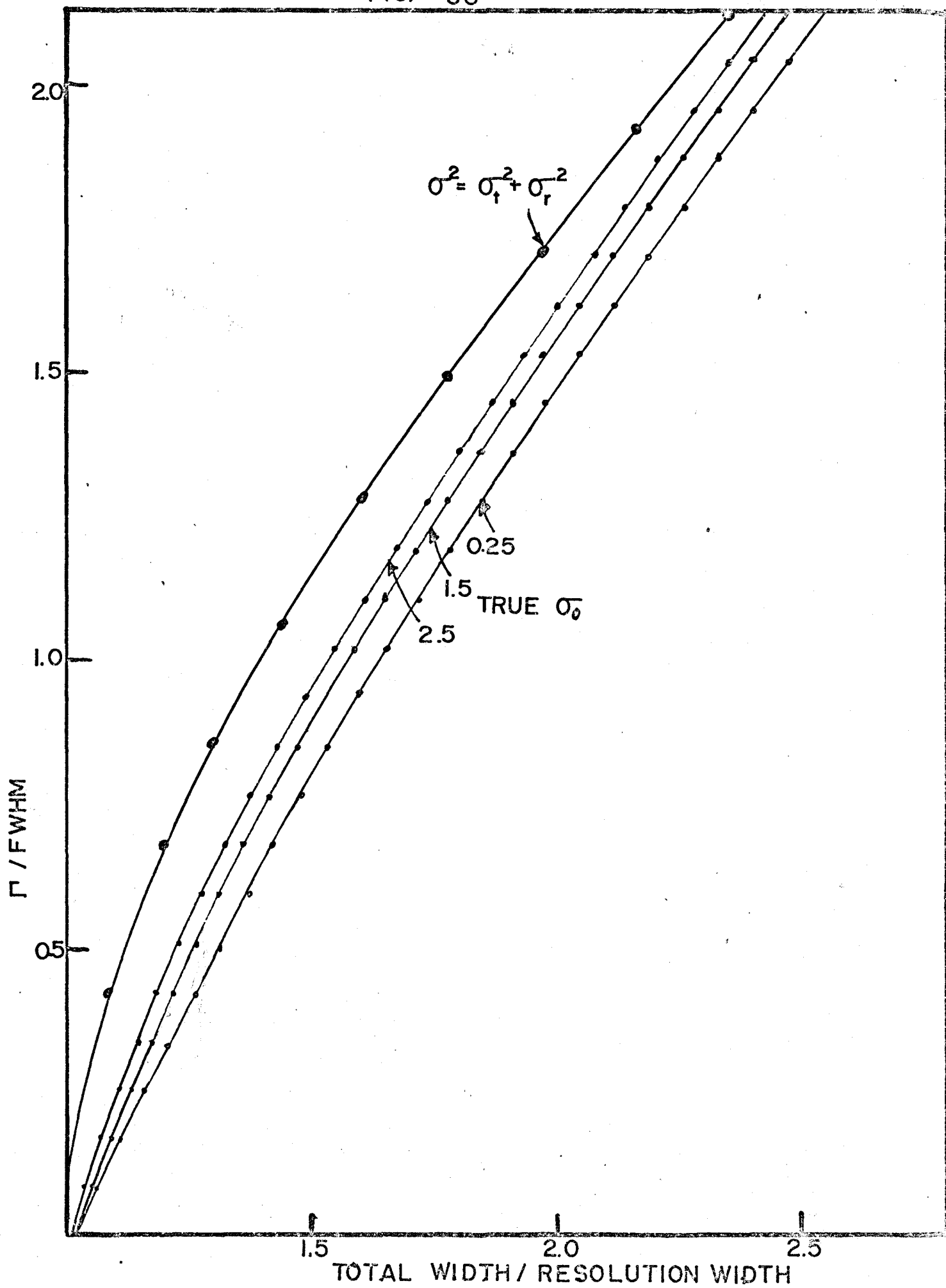
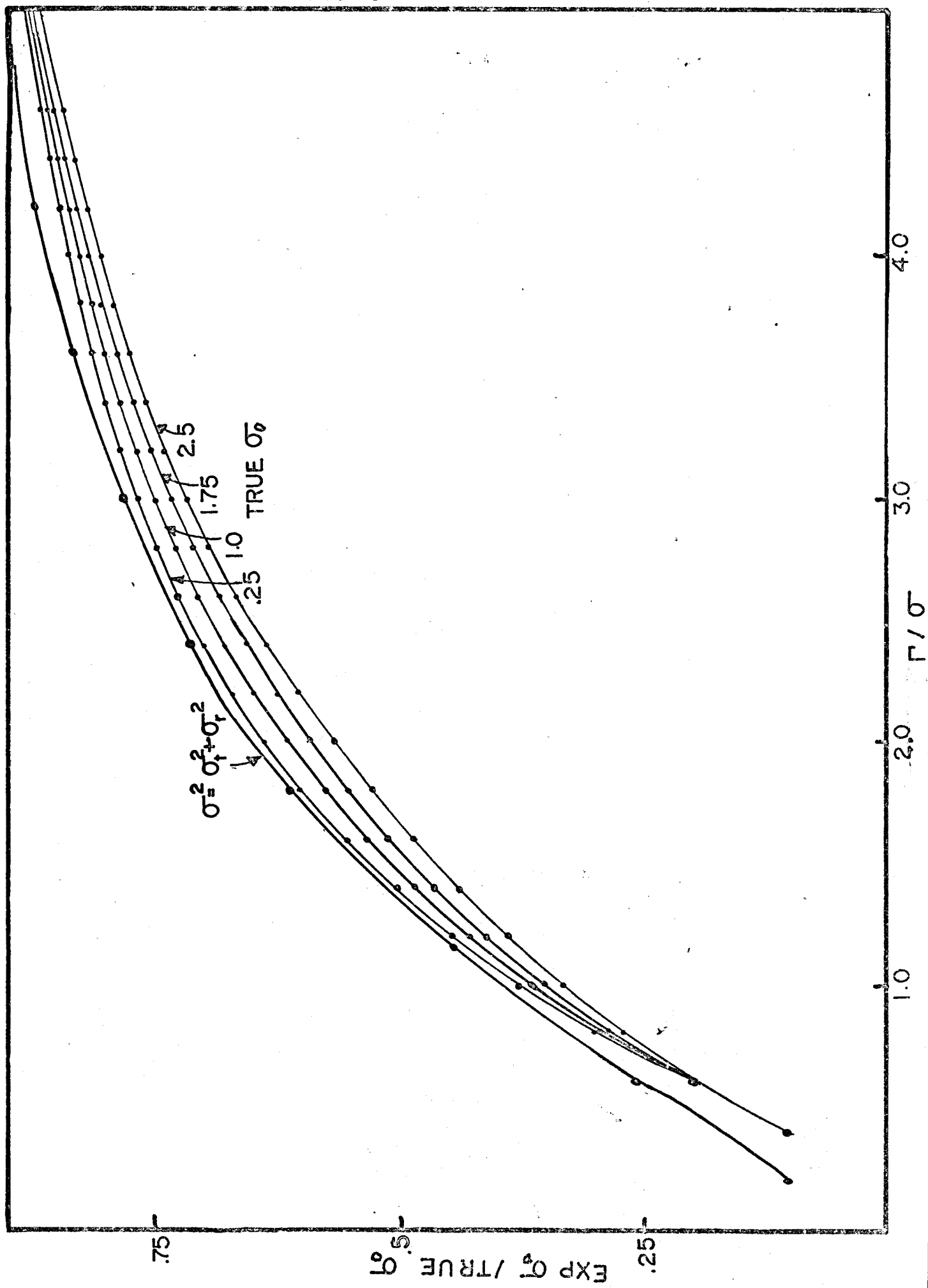


FIG.37. RELATION BETWEEN TRUE AMPLITUDE, OBSERVED AMPLITUDE AND RESOLUTION.

RATIO OF OBSERVED AMPLITUDE TO TRUE AMPLITUDE AS A FUNCTION OF THE RATIO OF TRUE WIDTH TO RESOLUTION WIDTH FOR VARIOUS VALUES OF THE TRUE AMPLITUDE.

FIG. 37



cross-section will not lead to large errors in the determination of true widths and amplitudes.

Experimental widths and amplitudes were determined by visual inspection of the cross-section results. The criterion used to define a resonance involved selecting only those fluctuations which were present over at least three data points. In this manner random fluctuations from statistical effects were not incorporated in these results. Of course, at higher energies, such a peak may still be selected if its presence was confirmed by the measurements of other investigators.

A certain error is introduced by measuring the width as the full-width at half-height of the observed peak, particularly in the case of overlapping resonances, as the relatively slow decay of the Lorentzian function results in a base line shift. Therefore, a better estimate was obtained by considering the baseline as a smooth curve drawn through minimum points located outside the region of overlapping resonances.

The observed resonances are marked by a vertical arrow in the cross-section curves, Figs. (26) to (35).

The procedure used in unfolding the true resonance parameters from the measured width and amplitude was , using the measured amplitude to locate the appropriate curve on Fig. (36) to obtain the true width from the measured width and resolution (the latter from Fig. (25) or from other experi-

menters' reports). This width was then used on Fig. (37) to obtain the true peak cross-section. If this value differed widely from the experimental peak cross-section, the new value was used to re-define the appropriate curve on Fig. (36), and the true width and amplitude were obtained iteratively.

The widths and amplitudes of all resonances observed for the ten nuclides in the present study from 800 keV to 4 MeV are listed in Table III. Approximately one hundred and fifty resonances were located in this region.

7.3 Distribution of Widths

An examination of the widths tabulated in Table III indicates that resonance widths are dispersed over a wide range from zero to greater than 150 keV. To investigate further the distribution of widths for each element, a histogram was constructed, which is illustrated in Fig. (38).

Although the numbers are small in each histogram, certain features are evident in an examination of these distributions. Perhaps the most interesting is that the expected clear separation between compound nucleus states, with widths of 10 keV or less, and doorway states, with average widths of ~ 100 keV is only present in Ca^{40} , in which several states of widths less than 10 keV are present followed by a gap between 20 and 60 keV, then an irregular distribution with calculated mean width of 97 keV. The distribution for Cl is

Table III

Widths and Amplitudes of Resonances 800keV-4000keV

Element	Energy (MeV)	Width (keV)	Amplitude (bn)	Element	Energy (keV)	Width (keV)	Amplitude (bn)
F	0.77	120	1.5	Al	0.79	50	2.4
	0.92	100	1.2		0.85	100	1.2
	1.13	60	0.8		1.05	35	.4
	1.26	120	1.4		1.20	105	1.2
	1.62	170	1.0		1.29	45	.6
	2.02	110	0.95		1.44	80	.5
	2.28	110	0.8		1.56	65	.6
	2.58	360	0.8		1.66	30	.5
	3.06	160	0.5		1.76	60	1.0
	3.26	90	0.5		1.96	50	.9
	3.46	90	0.5		2.06	45	1.0
	3.60	120	0.25		2.23	145	1.0
Na	0.79	40	3.0	Si	2.57	135	1.3
	0.93	40	2.5		2.80	25	1.5
	1.10	70	1.4		3.00	105	.5
	1.25	35	1.0		3.21	40	1.3
	1.33	20	1.2		3.42	55	1.0
	1.41	25	1.0		3.62	50	.9
	1.63	30	2.0		0.81	<10	
	1.80	140	1.0		0.95	140	2.4
	2.09	160	0.8		1.45	105	0.5
	2.44	100	0.8		1.66	51	3.8
Mg	0.88	40	1.3		1.87	95	3.5
	1.15	50	0.9				
	1.34	105	1.3				
	1.68	160	1.2		2.90	87	1.7
	1.90	75	0.8		3.78	90	1.2
	2.30	105	0.8		4.00	130	1.4
	2.64	120	1.0				
	2.86	50	1.15				
	3.08	45	1.8				
	3.35	100	1.1				
	3.50	105	1.4				

(continued next page)

TABLE III (cont'd)

Element	Energy (MeV)	Width (keV)	Amplitude (bn)	Element	Energy (MeV)	Width (keV)	Amplitude (bn)
P	.895	43	1.2	Cl	1.03	44	.9
	.970	110	1.4		1.15	65	1.4
	1.065	17	0.9		1.23	40	.6
	1.115	10	1.2		1.39	47	1.0
	1.190	72	1.4		1.47	91	1.1
	1.320	75	.85		1.58	69	.9
	1.470	70	.6		1.70	40<<	
	1.53	25	1.50		1.77	40<<	
	1.72	80	.90		1.83	44<<	
	1.84	45	.90		1.92	50	.9
	1.91	20	2.4		2.05	50<<	
	2.06				2.16	50<<	
	2.66				2.33	32	1.4
	2.94				3.65	50	1.25
S	0.80	105	0.9	K	0.90	47	.5
	0.95	25	1.5		1.21	60	.5
	1.10	20	1.2		1.40	60	.35
	1.18	20	.85		1.58	63	.4
	1.25	20	2.3		1.74	21	1.0
	1.34	40	1.0		2.20	10<	
	1.45	40	1.0		2.32	10<	
	1.54	40	.9	Ca	3.33	100	.55
	1.64	45	1.3		0.80	65	.55
	1.77	45	2.9		0.91	90	1.4
	2.04	95	1.1		1.02	75	0.8
	2.14	67	1.5		1.14	13	1.8
	2.36	47	1.1		1.24	120	1.1
	2.55	54	1.3		1.46	11	2.2
	2.70	75	1.8		1.76	<10	
	2.81	25	2.9		1.95	<10	
	3.06	130	1.45		2.27	<10	
	3.28	33	2.5		2.50	161	.75
	3.82	80	2.3		2.68	75	1.2
	4.00	<20			2.92	87	1.4

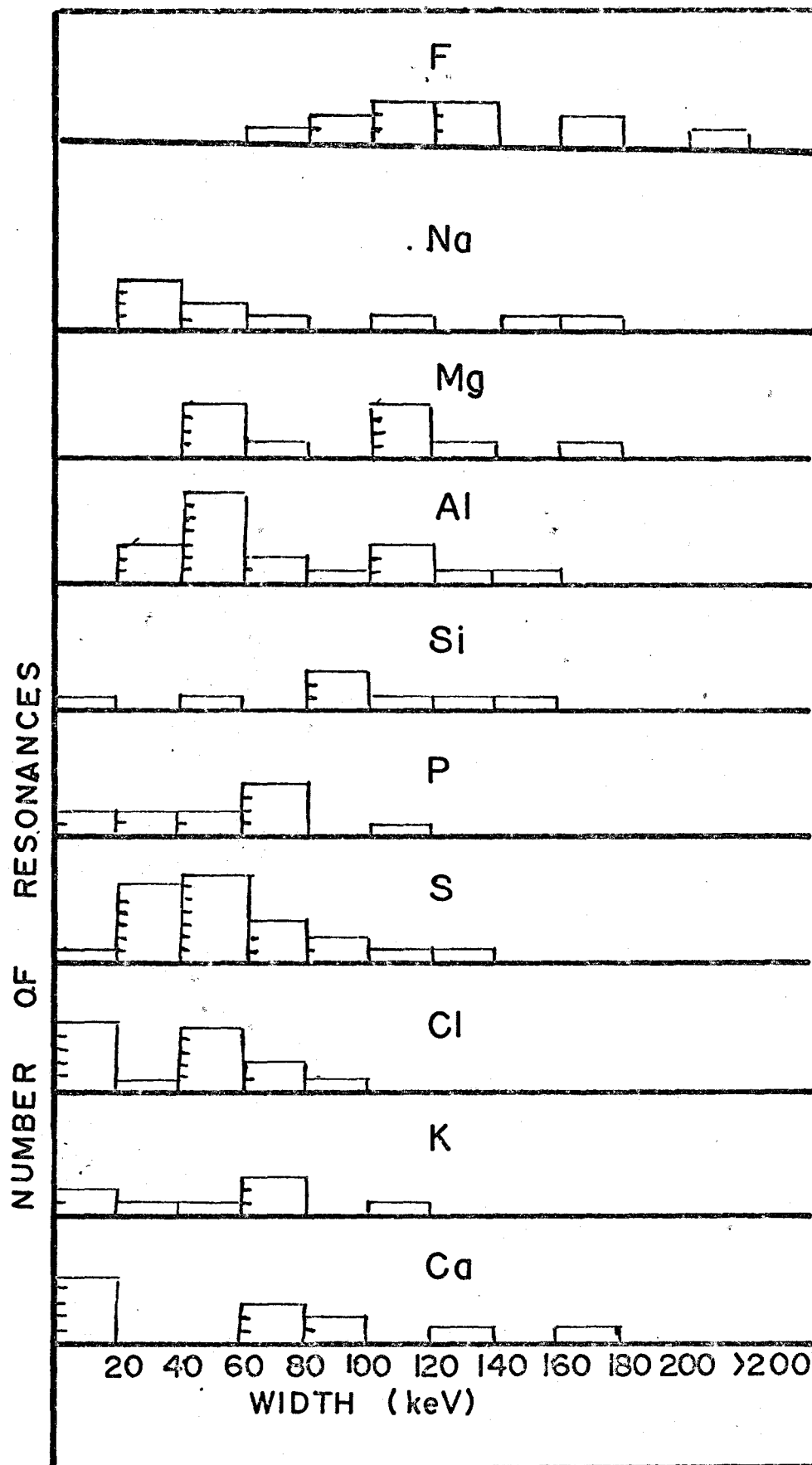


FIG.38

DISTRIBUTION OF RESONANCE WIDTHS A=19 TO A=40

similar, although the mean of the "doorway" state distribution is at about 60 keV, not the postulated 100 keV. Finally F^{19} clearly shows a preponderance of states with mean width of ~ 130 keV, but narrow resonances are entirely absent from this distribution. Although the experimental resolution reduces the detection efficiency for narrow resonances, this has no bearing on the discussion to follow which uses other high resolution data to investigate this region.

It is apparent from these distributions that a mean width of ~ 100 keV does not uniquely define doorway state resonances, or if in fact this is the characteristic width of such resonances, there remain a large number of resonances with widths of $20 \rightarrow 80$ keV of undetermined origin.

To resolve this apparent anomaly, it was necessary to investigate further the properties of the distribution of widths of compound nucleus resonances.

7.4 Widths and Spacings of Compound Nucleus Resonances

The theory underlying the existence of a compound nucleus state indicates that this quasi-bound state should consist of a large number of configuration mixtures of single particle states separated in energy by a few electron volts. There it is expected that the amplitude of each state $\gamma_{\lambda c}$ should be randomly distributed. The distribution of these amplitudes, and the resulting resonance widths, has been suggested by Porter and Thomas⁽⁶⁾. It is postulated that these amplitudes will have a Gaussian distribution centred about zero. Then the width of the associated level, which is pro-

portional to the square of $\gamma_{\lambda c}$, will be a χ^2 distribution with one degree of freedom.

$$P(x)dx = \frac{1}{\sqrt{2\pi}} \frac{x^{-1/2}}{2} e^{-x/2} dx \text{ where } x = \Gamma / \langle \Gamma \rangle_c \quad (7.8)$$

The subscript c indicates the exit channel c.

Now if, in fact n channels are open to decay from the compound nucleus, the distribution of widths corresponds to a χ^2 distribution with n degrees of freedom.

$$\text{Thus: } P_n(x)dx = \frac{n}{2} \frac{(\frac{nx}{2})^{\frac{n}{2}-1}}{(\frac{n}{2})^{\frac{n}{2}}} e^{-\frac{nx}{2}} dx \quad x = \frac{\Gamma_{\lambda}}{\langle \Gamma_{\lambda} \rangle} \quad (7.9)$$

Relating this result to the present analysis, if the average width of compound nucleus resonances were known from high resolution experiments, it would be possible to estimate the probability of obtaining states with widths of the order observed in the present analysis. Further, from such an experiment, the average spacing, and hence the number, of compound nucleus resonances within an energy interval could be extracted. Thus the predicted number of compound nucleus resonances at each width interval could be extracted from such an experiment.

The compound nucleus width distributions are dependent upon the number and type of decay channels available. It is well established that the interaction of neutrons with energy less than a few MeV consists of about 85% elastic scattering,

with the remainder predominantly inelastic scattering to excited states of the residual nucleus. At any rate the distribution corresponding to only one exit channel, the "Porter-Thomas" distribution, has the maximum dispersion, and leads to a "worst-case" estimate of number of states with $\Gamma \gg \langle \Gamma \rangle_c$. Thus in the present analysis, this distribution will be assumed for an estimate of numbers of compound nucleus states.

Hibdon⁽¹⁹⁾ and co-workers have investigated cross-sections of F^{19} below 300 keV, Al^{27} below 500 keV, and Ca^{40} below 700 keV using a resolution of ~ 1 keV. Therefore for these three cases, an accurate estimate of widths and spacings of compound nucleus resonances below several hundred kilovolts exists. To extrapolate these data to the region of interest of the present experiment, however, knowledge of the behaviour of the average widths and spacings as a function of excitation energy is necessary.

Energy Variation of Level Density

It is unnecessary in the present context to give a detailed review of the theory applied to the variation of level density as a function of excitation energy. Many experimental results have been fitted in terms of the semi-empirical formula⁽³³⁾

$$\omega(E) = C \exp 2(aE)^{1/2} \quad (7.10)$$

where $\omega(E)$ = level density

C, a are empirical parameters

E = excitation energy.

The parameter " a " for $15 < A < 70$ is given by Heidmann and Bethe⁽⁵⁹⁾

$$a = 0.035 (A-12) \text{ MeV}^{-1} \quad (7.11)$$

In the present analysis, the level density of compound nucleus resonances was determined by an average of the Hibdon data, and this value substituted in equation (7.10), using " a " from (7.11) to obtain the parameter C . These experimental parameters were then used to extrapolate to the excitation energy of the present experiment.

Energy Variation of Compound Nucleus Widths

In the region under a few MeV, the interaction of neutrons with nucleus is predominantly elastic scattering. Hence, using the Breit-Wigner formula, the half-width of a compound nucleus, Γ , is approximately equal to Γ_n , the width for neutron emission.

Now the width of a resonance is related to the mean lifetime of the corresponding state. Considering a simplistic picture of a neutron escaping from a square potential well, the probability of escape at each collision is⁽⁶⁰⁾:

$$\frac{N_\ell 4kK}{(k+K)^2} \approx 4N_\ell \frac{k}{K} \quad (7.12)$$

where $K \gg k$ are the neutron wave numbers inside and outside

the well, and N_ℓ is an ℓ -dependent function of k and the nuclear radius. For $\ell=0$ $N_0 = 1$, and for $\ell=1$

$$N_1 \approx \frac{E(A^{2/3}/8)}{1 + \frac{EA^{2/3}}{8}} \quad (7.13)$$

Thus for s-wave neutrons, the energy dependence of the average width, based on this simple model is proportional to $\frac{1}{k} = \sqrt{E_n}$. For p-waves, this term is modified by a monotonically increasing, slowly varying function of E_n .

This formulation leads to the familiar concept of the reduced width of a compound nucleus resonance.

$$\Gamma_n^0 = \Gamma_n \left(\frac{E_0}{E_n} \right)^{1/2} \quad \text{where } E_0 \text{ is the reference energy,} \\ \text{usually 1 eV.}$$

For the purpose of the present analysis, the important consequence of this formulation, is that the average compound nucleus width varies approximately as the square root of the neutron energy, permitting us to extrapolate the low-energy data to the energy region in the present study.

7.5 Application to Present Experiment

Using the Hibdon⁽¹⁹⁾ data, average values of the compound nucleus width and level density were calculated for fluorine, aluminum and calcium. These parameters were then extrapolated to a neutron energy of 2.0 MeV using the formulae developed in the previous section. The averages of the Hibdon data, and the extrapolated average widths and spacings are shown in Table (IV). From these data, the Porter Thomas

Table IV

Average Compound Nucleus Parameters of F, Al, Ca

Element	average Energy	Average Width	No. of Res per MeV	C	Extrap. Width @ 2.0 MeV	Extrap. No. @ 2.0 MeV
F ¹⁹	200 keV	3.3 keV	17	1.2	9.0 keV	36
Al ²⁷	500	2.4	112	2.0	5.5	160
Ca ⁴⁰	500	0.25	125	0.40	0.5	220

distribution function was utilized to calculate the total number of compound nucleus states at each width interval compatible with the widths measured in the present experiment. These distributions are shown in Fig. (39) superimposed on the measured distribution of widths, shown previously in Fig. (38).

It is evident from this figure that the resonances observed in the present experiment probably originate from some mechanism other than the compound nucleus mechanism. Particularly in the heavier elements, Porter-Thomas fluctuations are not of sufficient magnitude to explain the presence of states with widths greater than 40 keV.

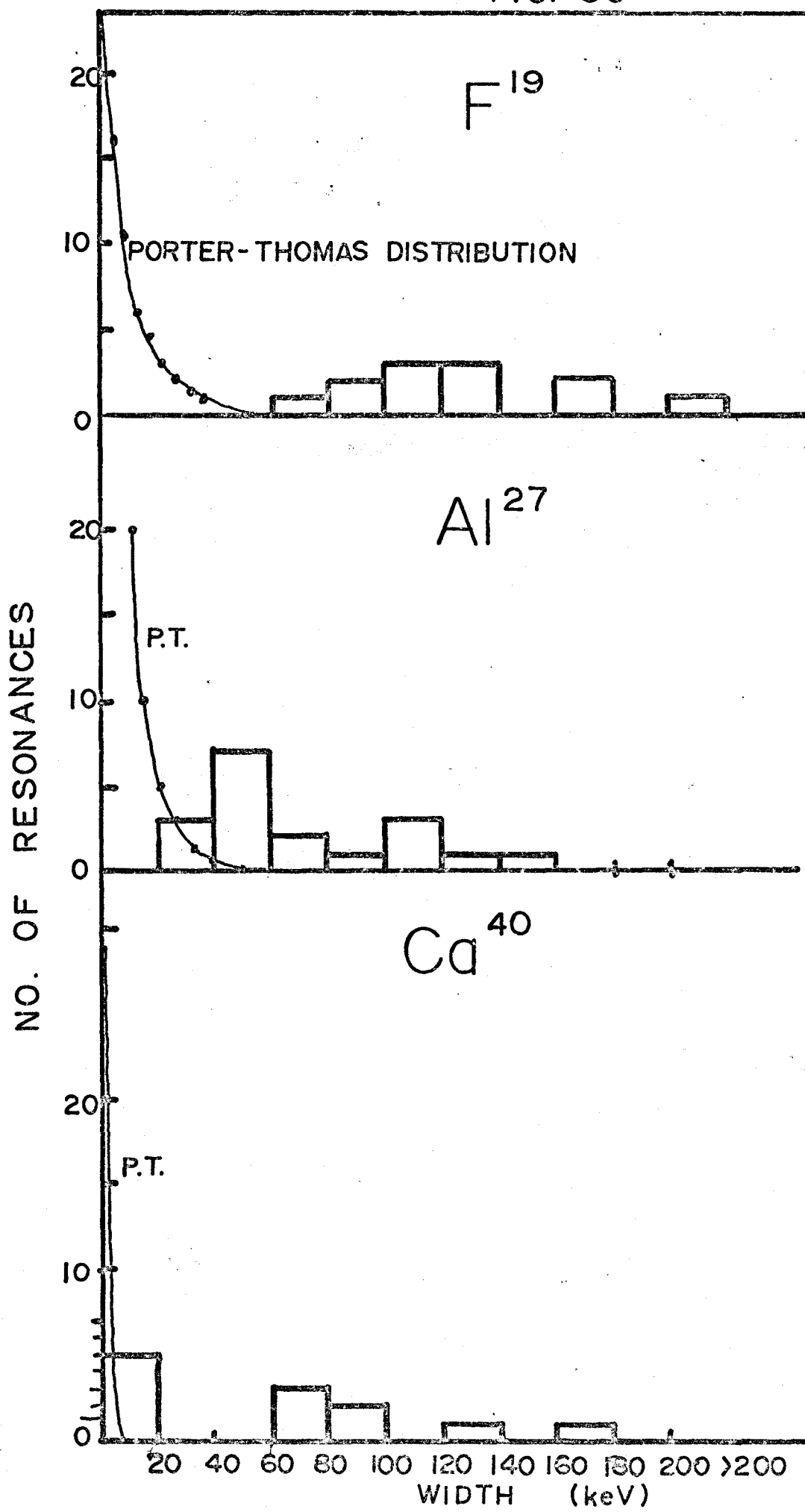
Returning to Fig. (38), it is evident that the majority of states observed in the present experiment are not compound nucleus resonances. Since the average width of compound nucleus resonances decreases regularly with mass⁽³⁵⁾, approximately as $A^{-2/3}$ ⁽³⁾, this mechanism is inadequate to explain all but the narrowest resonances for elements with mass greater than 27. Furthermore, in F^{19} , a large number of resonances exist with average width of ~ 150 keV, and these are not accounted for by the compound nucleus picture.

On the assumption that these resonances are evidence of the doorway state mechanism, it is apparent that the average width of these resonances varies considerably with target

Fig.39. DISTRIBUTION OF COMPOUND NUCLEUS AND INTERMEDIATE WIDTHS IN F,AL,ANDCa.

COMPOUND NUCLEUS WIDTH DISTRIBUTIONS ARE CALCULATED FROM HIBDEN DATA ASSUMING A PORTER-THOMAS DISTRIBUTION,AND CORRECTING MEANS FOR DEPENDENCE ON INCIDENT NEUTRON ENERGY.

FIG. 39



nucleus from a minimum of ~ 50 keV in S^{32} to a maximum of ~ 130 keV in F^{19} . Furthermore individual doorway resonances may exist with widths considerably narrower than these averages.

These results have implications in terms of the commonly accepted "average" width of ~ 100 keV. The origin of this "axiom of width" and its impact on the relationship between the characteristics of doorway states and nuclear structure will be discussed further in Chapter IX.

7.6 Energy Dependence of Doorway State Widths

From the distribution of doorway-state widths shown in Fig. (39) for fluorine, aluminum and calcium, it is evident that considerable dispersion exists in these widths. However some indication of the energy dependence of these widths may be obtained by plotting the widths of individual resonances as a function of energy. These plots are shown for fluorine, aluminum, and calcium in Figs. (40) to (42) respectively. Considering only those points corresponding to widths outside the compound nucleus range, no clear energy dependence is evident in aluminum. However in both calcium and fluorine, a clear trend to higher widths at increased neutron energies exists. An empirical \sqrt{E} function is shown on these graphs, the multiplying constant being fitted visually to the data.

Fig. 40-42. WIDTHS OF INDIVIDUAL RESONANCES FUNCTION OF ENERGY
IN F, AL, AND CA.

THE SEPARATION BETWEEN COMPOUND NUCLEUS AND INTERMEDIATE
STRUCTURE WIDTHS IS EVIDENT FROM THESE GRAPHS. A POSTULATED
 $E^{1/2}$ DEPENDENCE IS SHOWN FOR INTERMEDIATE STRUCTURE IN F & CA.

FIG. 40

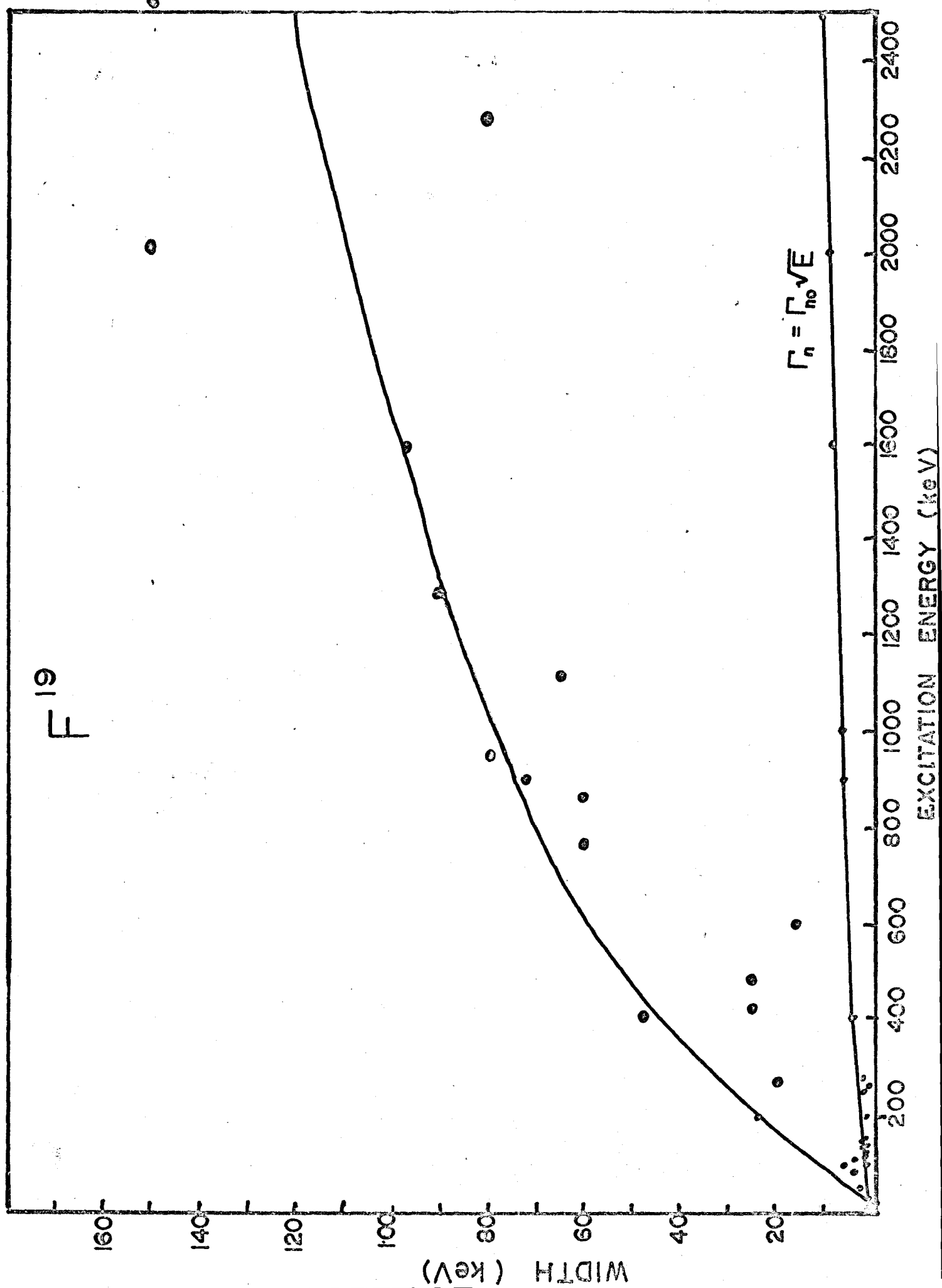


FIG. 41

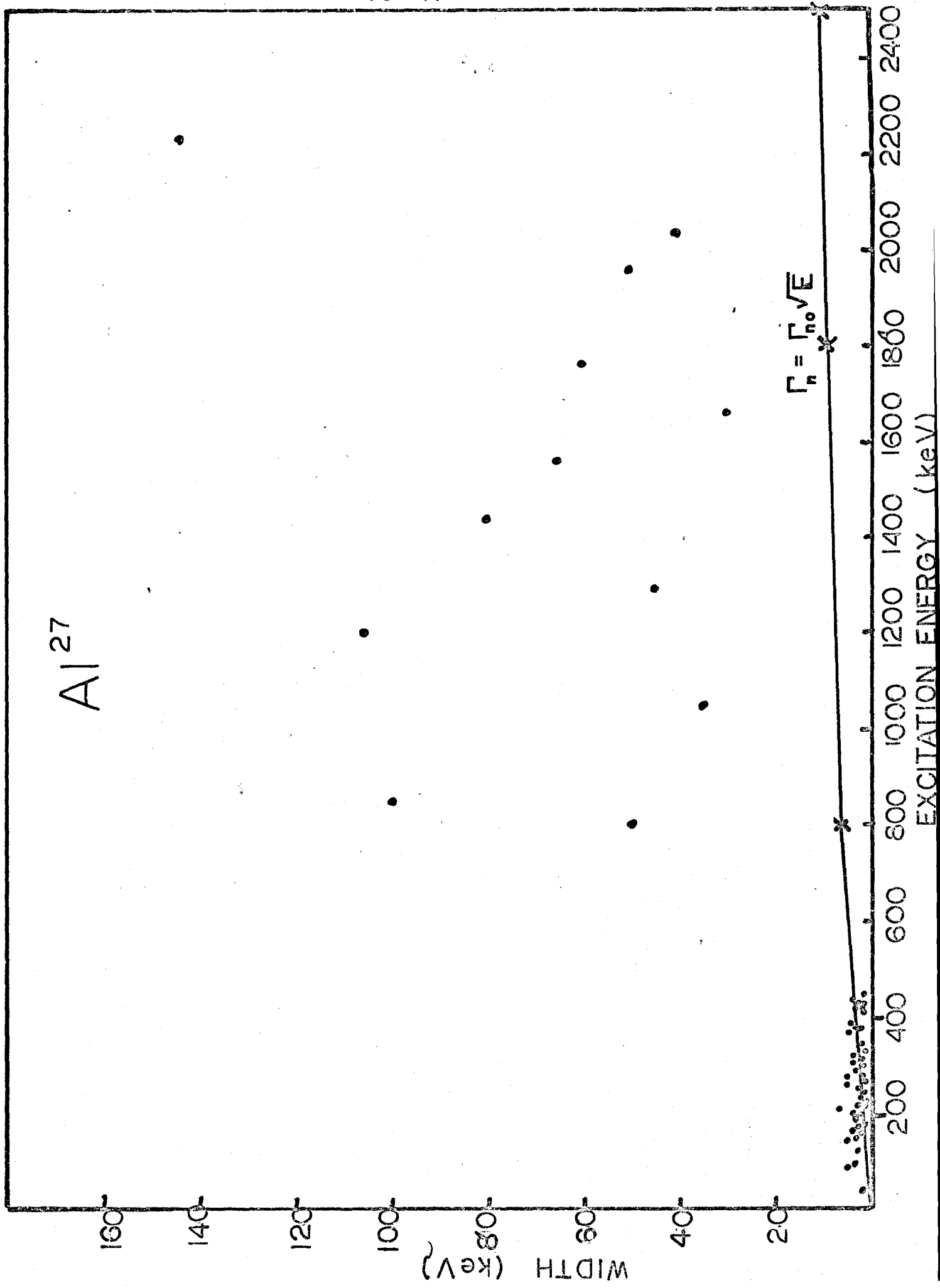
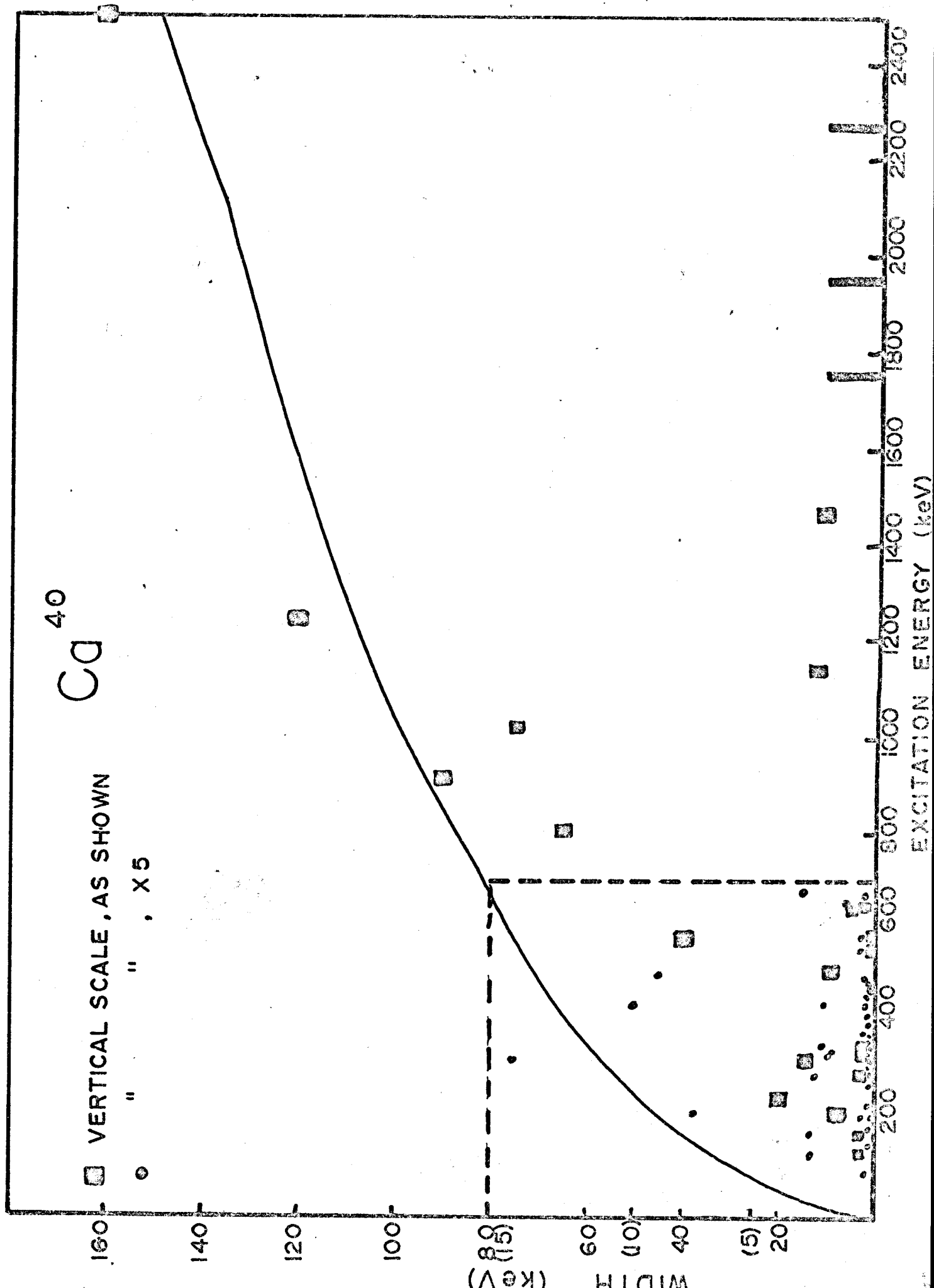


FIG. 42



CHAPTER VIII

SPECTRAL ANALYSIS OF CROSS SECTIONS

8.1 Signal Analysis Techniques

The analysis of experimental cross-sections by signal-averaging techniques is not a new approach. Seth⁽³⁶⁾ used the method of autocorrelation analysis to determine average widths in the cross sections of seventeen medium weight nuclei, and Ericson⁽⁵⁶⁾ showed that the value of the auto-correlation function in a region of overlapping compound nucleus resonances is a measure of the average compound-nucleus width. These analyses relate the form of the auto-correlation determined experimentally to the theoretical form based on a single resonance of Lorentzian shape above a smooth background.

However these analyses have been confined to an examination of the auto-correlation function over a range comparable with the average width of resonances. It will be shown in the present analysis that considerable information may be deduced from an extension of the auto-correlation function to greater displacements, and furthermore, the logical progression to a power-spectral analysis of the auto-correlation function, in combination with detailed examination of the auto correlation function yields an estimate of the

neutron-strength function. Furthermore, parameters may be extracted which yield not only the average width and spacing, but also permit some inference of the distribution of widths and spacings about these means.

8.2 The Auto-Correlation Function

For a real function $f(x)$ defined between limits of $-\infty$ and $+\infty$ the auto-correlation function is defined as ⁽⁶¹⁾:

$$R(\epsilon) = \int_{-\infty}^{\infty} f(x)f(x+\epsilon)dx. \quad (8.1)$$

In application to neutron cross-sections, this is usually written in a modified form. For a cross section $\sigma(E)$, defined over the energy interval E_1, E_2 the auto-correlation function is written as

$$R(\epsilon) = \frac{1}{(E_2 - E_1)} \left[\int_{E_1}^{E_2} \sigma(E)\sigma(E+\epsilon)dE - \left(\int_{E_1}^{E_2} \sigma(E)dE \right)^2 \right] \quad (8.2)$$

$$= \langle \sigma(E)\sigma(E+\epsilon) \rangle - \langle \sigma \rangle^2. \quad (8.3)$$

Although this form differs from the previous in two respects; normalization over the energy interval, and a baseline shift to a mean value of zero, the characteristics of the two functions are identical. Specifically, all dependence on ϵ is contained in the first term of eq. 8.3, and this term is identical, aside from normalizations, in the two formulations.

Qualitatively, it can be seen from the functional form

of $R(\epsilon)$ that this provides an average measure of the correlation between values of the cross section separated by an energy ϵ . Considering a simple example, of δ -functions at a fixed spacing of Δ , the ac function would be a δ function at $\epsilon = \Delta, 2\Delta, 3\Delta$, etc and zero elsewhere. The auto-correlation function of a pure sine or cosine wave of frequency ν may be easily interpreted. Since everywhere points at $\epsilon = \frac{\pi}{\nu}, \frac{3\pi}{\nu}$, etc. are anticorrelated with points at $\epsilon = 0$, then clearly the auto-correlation function at these points will be a minimum. Similarly the auto-correlation function will maximize at $\epsilon = \frac{2\pi}{\nu}, \frac{4\pi}{\nu}$, etc.

Thus the maxima of this function provides a measure of the average spacing of maxima in the original spectrum. Furthermore, since $R(0)$ is a maximum, equal to the mean-square fluctuation of the cross-section, the width of the maximum about zero provides some measure of the average width of the fluctuation in cross-section.

These properties will be discussed quantitatively in section 8.4, but some understanding of the definition and properties of this function are pertinent to the following section.

8.3 The Power Spectrum Function

The "power spectrum" of a given function $\sigma(E)$ is related to the Fourier transform of the function. Thus:

$$\Sigma(\omega) = \int_{-\infty}^{\infty} \sigma(E) e^{-i\omega E} dE \quad (8.4)$$

where ω = frequency

defines the Fourier transform of the cross-section. The power spectrum of $\sigma(E)$ is the squared modulus of the Fourier transform. Thus

$$P(\omega) = |\Sigma(\omega)|^2 \quad (8.5)$$

It may be shown that the power spectrum of a function is directly obtainable from the auto-correlation function, and is in fact, the Fourier transform of the auto-correlation function. Since the auto-correlation function, from its definition, is an even function, then the power spectrum is similarly an even function and is usually defined only for positive frequency.

The power spectrum is amenable to physical interpretation, as implied by its name. The function represents the amount of "energy" present in the original spectrum at each frequency. Therefore, any arbitrary periodic function, of period τ , will show a peak in the power spectrum at a frequency $\nu = 1/\tau$.

Power spectral analysis is useful in the analysis of total cross-sections, as a dominant spacing of D would show as multiple peaks at D , $2D$, etc. in the auto-correlation function, but would be present in the power spectrum as a single peak at $\nu = 1/D$.

8.4 Detailed Properties of Auto-Correlation and Power Spectrum.

Certain qualitative features of the auto-correlation function and power spectrum have been described in the previous section. However some properties have not been delineated, and require further investigation to be of use in the present analysis.

For example, it is unclear how the width of the auto-correlation function about zero is related to the average width in the original spectrum in the case of multiple peaks. Furthermore, this width should intuitively be sensitive to the distribution of widths about the mean, and may be sensitive to the average spacing of peaks. Similarly the power spectrum should in some manner show evidence of the distribution of spacings about the mean.

The auto-correlation function may be evaluated analytically for the simple case of a picket-fence distribution of resonances of Lorentzian form; that is to say, peaks of fixed amplitude and width separated by a fixed distance. This model was used to obtain insight into some of the questions posed above.

Auto-correlation Function for Single Resonance and Multiple Resonances

It may be shown by several methods, eg. Cauchy integration in the complex plane, inverse Fourier transformation, that for a single Lorentzian at $x = 0$,

$$f(x) = \frac{1}{1+x^2} \quad \text{experimentally } x = \frac{2E}{\Gamma} \quad (8.6)$$

The auto-correlation function is just

$$R(x) = \frac{2\pi}{4+x^2} \quad (8.7)$$

Thus, for a single resonance, the auto-correlation function is a Lorentzian with width 2Γ .

Now for a picket fence model over the interval $2E=(2N+1)D$

$$f(x) = \sum_{n=-N}^N \frac{1}{1+(x-\frac{2nD}{\Gamma})^2} \quad (8.8)$$

and

$$R(\epsilon) = \frac{1}{(2N+1)D} \int_{-\infty}^{\infty} \sum_{n=-N}^N \sum_{m=-N}^N \frac{1}{1+(x-\frac{2nD}{\Gamma})^2} \frac{1}{1+(x-\frac{2mD}{\Gamma}+\epsilon)^2} dx \quad (8.9)$$

Setting $y = x - nD$

$$R(\epsilon) = \frac{1}{(2N+1)D} \int_{-\infty}^{\infty} \sum_{n=-N}^{+N} \sum_{m=-N}^{+N} \frac{1}{1+y^2} \frac{1}{1+(y-2(m-n)\frac{D}{\Gamma}+\epsilon)^2} dy \quad (8.10)$$

$$\begin{aligned} &= \frac{2N+1}{(2N+1)D} \int \frac{1}{1+y^2} \frac{1}{1+(y+\epsilon)^2} dy + \frac{2N}{(2N+1)D} \int \frac{1}{1+y^2} \frac{1}{1+(y-\frac{2D}{\Gamma}+\epsilon)^2} dy + \\ &+ \frac{2N}{(2N+1)D} \int \frac{1}{1+y^2} \frac{1}{1+(y+\frac{2D}{\Gamma}+\epsilon)^2} dy + \frac{2N-1}{(2N+1)D} \int \frac{1}{1+y^2} \frac{1}{1+(y-\frac{4D}{\Gamma}+\epsilon)^2} dy \end{aligned} \quad (8.11)$$

Then for $N \rightarrow \infty$, using equation 8.7

$$R(\epsilon) = \frac{2\pi}{4+4x^2} + \frac{2\pi}{4+4(x-\frac{D}{\Gamma})^2} + \frac{2\pi}{4+4(x+\frac{D}{\Gamma})^2} + \frac{2\pi}{4+4(x-\frac{2D}{\Gamma})^2} \text{ etc.} \quad (8.12)$$

where $x = \frac{\epsilon}{\Gamma}$

$$= \frac{\pi}{2} \frac{1}{1 + (\frac{\epsilon}{\Gamma})^2} + \frac{\pi}{2} \frac{1}{1 + (\frac{\epsilon}{\Gamma} - \frac{D}{\Gamma})^2} + \frac{\pi}{2} \frac{1}{1 + (\frac{\epsilon}{\Gamma} + \frac{D}{\Gamma})^2} + \frac{\pi}{2} \frac{1}{1 + (\frac{\epsilon}{\Gamma} - \frac{2D}{\Gamma})^2} + \dots \quad (8.13)$$

These results are shown in Fig. (43). It will be noted that if the width of the auto-correlation function is defined as the value of ϵ at half height, height being measured from maximum to first minimum of the auto-correlation function, the width decreases with decreasing spacing. Restating this result, the width of the auto-correlation function is related to the average width, and the average spacing of the resonances. This result will prove crucial to the analysis of experimental cross-sections.

To extend the analysis to the power spectral analysis of the picket fence model, a theoretical distribution was generated by computer, and analysed using an available subroutine package for calculation of auto-correlation and power spectrum functions. These calculations were performed for values of Γ/D of 0.1, 0.2 \rightarrow 1.0. The power spectra shows a single peak at a frequency corresponding to the average spacing as expected from the definition.

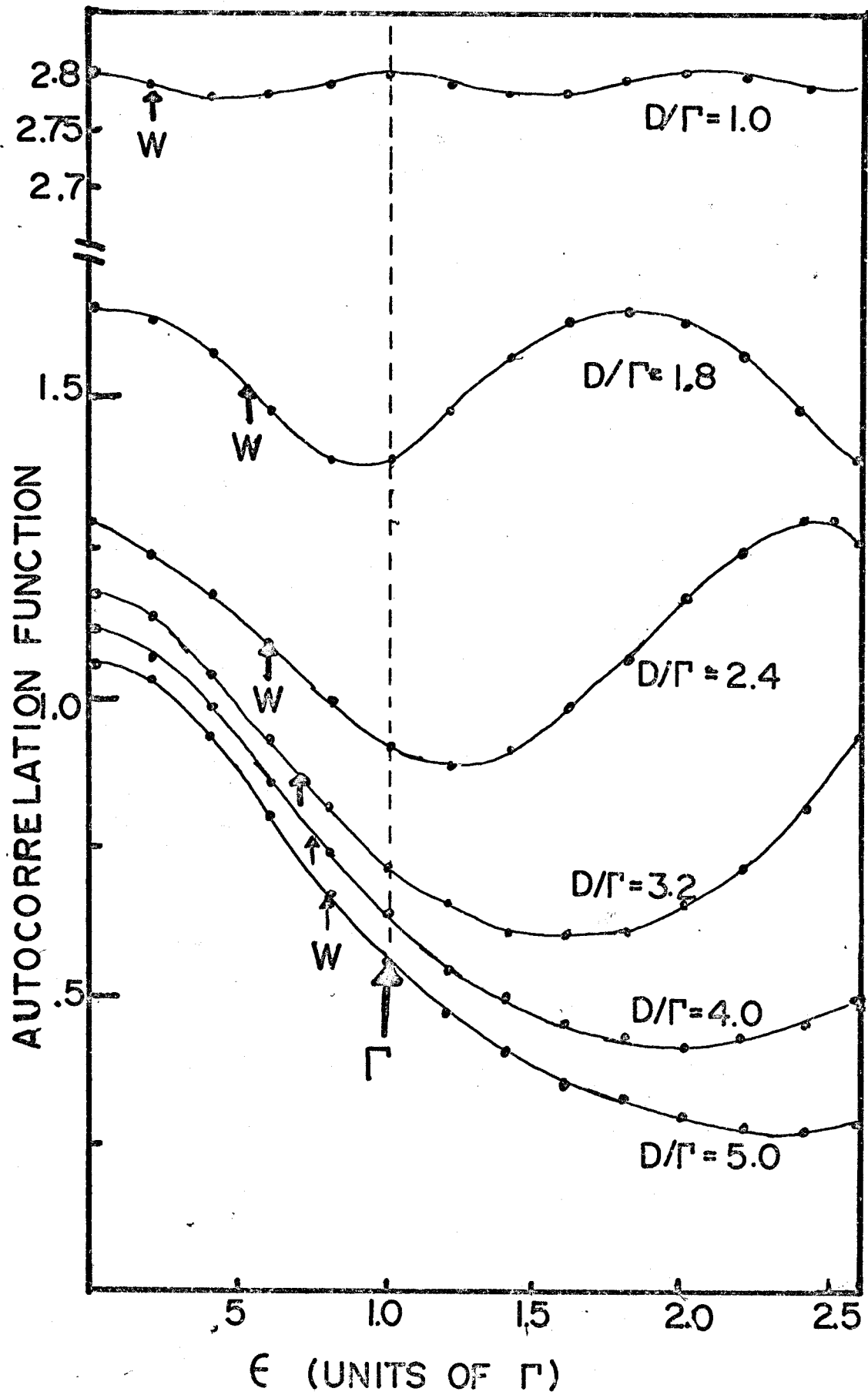
To summarize the characteristics of these functions, based on analysis of a picket fence model:

- (1) In the limit of average spacing $\rightarrow \infty$, the width of the a.c. function is twice the width of the individual resonance.
- (2) The auto-correlation function showed secondary maxima corresponding to a displacement of D , $2D$, $3D$, etc.

FIG.43. AUTOCORRELATION FUNCTION OF PICKET FENCE CROSS-SECTION.

THE FUNCTION IS ILLUSTRATED FOR DISPLACEMENTS TO
2.5 Γ , AND VARIOUS VALUES OF D/Γ .

FIG. 43



- (3) The width of the auto-correlation function decreases with decreasing average spacing and is therefore a function of D and Γ .
- (4) The average spacing is reflected in a peak in the power spectrum at a frequency corresponding to the inverse of this spacing.

8.5 Experimental Results

To calculate the auto-correlation and power spectrum of the experimental cross-sections, these were quantized at 20 keV increments by visual readout of the mean curve through the data points.

In order to reduce the effects of experimental resolution these data were obtained over a limited region from 800 to 2500 keV. In this region, the experimental resolution, while non-negligible, is still relatively small compared with the average widths of observed resonances.

Data points obtained by visual methods were then key punched as input to the program package for calculation of auto-correlation and power spectrum.

The experimental auto-correlations are shown in Fig. 44-47, for a lag $\epsilon \leq 800$ keV. As we have shown for the picket fence model, the average spacing is observed in the auto-correlation function by multiple peaks at D , $2D$, $3D$, etc. Such a functional form is clearly evident for fluorine, aluminum,

FIG.44-4Z. EXPERIMENTAL AUTOCORRELATION FUNCTIONS A=19-40.

SPACINGS CORRESPONDING TO PEAKS IN THE POWER SPECTRA
ARE INDICATED BY NUMBERS, WITH MULTIPLE AUTOCORRELATION PEAKS
IDENTIFIED BY PRIMES.

FIG. 44

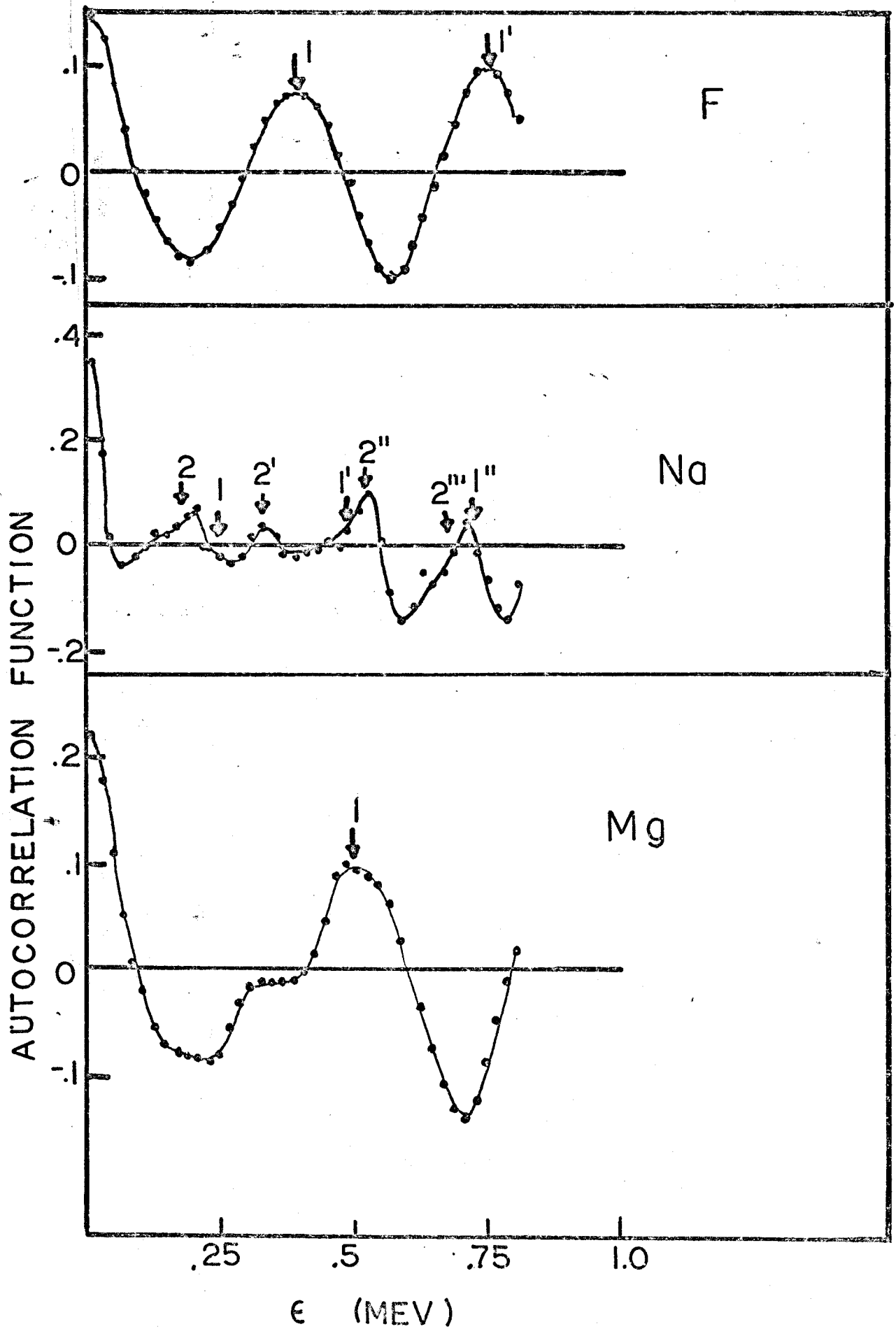


FIG. 45

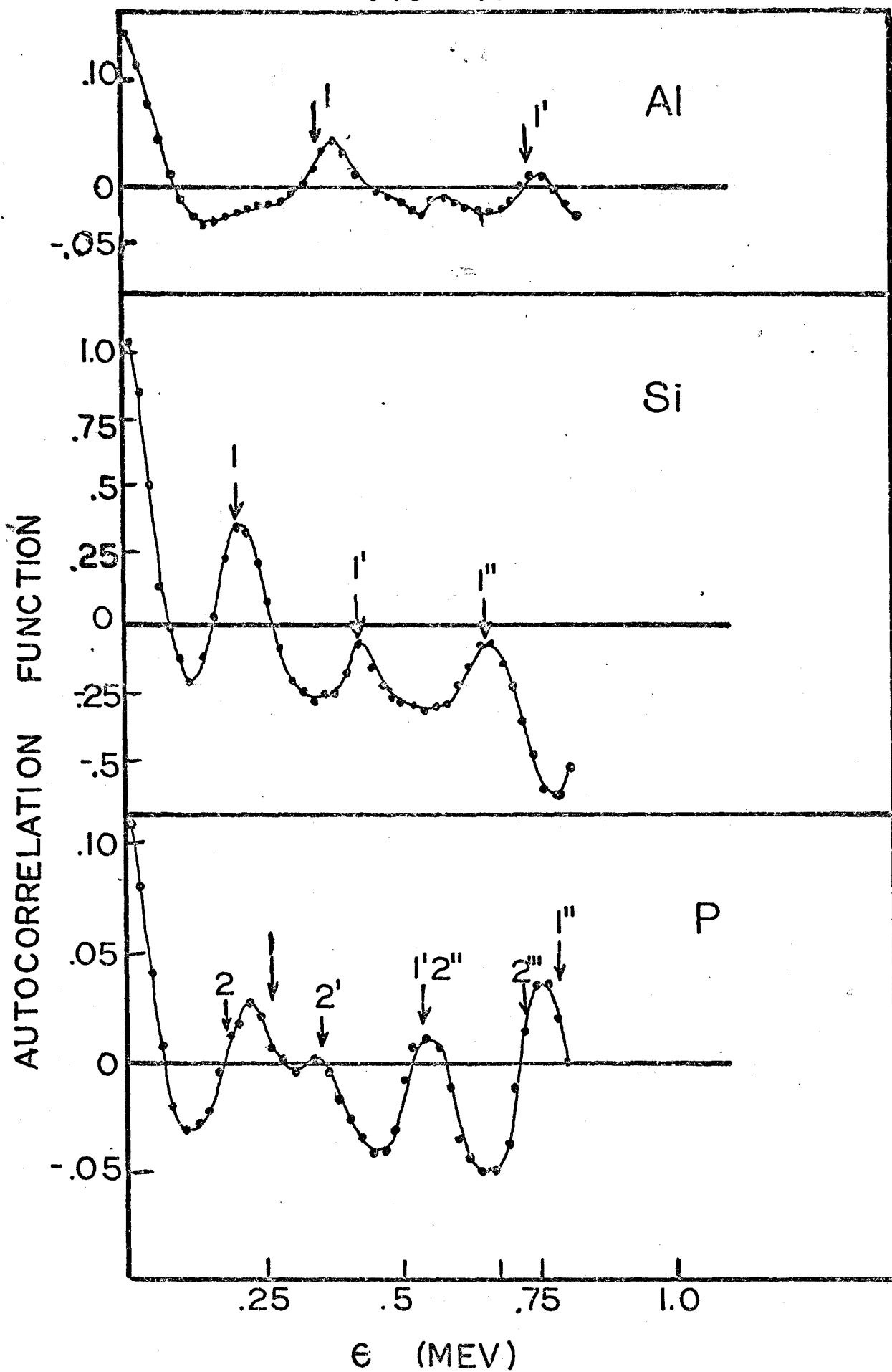


FIG. 46

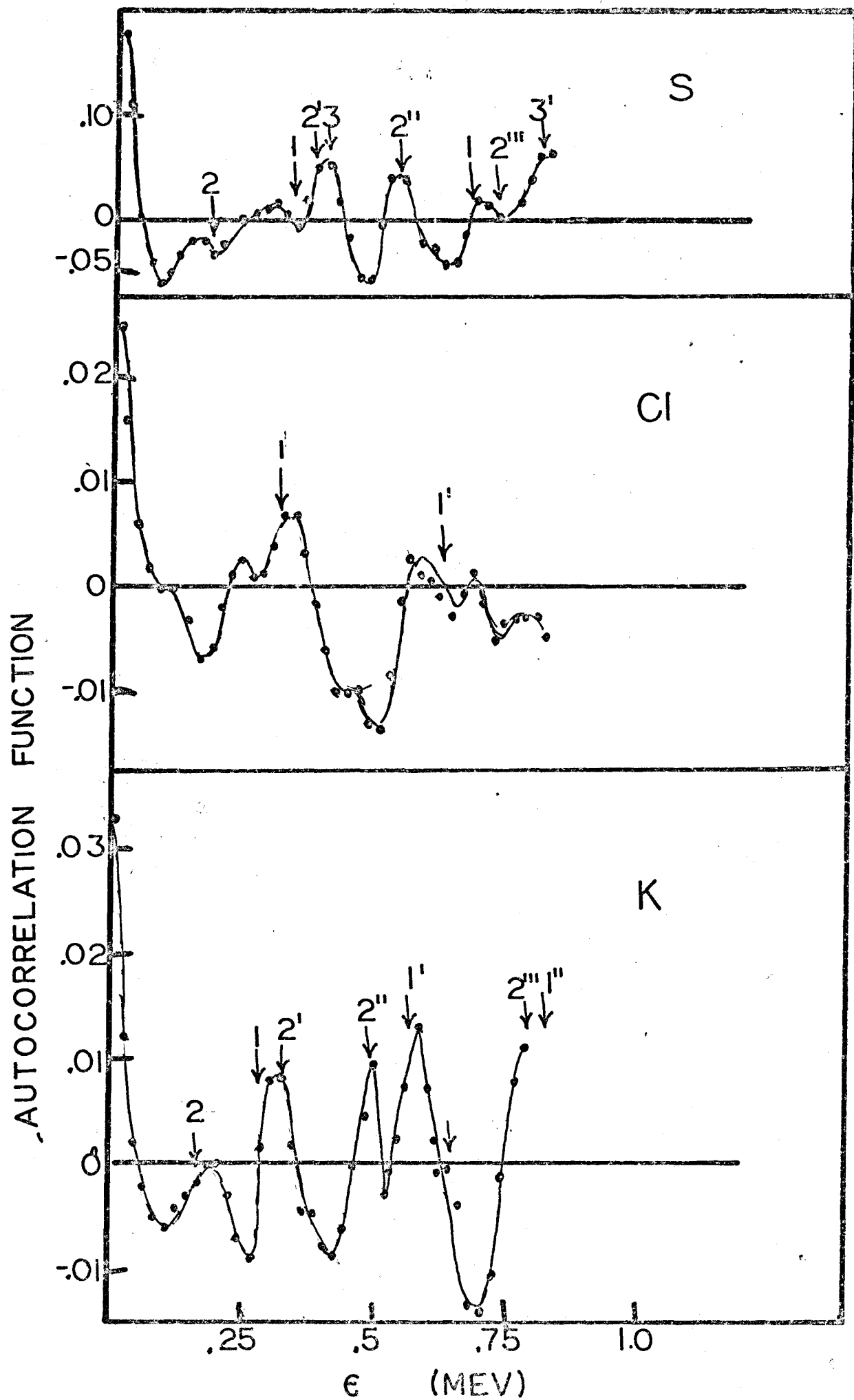
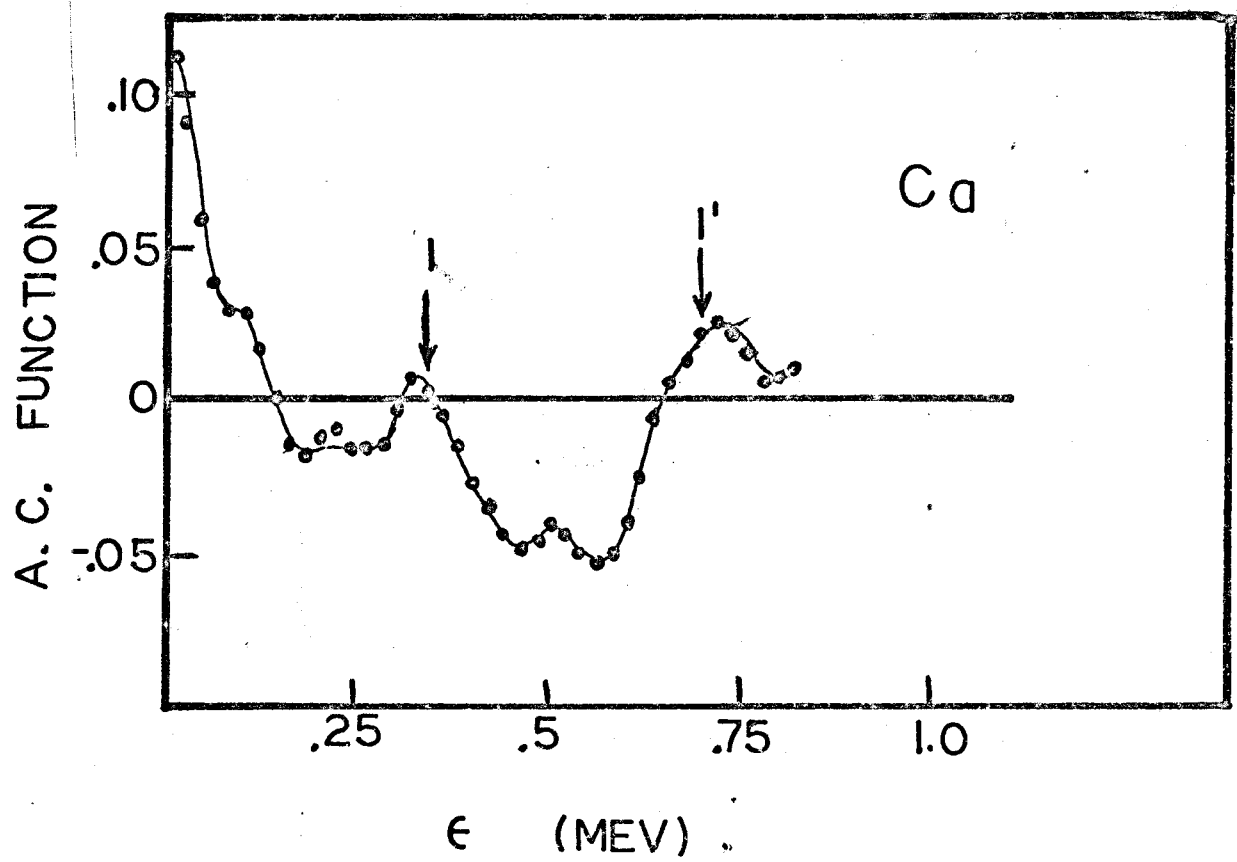


FIG. 47



silicon and calcium. A multiple peak structure with somewhat less certainty is shown for phosphorus and chlorine. In these two cases the lack of clear resonance behaviour may be due to poor statistics in these nuclides, resulting from the relatively low amplitude of the resonance structure. Magnesium presents a single strong resonance at 500 keV lag. The remaining three nuclides are somewhat anomalous in that multiple peaks are present in potassium and sulphur, but the constraint of resonances at multiples of the average spacing does not appear to be satisfied. Sodium, finally does not show any strong characteristic structure.

The presence of prominent maxima in the auto-correlation function yields at least some qualitative insight into the distribution of spacings. For in order for maxima to exist, spacings between resonances must be distributed about the average spacing with a dispersion characterized by the width of the maxima. Furthermore the presence of multiple maxima substantiates this form of the distribution, as a single maximum at a spacing ϵ could be obtained from two strong peaks in the spectrum at this spacing, however, two such peaks would not contribute to a second maximum at 2ϵ .

From this discussion it follows that the absence of correlated maxima does not indicate a failure of the analytic technique, but may result from a broad distribution of spacings about the mean.

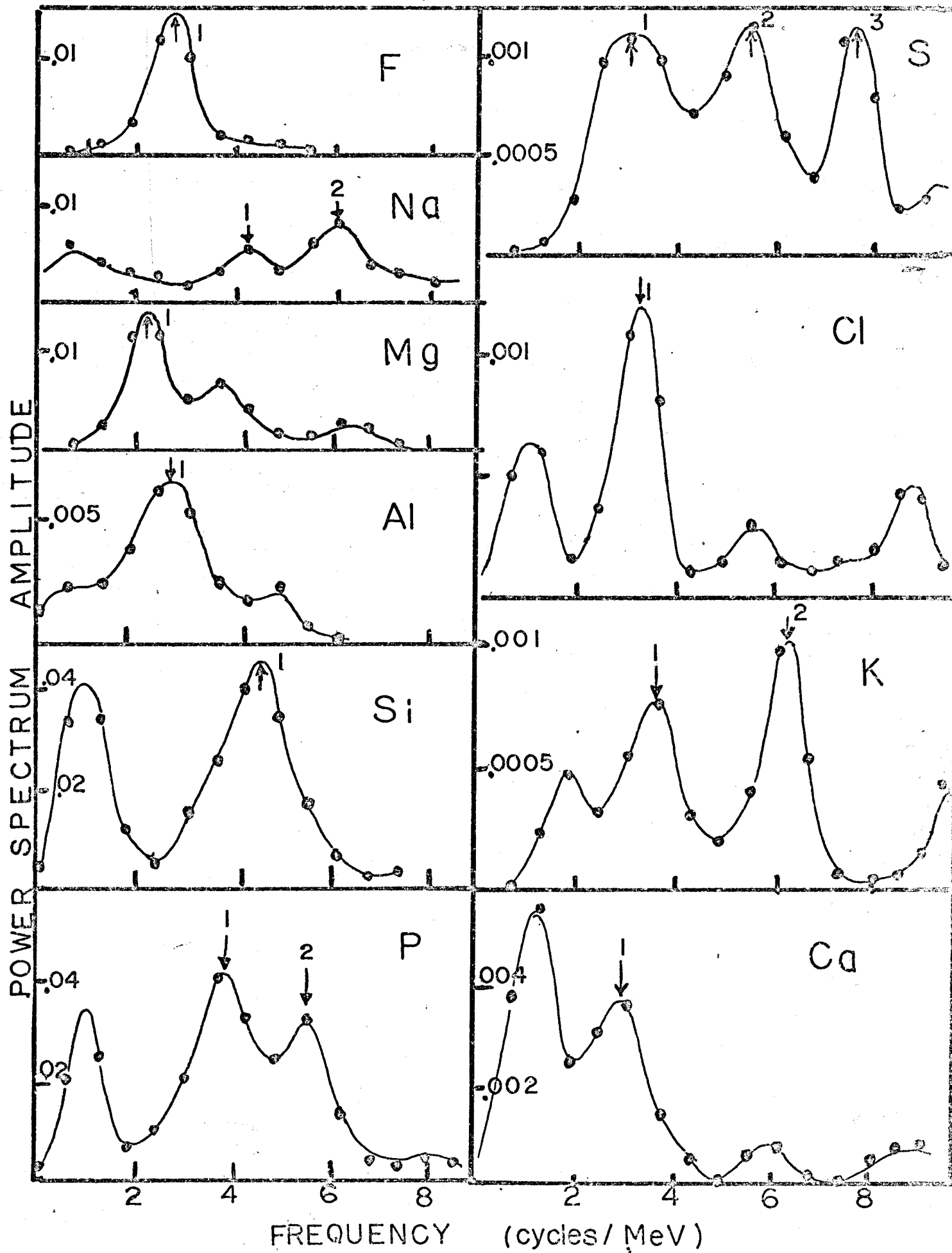
For additional confirmation of the average spacing obtained from this analysis, we turn to the power spectrum of each element. These are illustrated in Fig. (48). These power spectra are for a frequency of 0-10 cycles / MeV, or for a range of spacing from infinity to 100 keV. It was found that very little power was present in any nucleus for frequencies greater than 10/ MeV, indicating a spacing of resonances observed in these experiments of greater than 100 keV. Where a peak is present in the power spectrum at 1 cyc/MeV, as in the case of Si, P, K, Ca, this corresponds to a fluctuation with a period of 1 MeV. Since the cross-section is measured over a range of 1.5 MeV, this power is present in the trend of the cross-section, or in a crude sense, represents the spacing of single particle resonances. Discounting this low frequency peak, then, six elements, F, Mg, Al, Si, Cl and Ca, display a single strong peak in the power spectrum. Two peaks are present for sulphur and potassium. The spacings corresponding to these peaks are shown on the auto-correlation spectra, numerically coded to the power-spectral peaks.

It may be concluded, therefore, that for six of the nuclides the auto-correlation and power spectral analysis provides an unambiguous measure of the average spacing of resonances in the cross section. Ambiguities remain in the remaining four nuclides. And, as yet, no information about average widths has been obtained from the analysis. In the

FIG.48. EXPERIMENTAL POWER SPECTRA A=19-40.

THE NUMBERED PEAKS CORRESPOND TO NUMBERS SHOWN ON
THE AUTOCORRELATION FUNCTIONS FIG.44-47.

FIG. 48



next section, a second approach to the determination of average spacings will be utilized to resolve ambiguities, and the average width will enter in the analysis of the auto-correlation function.

8.6 Correlation Between Widths and Spacings in Auto-Correlation Function

As was already noted, in the picket fence model a relation exists between the width about zero of the auto-correlation function and the average width, and average spacing of the resonances. One may expect therefore, that when the spacings and widths are distributed about the mean a similar relationship may exist. To investigate in more detail the functional form of this relationship the ratio of the auto-correlation width to the resonance width was plotted as a function of the spacing/width ratio for the picket-fence model. Difficulties exist in using this relationship for experimental spectra, as the average width cannot be obtained directly from the auto-correlation function. However the distributions of widths calculated in Chapter VII provide a good estimate of the mean resonance width.

Using this value of mean width, the same parameters were plotted for the experimental spectra. Where ambiguities existed in the auto-correlation and power spectra estimates of the average spacing, this ratio D/T was plotted for all possible D 's. These results, for the picket fence and experimental spectra are tabulated in Table V and Table VI and

Table V

Average Resonance Parameters of Picket Fence Distribution

Γ	D	W	W/ Γ	D/ Γ
10.0	50.	10.	1.0	5.0
10.0	25.	8.	0.8	2.5
10.0	12.5	5.5	0.55	1.25
10.0	10.	5.0	0.50	1.0
10.0	8.33	4.0	0.40	0.83

Table VI

Average Resonance Parameters of Experimental Distributions

Element	$\langle \Gamma \rangle$ keV	W	W/ $\langle \Gamma \rangle$	D ₁	D ₁ / $\langle \Gamma \rangle$	D ₂	D ₂ / $\langle \Gamma \rangle$	D ₃	D ₃ / $\langle \Gamma \rangle$
F	135	67	.50	370	3.00				
Na	66	23	.35	232	3.50	167	2.54		
Mg	85	62	.73	450	5.25				
Al	68	55	.81	375	5.5				
Si	100	40	.40	220	2.20				
P	51	40	.80	270	5.3	180	3.6		
S	50	30	.60	330	6.6	180	3.6	130	2.6
Cl	54	37	.69	310	5.8				
K	59	23	.39	280	4.7	159	2.7		
Ca	96	50	.52	350	3.65				

plotted in Fig. 49.

It is clear from the positions of the unambiguous points that some relationship exists between these parameters. The absolute value of D/Γ for the fitted curve is smaller in magnitude for the experimental spectra than for the picket fence model, but a similar functional relationship exists for both sets of data. Where the ambiguous points are plotted, it is clear that one value lies nearer to the fitted line than the remaining values. Furthermore if these values, which lie closer to the fitted curve, are compared with the corresponding peaks in the power spectra, in every instance, the selected data point corresponds to the highest observed peak in the power spectrum. This is interpreted as confirmation that this functional relationship between the width of the auto-correlation function about zero and the average spacing obtained from power spectra analysis is a real phenomenon in the experimental spectra.

This method, then permits an unambiguous definition of $\langle D \rangle / \langle \Gamma \rangle$, or inverting this parameter, of the strength function averaged over all angular momentum channels. Furthermore the functional form of this curve will be utilized in the following section to ascertain certain properties of the distributions of the individual parameters about their mean values.

FIG.49. RELATION BETWEEN AUTOCORRELATION WIDTH, AVERAGE WIDTH AND AVERAGE SPACING IN EXPERIMENT.

THE RATIO OF THE AUTOCORRELATION WIDTH TO THE MEAN RESONANCE WIDTH IS PLOTTED AS A FUNCTION OF D/Γ FOR THE PICKET FENCE AND EXPERIMENTAL SPECTRA. WHERE AMBIGUITIES EXIST IN THE MEAN SPACING FROM THE POWER SPECTRA, THESE ARE SHOWN AS OPEN OR SHADED CIRCLES.

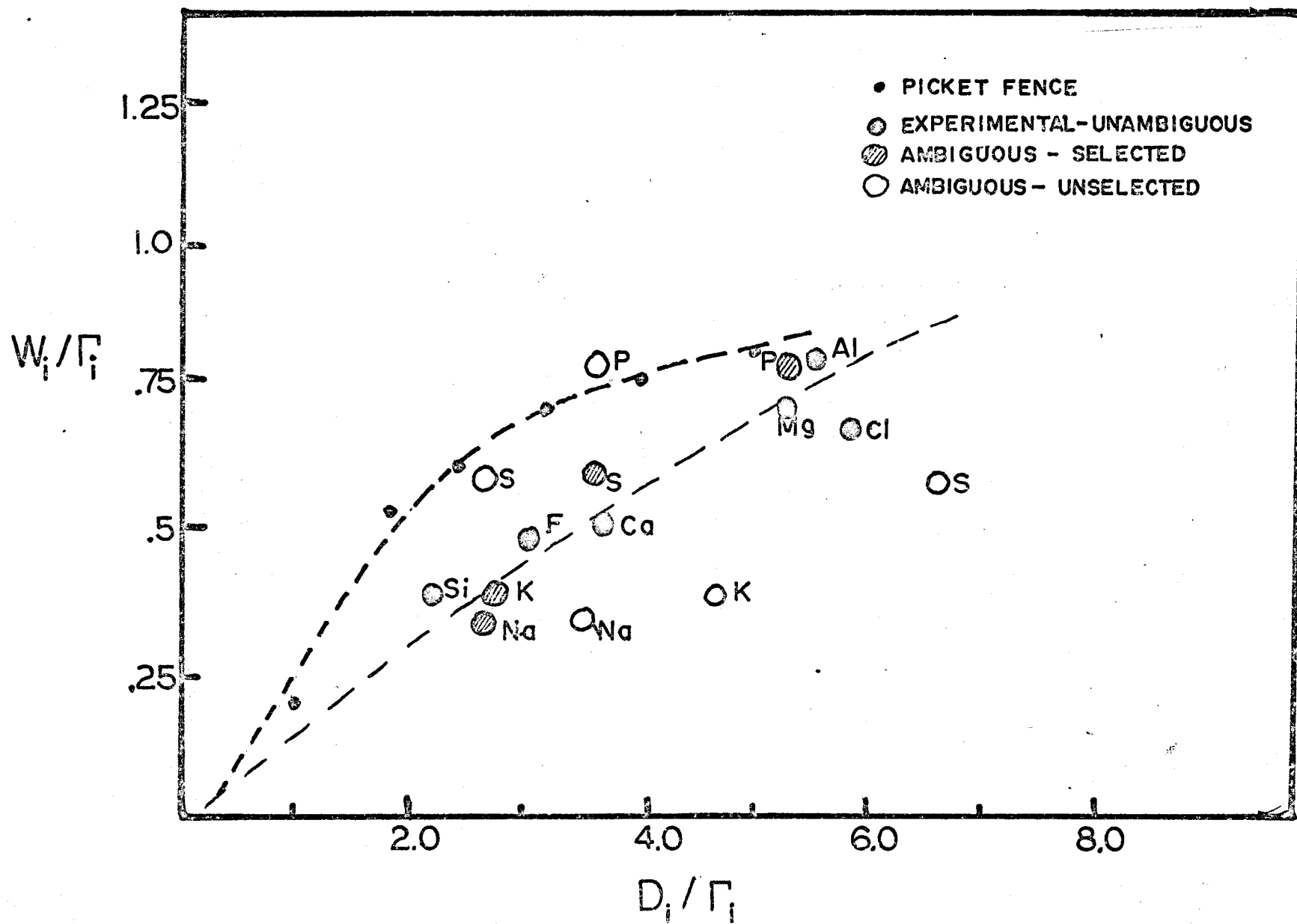


FIG. 49

8.7 Distributions of Widths and Spacings - Model Distribution

The vertical displacement between the picket fence curve in Fig. (49) and the experimental data suggests that the values of these parameters may be sensitive to the distributions of widths and spacings.

As an initial test of this hypothesis, theoretical spectra were generated with resonance amplitudes, widths and spacings distributed exponentially about their mean values. Numerical values of the means were chosen to represent as closely as possible the experimental spectra in terms of average width and spacing in channel units, average amplitude in barns, etc. For each parameter set, ten spectra were generated, corresponding to ten finite samples, and the mean values of the parameters in fig.50 obtained by averaging parameters obtained from the auto-correlation analysis of these spectra.

The exponential distributions represent distributions of extreme disorder, in contrast with the picket fence model. However, the exponential distribution of widths is a reasonable approximation to the Porter-Thomas distribution, and the exponential distribution of spacings is not unlike the spacing distribution obtained from a superposition of Wigner surmise spacings of differing angular momentum transfer. Therefore, these hypothetical distributions, although of extreme randomness, is a reasonable representation of the distributions expected on the basis of the distributions of compound nucleus resonances.

In Fig.50 the results of the exponential distributions on the labelled curve C, are shown with the data points of the picket fence model, curve A, and the experimental points. Also shown are additional curves, labelled D, and E which will be introduced later. Curve C shows a markedly different behaviour from the data of the previous distributions, tending strongly to higher values of W/Γ as D/Γ tends to zero. This result suggests that in fact these parameter curves are strongly dependent on the distributions of amplitude widths and spacings. Furthermore, it is evident that the distributions of the experimental cross-sections tend to resemble the undistributed picket fence model rather than the wide distributions of the exponential model.

The remaining curves are from theoretical spectra generated with different functional forms of the distributions.

From the distributions of individual widths, Fig. (38), which tend to be strongly peaked about the mean, resembling a Gaussian type of distribution, curve D was developed from a distribution of widths of Gaussian form, with mean equal to $\langle \Gamma \rangle$, and standard deviation of $\langle \Gamma \rangle / 2$, truncated at 0 width. Amplitudes and spacings remained exponential. It is seen that this curve is nearly flat, in contrast with curve B, and is tending more towards the experimental curve.

By imposing the additional constraint of a distribution of spacings of the Gaussian form, $\mu = \langle D \rangle$, $\sigma = \langle D \rangle / 2$, curve E

FIG.50. W/Γ FUNCTION OF D/Γ FOR EXPERIMENTAL AND THEORETICAL
DISTRIBUTIONS OF AMPLITUDES, WIDTHS, AND SPACINGS

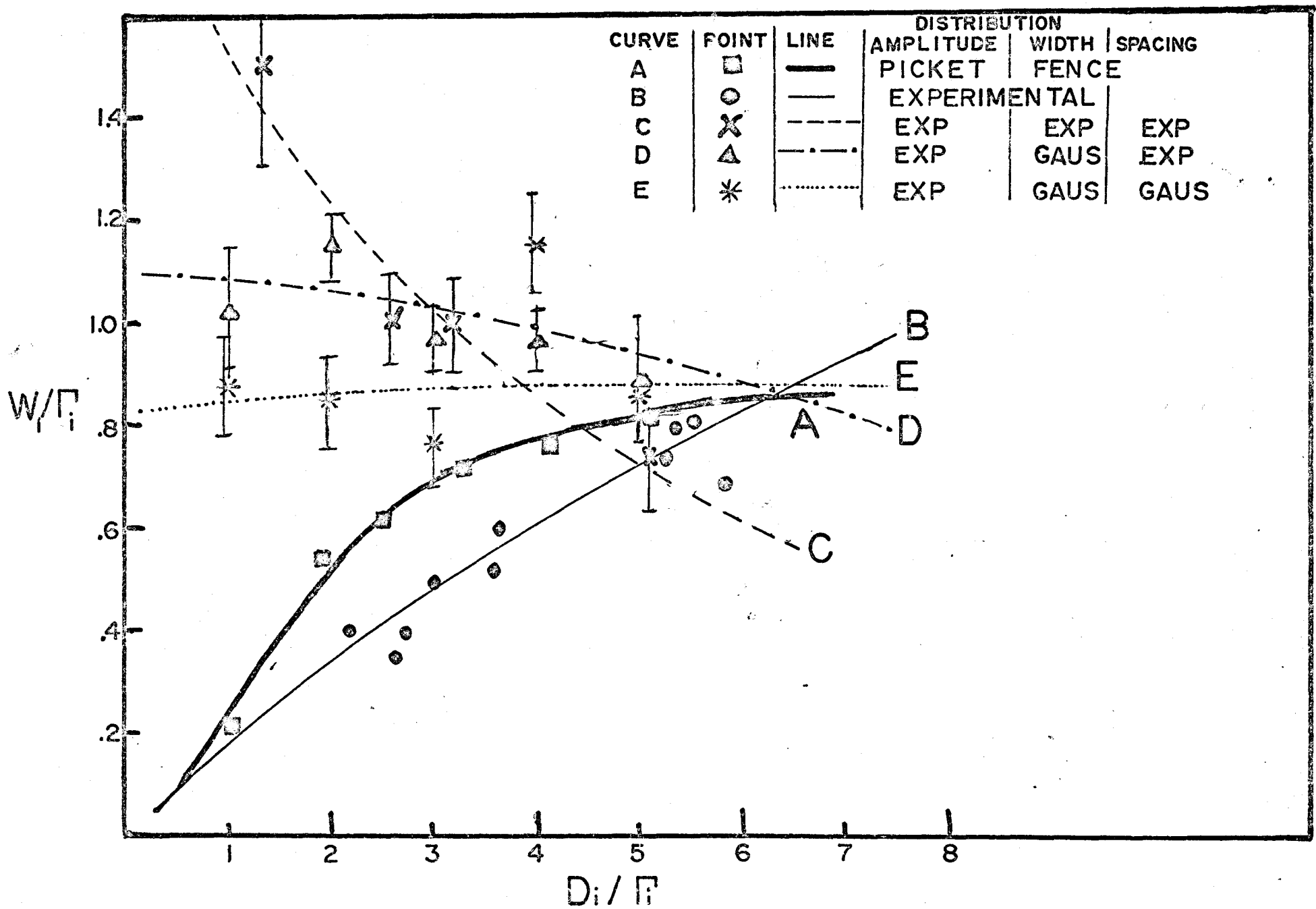


FIG. 50

resulted. This curve showed virtually no correlation between W and D, within experimental error, but moved still closer to the experimental and "picket fence" curves than the preceding curves.

From the parameter curves obtained from the theoretical distributions, it is evident that distribution of widths and spacings observed in the present experiment are constrained to relatively little variation about the means. Additional distributions could hypothetically be developed to provide a more precise fit to the experimental data, but in the absence of theoretical models of the distribution function, such a procedure may be of little benefit.

Extrapolating these strength function estimates to compare with predicted dependence on nuclear structure parameters should be attempted with caution, as it is evident that these values were derived from a relatively limited number of observed resonances. Thus, although the mean values illustrate an internal consistency of the form illustrated in the preceding section, because these estimates are based on fewer than twenty observed resonances, it is estimated that the error in these estimates may be of the order of 25% → 50%. This estimate is based on the sample size, which enters into the calculation of the average widths and, of course, the average spacing, which is highly dependent on the number of resolved resonances.

Thus, to conclude, a method has been developed to obtain average estimates of the width and spacing of resonances from auto-correlation and power spectrum analysis. Certain properties of these functions permit an inference of the distributions of these parameters about the mean values. Finally, a consistent strength function estimate may be derived from the relation between the width of the auto-correlation function, the average resonance width, and the average spacing derived from power spectral analysis.

CHAPTER IX

DISCUSSION OF RESULTS

9.1 Nuclear Parameters and Neutron Cross-Sections

As we have shown in Chapter V, the gross properties of the neutron cross section are adequately reproduced by an optical model potential, in which the nucleus is represented as a potential well containing real and imaginary components, spin-dependent components, etc. Such a model, although revealing much insight into the reaction mechanism involved, contains little information about the detailed nuclear properties of the target. For example, the ground state spin of the nucleus, the level density, the properties of the levels (collective, single particle, rotational, etc.) do not enter into the theoretical description of the reaction mechanism. It has been pointed out⁽²⁷⁾ that the presence of hard deformations, confirmed by the observation of rotational band structure in the level scheme, results in a consistent deviation of the observed cross section from the optical model predictions. This is not surprising, as the Perey-Buck potential is spherically symmetric. However in the region analysed in the present experiment, the same authors have correctly pointed out the difficulty of separating deviations due to permanent nuclear deformation from deviations due to

the formation of particle-hole states or alternately, statistical fluctuations in the component of the cross section due to compound nucleus interactions.

Although it is apparent that information may be gained from a detailed calculation of the total cross-section using a non-spherical optical potential, or alternatively a reaction theory such as the unified theory proposed by Feshbach⁽⁷⁾ such an analysis is beyond the scope of the present work. In any case, a calculated cross-section which accurately predicts the position and shape of individual resonances, in addition to the gross structure, is probably beyond capabilities of present theories of nuclear dynamics.

The fluctuations in the cross-section are, however, dependent on specific properties of the nucleus. As a simple example, we again borrow from Foster and Glasgow⁽²⁷⁾, who used the spin-dependence of the Ericson⁽⁵⁶⁾-type of fluctuation, in conjunction with the ground-state spin of target nuclei, to qualitatively explain the variation in the average amplitude of fluctuations in moving from nucleus to nucleus.

If the fluctuations are due to doorway-type resonances, the theory of Feshbach et al⁽³⁾ in conjunction with some of the results of Block and Feshbach⁽³⁷⁾ may yield theoretical predictions of the spin dependence of the fluctuation amplitude. Furthermore, as has already been pointed out, Kerman et al⁽¹²⁾ have indicated the density of the states should show a characteristic dependence of mass number, and should reflect

ground state spin, shell closure, pairing effects, etc. Therefore, in relating the total cross-section to nuclear structure it is instructive to examine the resonances observed in the cross section; their amplitudes, widths, spacings, and the associated average parameters calculated in Chapter VIII, with a view to correlating these results with theoretical predictions.

9.2 Cross-Section Fluctuations and Target Spin

In their discussion of fluctuations observed in the cross-sections of light nuclei ($A < 40$) Foster and Glasgow⁽²⁷⁾ used the correlation of the average amplitude of fluctuations with the ground state spin to explain the observed resonance structure in terms of Ericson fluctuations. However, to use this evidence as an argument against the existence of doorway states, it is necessary to evaluate the spin dependence of doorway-type resonances.

In particular, since the auto-correlation function at a displacement of $\epsilon=0$ is just the variance in the total cross-section, we will develop a theoretical expression for this variance based on a model of multiple doorway-state resonances.

Expanding on the theory given in section 1.4, it may be shown that the doorway-resonance, with inclusion of angular momentum dependence, may be written as

$$\sigma(E) = \frac{\pi}{k^2} \frac{(2J+1)}{(2i+1)(2I+1)} \frac{\Gamma_d^\dagger \Gamma_d}{(E-E_0)^2 + 1/4 \Gamma_d^2} \quad (9.1)$$

where J = total angular momentum of spectra

i = spin of incident nucleon

I = ground state spin of target nucleus

Expressing equation (9.1) in terms of energy-dependent and energy-independent variables:

$$\sigma(E) = K \frac{1}{\frac{4(E-E_0)^2}{\Gamma_d^2} + 1} \quad (9.2)$$

where

$$K = \frac{\pi}{k^2} \frac{(2J+1)}{(2i+1)(2I+1)} \frac{4\Gamma_d^\uparrow \Gamma_d^\downarrow}{\Gamma_d^2} .$$

Now from section 8.2, the auto-correlation function is given by

$$F(\epsilon) = \langle \sigma(E+\epsilon)\sigma(E) - \langle \sigma \rangle^2 \rangle \quad (9.3)$$

or from equation 9.2 and the results of section 8.4,

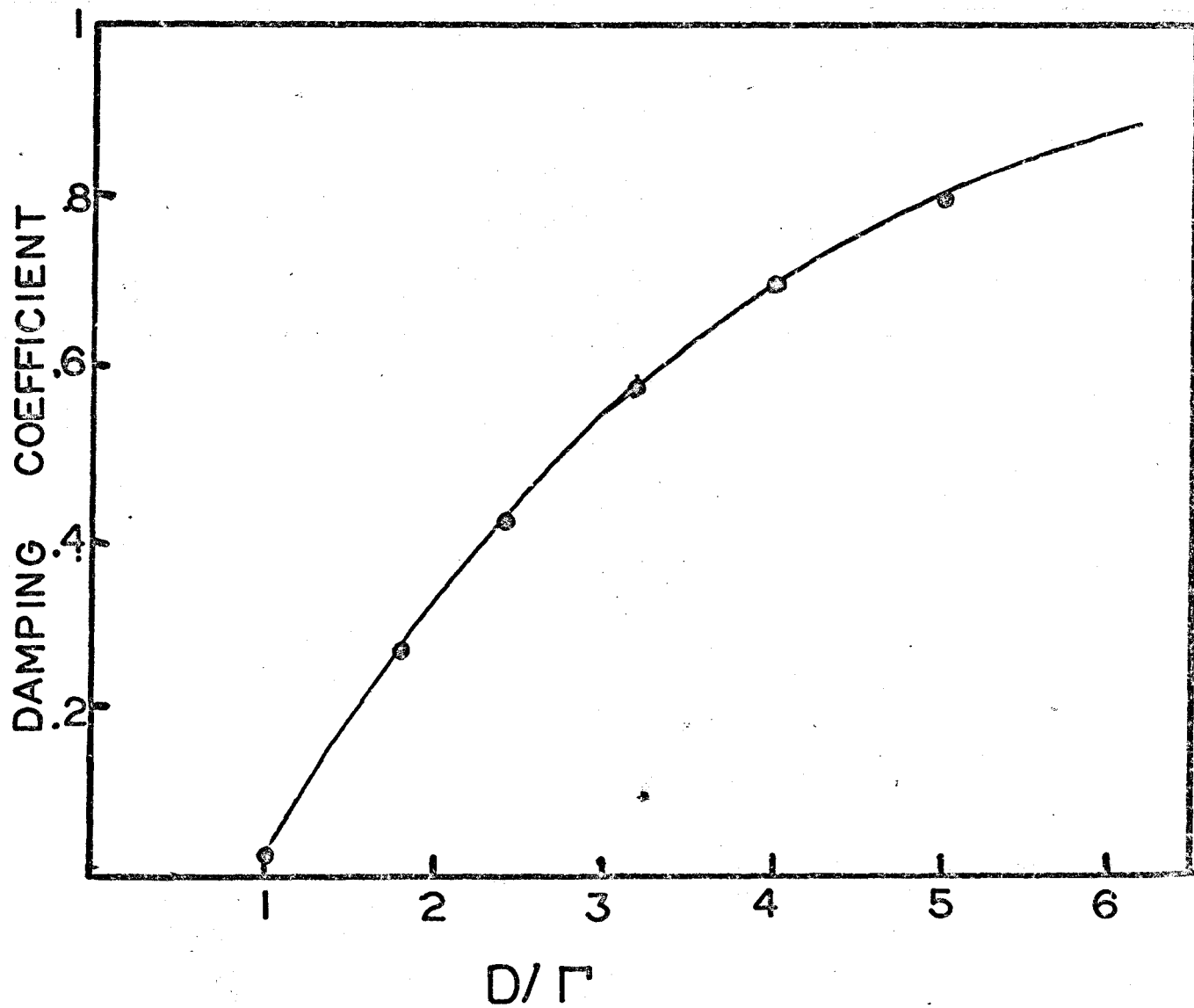
$$F(\epsilon) = K^2 \left(\frac{1}{\frac{(E_0 - \epsilon)^2}{\Gamma_d^2} + 1} \right) \quad (9.4)$$

Equation 9.4 is valid for the case of a single resonance separated by a spacing $D \gg \Gamma$ from other resonances. However, as we have shown in section 8.4, as the average spacing becomes comparable with the average width, the amplitude of fluctuations, and correspondingly, the separation of maxima and minima in the auto-correlation function, is damped. Fig. (51) illustrates the relative difference between the height of the maximum at $\epsilon = 0$ and the first minimum for the

FIG.51

DAMPING OF AUTOCORRELATION FUNCTION AS A FUNCTION OF D/Γ

THE DAMPING COEFFICIENT $R(D/\Gamma)$, Eq.9.5, CALCULATED FROM
THE PICKET FENCE MODEL.



picket-fence auto-correlation function as a function of D/Γ , normalized to 1.0 at $D/\Gamma = \infty$. Thus it is necessary to introduce a damping term in equation (9.4) to include the proximity of additional resonances. The function then resembles

$$F(\epsilon) = \left(\frac{\pi}{k}\right)^2 \left(\frac{(2J+1)}{(2i+1)(2I+1)}\right)^2 \frac{16\Gamma_d^{\uparrow 2}\Gamma_d^{\downarrow 2}}{\Gamma_d^4} \left(R\left(\frac{D_d}{\Gamma_d}\right)\right) \frac{1}{1 + \frac{(E_o - \epsilon)^2}{\Gamma_d^2}} \quad (9.5)$$

where R is the damping function.

And the variance in the cross-section is equal to $F(0)$

$$\text{VAR } \sigma = \left(\frac{\pi}{k}\right)^2 \left(\frac{(2J+1)^2}{(2i+1)^2(2I+1)^2}\right)^2 \left(\frac{16\Gamma_d^{\uparrow 2}\Gamma_d^{\downarrow 2}}{\Gamma_d^4}\right) R(D_d/\Gamma_d) \quad (9.6)$$

If we assume further that the relative branching to the entrance channel and the various exit channels is similar for all resonances and all nuclides;

$$\Gamma_d^{\uparrow} = \alpha\Gamma_d \quad \Gamma_d^{\downarrow} = (1-\alpha)\Gamma_d. \quad (9.7)$$

Then equation (9.6) becomes.

$$\text{VAR } \sigma = \beta \left(\frac{\pi}{k}\right)^2 \left(\frac{(2J+1)}{(2i+1)(2I+1)}\right)^2 R\left(\frac{D_d}{\Gamma_d}\right) \quad \text{where } \beta = 16(\alpha)^2(1-\alpha)^2 \quad (9.8)$$

Implicit in this derivation are these assumptions:

- (1) All resonances have the same total width, Γ_d , permitting a direct evaluation of the auto-correlation function in terms of this width.
- (2) The relative branching to entrance and decay channels is equal for all resonances.

(3) All resonances have the same total spin, J .

These assumptions can not be justified on physical grounds, and, in fact, from Chapter VII, clearly assumption (1) is invalid. However, the effect of excluding these assumptions will be to introduce a randomness in individual resonances which will tend to cancel in the calculation of the variance.

Now the variance in the cross-section, from the Ericson theory, is given by

$$\text{VAR } \sigma = \left(\frac{\pi}{k^2}\right)^2 \frac{1}{(2i+1)^2 (2I+1)^2} \frac{k}{\pi} \frac{D}{\Gamma} \sum_e (2J+1)^2 T_{\ell s}^J \quad (9.9)$$

where $T_{\ell s}^J$ = optical model transmission coefficient

k = parameter related to distribution of Γ_i

It is evident from a comparison of equations (9.8) and (9.9) that the dependence on ground state spin in the two formulations is identical. Therefore the conclusion of Foster and Glasgow with respect to the exclusion of doorway state resonances is invalid.

Other similarities are evident from a detailed examination of the two functions. The Ericson equation is linear D/Γ , where these are parameters of compound nucleus resonances, and the doorway state variance is a monotonic increasing function of D_d/Γ_d , which in the limit of $D_d \sim \Gamma_d$ is approximately linear. Furthermore, as shown by Feshbach⁽³⁾ et al the doorway state strength function is equal to a local average of the compound nucleus strength function.

Thus

$$\frac{D_d}{\Gamma_d} = \frac{\langle D \rangle}{\langle \Gamma \rangle}$$

Some consideration may be given to the possible final angular momentum states of the compound system. The optical model transmission coefficients for $A \leq 40$ and $E_n < 2,5$ MeV are dominated by the $\ell = 0$ term. Therefore it is justifiable to include in the summation of equation (9.9), only the $\ell=0$ term. Furthermore, Block and Feshbach⁽³⁷⁾ have shown that for $A \leq 40$, the 2p-1h states of excitation less than a few MeV are predominantly $\ell=0$. Thus in both equation (9.9) and (9.8) we may consider only the terms for $J = I \pm 1/2$. Interestingly, if one considers just this component, the dependence of the variance on ground state spin vanishes, at least in first approximation, and the variance is dependent only on the damping coefficient $R(D/\Gamma)$.

As will be shown, the magnitude of the branching to the entrance and decay channels is not constant over all elements, thus the derivation, although useful in delineating the spin dependence on fluctuation amplitudes, is not uniquely dependent on variations in the strength function estimates. In consideration of the assumptions inherent in this derivation, and the sampling errors introduced by a calculation of the strength function over a relatively limited energy range, little apparent correlation exists between the amplitude of the fluctuations and the strength function estimate.

Returning to the correlation between the amplitude of fluctuations and the ground state spin, it is evident that the lack of correlation, both theoretically and experimentally, in the present work is to some extent peculiar to the mass-energy region under examination. For if, in fact, the orbital angular momentum is permitted to assume non zero values, the close correlation between the J and I in equation (9.9) will be modified, and the denominator will dominate. Such a situation will arise if the magnitudes of the transmission coefficients for non-zero angular momenta dominate the $\ell=0$ term, and this situation is indeed true as the bombarding energy increases and as one proceeds to regions of higher atomic mass. Similarly, the results of Block and Feshbach have shown that as the atomic mass increases, the predicted $2p-1h$ states have angular momentum of $\ell=1$ &/or $\ell=2$ dependent on mass number.

9.3 Cross-Section Fluctuation and Nuclear Deformation

In the previous section the theoretical aspects of the amplitude of doorway resonances were discussed. It was shown that the amplitude of these resonances, using the approximations mentioned, is nearly independent of the ground state spin, and dependence on the strength function is only introduced as a consequence of the damping of the amplitudes from the proximity of near resonances.

However, in the cross-sections discussed in the present experiment, the variance of the cross-section differs by greater

than an order of magnitude over the range of masses. Clearly, this range is outside the range of variances expected from statistical uncertainties. Therefore, some mechanism must be present to explain this anomalous behavior.

Some indication is provided by the experimental observations of Seth⁽³⁶⁾. In the seventeen elements examined in that work, it was observed qualitatively that the amplitude of resonance structure was maximized for the highly deformed nuclides, Gd and Nd.

Therefore let us assume a priori that the amplitude of the doorway state resonance is linearly proportional to the magnitude of the deformation, characterized by the parameter β which is just equal to $\Delta r/r$, the difference between maximum and minimum radius divided by the mean value. From the discussion of section 9.2 then, the auto-correlation function is proportional to β^2 . Fig. (52) is a graph of the variance in the cross-section as a function of β^2 using the data of Gove⁽⁶³⁾ for the deformation parameter. The values used are also shown in Table VII. Within the scatter of experimental points, this dependence may be fitted by a linear function of β^2 , and yields a correlation coefficient $r = 0.63$.

Other characteristics of the parameters affecting the magnitude of the variance are evident from an observation of the ground state spins of the targets.

The data points fall naturally into three groups along

Fig.52

RELATION BETWEEN VARIANCE AND DEFORMATION PARAMETER.

THE VARIANCE IN THE EXPERIMENTAL CROSS-SECTIONS IS PLOTTED AS A FUNCTION OF THE NUCLEAR DEFORMATION PARAMETER.

THE CALCULATED CORRELATION COEFFICIENT IS 0.63, WHICH IS SIGNIFICANT AT THE .05 LEVEL.

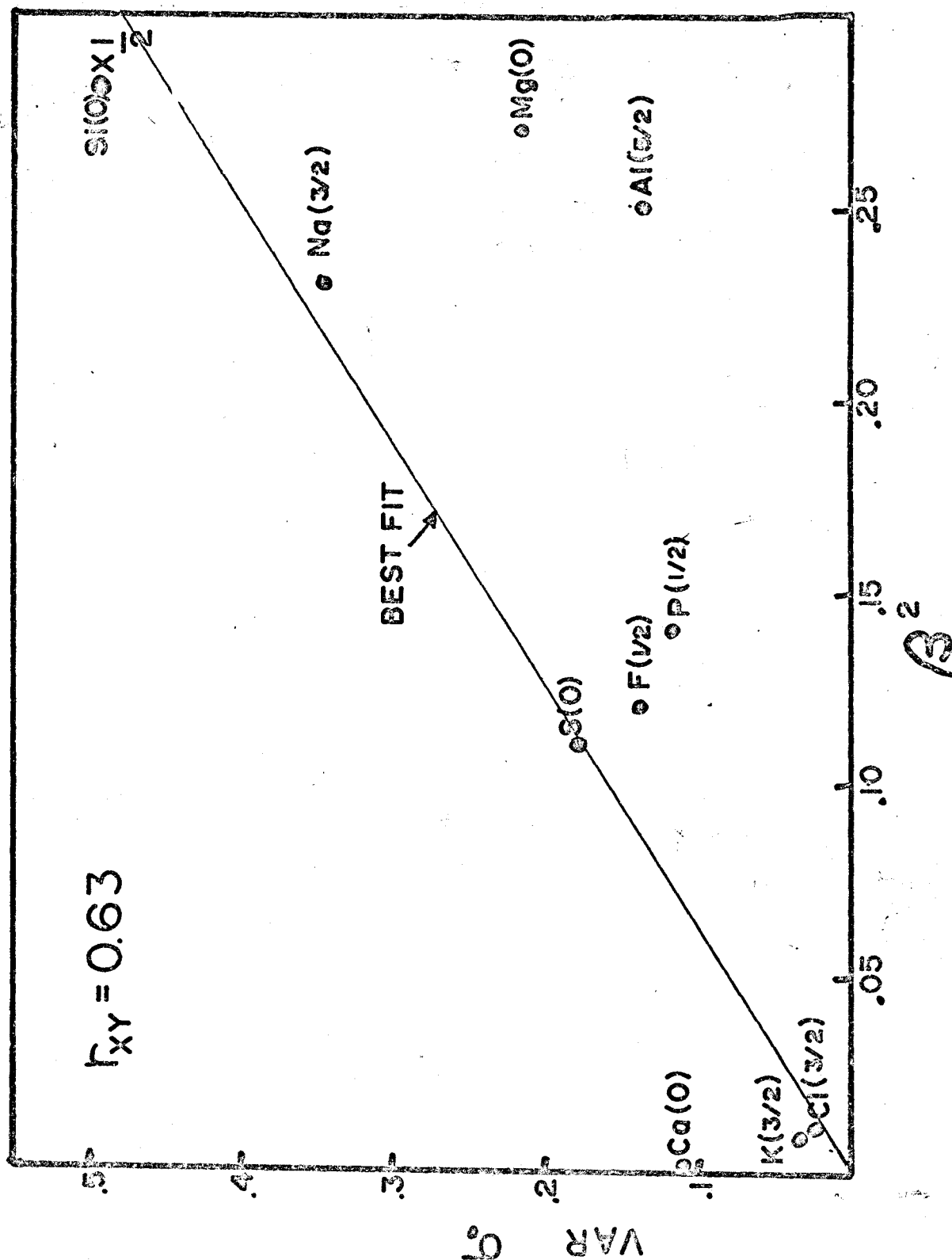


Table VII

Spin , Deformation, and Autocorrelation Function A=19-40

Hypothesized Dependence on I and β are tabulated.

Element	I	β	$1/(2I+1)^2$	β^2	$VAR\sigma$
F	1/2	.35	.25	.12	.14
Na	3/2	.48	.06	.23	.35
Mg	0	.52	1	.27	.22
Al	5/2	-.50	.028	.25	.14
Si	0	-.52	1	.27	1.0
P	1/2	-.37	.25	.14	.12
S	0	-.33	1	.11	.18
Cl	3/2	-.10	.06	.01	.025
K	3/2	-.08	.06	.006	.033
Cu	0	0	0	0	.11

the ordinate, and within each group, there exists a trend toward lower variance with increasing ground state spin. Clearly the dependence is not nearly as strong as the $1/(2I+1)^2$ dependence suggested by Foster and Glasgow, and qualitatively resembles more closely the weak dependence suggested in section 9.2.

It is not obvious how the functional relationship between the variance and the nuclear deformation parameter enters into the theoretical expression for the variance, equation (9.8). To place this phenomenon in the context of the doorway state model, it is necessary to re-examine the assumptions of this model. It has been assumed that these states result from the application of a residual interaction of two-body form to the system of (beam particle + target nucleus). The residual interaction, it will be remembered, is the difference between the total Hamiltonian and the optical model-type Hamiltonian responsible for the broad single-particle resonance structure in the total cross-section.

Now in section 9.2 we assumed that the relative branching to the entrance channel and the decay channel was independent of specific nuclear properties. However, on the average, the matrix element between the doorway state and decay channels in the deformed nucleus may differ substantially from the $(2p-1h \rightarrow 3p-2h)$ matrix element of the undeformed, shell model type nucleus. Therefore the assumption leading to the

expression for the variance, equation (9.8) is no longer valid. The dependence of the average resonance amplitude, on deformation, therefore, is evidenced as a variation of the product term $\Gamma_d^\uparrow \Gamma_d^\downarrow$ resulting from the detailed form of the residual interaction.

Now the widths are related to the matrix element between the doorway state and the entrance channel, or decay channels, as discussed in section 1.4,

$$\Gamma_d^\uparrow = |\langle \psi_0 | V_R | \psi_d \rangle|^2 \quad (9.10)$$

$$\Gamma_d^\downarrow = |\langle \psi_0 | V_R | \phi_s \rangle|^2 \quad (9.11)$$

Hence, the variation in branching ratio as a function of deformation is evidence of some deformation-dependent component in the matrix elements (9.11) and (9.12). In the paper of Seth⁽³⁶⁾ previously cited, a different form of the residual interaction, to form (particle+collective excitations) states was postulated. However numerous theoretical calculations have shown that the concept of a residual two-body interaction is valid for deformed nuclei. A necessary conclusion, then, is that the dependence of the matrix element on deformation resides in the number and character of the states available for formation and decay.

Certain properties of these states may be hypothesized from the mode of formation. From the optical model transmission coefficients, the states must be primarily $\ell=0$ or $\ell=1$ states,

leading in the case of an even-even target to states of $J = 1/2\pm$, $3/2\pm$. Furthermore the states are a restricted subset of the multiplicity of stable eigenstates of the compound nucleus; the entrance channel being a single particle state, the doorway state, a 2p-1h state, etc.

Considering only the entrance channel, then, in the case of an undeformed "shell model" nucleus, the entrance channel will be defined by the overlap between the unbound wave function, and nearby shell model states with $\ell=0,1$. Now when the nucleus is deformed the degeneracy in l_z is removed and each shell model state is split into $(2J_s+1)$ states with $J = 1/2, 3/2 \rightarrow J_s$. Thus the presence of deformation results in an increase in the number of possible entrance channel configurations available to the incident neutron. The effect of deformation on the formation of the doorway state and more complex configurations is somewhat analogous in that the number of available 2p-1h, 3p-2h, etc. states should be increased by removal of the degeneracy in ℓ_z .

However because these more complex configurations result from one or more excitations of particles from the core, the total angular momentum is not as strongly restricted to low values. Now the effect of deformation is to increase the number of available states of low total angular momentum proportionately over states of higher angular momentum. Therefore, the effect of deformation should be most strongly felt in

the matrix element with the entrance channel and less so in the matrix element between the doorway state and complex configurations.

Block and Feshbach⁽³⁷⁾ have assumed $\Gamma_d \downarrow \gg \Gamma_d \uparrow$ in their calculations. Consider the term in the variance expression, equation (9.8), then:

$$\frac{\Gamma_d \uparrow \Gamma_d \downarrow}{(\Gamma_d \uparrow + \Gamma_d \downarrow)^2} = \alpha(1-\alpha) \quad (9.12)$$

It is clear that this expression is maximized for $\alpha = 0.5$, or $\Gamma_d \uparrow = \Gamma_d \downarrow$. Then an increase in the branching to the entrance channel, reducing $\Gamma_d \downarrow$, would increase the average amplitude of the doorway state resonances. Hence it is seen that the mechanism by which nuclear deformation affects the formation of doorway states, by increasing the number of low angular momentum states available, at least qualitatively predicts the dependence of the variance of the cross-section on the deformation parameter.

The character of the states of the deformed nuclei may also explain in part the distributions of widths shown in Fig. 38. Since the Nilsson levels originate from shell model states of widely divergent l and J , it is reasonable to assume a wider variation in the widths of doorway states observed in deformed nuclei. Thus the observation that in most cases observed in the present series, the total widths may assume values from ten kilovolts to several hundred kilovolts may be explainable on this basis.

REFERENCES

1. Bohr, N., Nature 137, 344 (1936).
2. Bethe, H. A. Rev. Mod. Phys. 9, 69 (1937).
3. Feshbach, H., Kerman, A. K. and Lemmer, R.H. Ann. Phys. 41, 230 (1967).
4. Perey, F. and Buck, B., Nuc. Phys. 32, 353 (1962).
5. Hauser, W. and Feshbach, H. Phys. Rev. 87, 366 (1952).
6. Porter, C. F. and Thomas, R.G. Phys. Rev. 104, 483 (1956).
7. Feshbach, H. Ann. Phys. (N.Y.) 5 357, (1958).
8. Feshbach, H. Ann. Phys. (N.Y.) 19, 287 (1962).
9. Franco, V. and Lemmer, R.H. MIT Report - to be published.
10. Lemmer, R. H. and Shakin, C. Ann. Phys. (N.Y.) 27, 13 (1964).
11. Le Couteur, K.J. Phys. Let. 11, 53 (1964).
12. Kerman, A.K., Rodberg, L.S. and Young, J.F. Phys. Let. 11, 422 (1964).
13. Barschall, H.H, Bockelman, C.K, Peterson, R.E and Adair, R.K . Phys. Rev. 76, 1146 (1949).
14. Barschall, H.H, Mooring J.K., Petree, B. . Phys. Rev. 82, 378 (1951).
15. Barschall, H.H. Rev. Mod. Phys. 24, 120 (1952).
16. Barschall, H.H. Phys. Rev. 86, 431 (1952).
17. Miller, D.W., Adair, R.K., Bockelman, C.K. and Darden S. Phys. Rev. 88, 83 (1957).
18. Frier, G. Fulk, M. Lampi, E.E. and Williams, J.H., Phys. Rev. 78, 508 (1950).
19. Hibdon, C. T. Phys. Rev. 114, 79 (1959).
20. Cabe, J. , Laurat, M. and Yvon P. . Priv. Commun. in BNL325.

21. Wills, J.E. Bair, J.K. Cohn, H.O. Willard H.B. Phys. Rev. 109, 891 (1958).
22. Stelson, P. H. and Preston, W.M. Phys. Rev. 88, 1354 (1952).
23. Ricamo, R. Nuovo Cimento 8, 383 (1951).
24. Nerenson, N. and Darden, S. Phys. Rev. 89, 775 (1953).
25. Ibid. Phys. Rev. 94, 1678 (1954).
26. Foster, D.G. and Glasgow, D.W. Nucl. Inst. Meth. 36, 1 (1965).
27. Ibid. Phys. Rev. C3, 576 (1971).
28. Galloway, L. A. and Schraeder, E.F. Case Institute Report COO-1573-6.
29. Feshbach, H., Porter, C.F., and Weisskopf, V.W. Phys. Rev. 90, 166 (1953).
30. Nemirovski, . Proc. Int. Conf. Peaceful Uses At. Energy Geneva (1955).
31. Bjorklund, F., Fernbach, S. and Sherman, . Phys. Rev. 101, 1832 (1956).
32. Culler, G., Fernbach, S. and Sherman, N. . Phys. Rev. 101, 1047 (1956).
33. Monahan, J. E. and Elwyn, A.J., ANL 7081, p. 24 (1965).
34. Ibid. Phys. Rev. 153, 1148 (1967).
35. Singh, P. R. et. al. Nuc. Phys. 65, 577 (1965).
36. Seth, K. K. Phys. Let. 16, 306 (1965).
37. Block, B. and Feshbach, H. Ann. Phys. N.Y. 23, 47 (1963).
38. Agodi, A. and Pappalardi, G. Nuc. Phys. 47, 129 (1963).
39. Monahan, J.E. and Elwyn, A.J. Nucl. Phys. A93, 683 (1967).
40. Ibid. Phys. Rev. Let. 20, 1119 (1968).
41. Shakin, C. Ann. Phys. (N.Y.) 1, 373 (1963).

42. Shakin, C. Ann. Phys. (N.Y.) 22, 54 (1963).
43. Arad, B. Proc. 3rd Int. Conf. Peaceful Uses At. Energy Geneva (1964) United Nations, N.Y. (1965).
44. Schwartz, C. O. and Owen, G.E. in Fast Neutron Physics p. 212 Interscience Publishers (1960).
45. Fano, V. Phys. Rev. 72, 26 (1947).
46. MacDonald, W. J. and Gedke, D.A. Nuc. Inst. Meth. 55, 1 (1967).
47. Bratenahl, A., Peterson, J.M. and Stoering, J.P., Phys. Rev. 110, 927 (1958).
48. Miller, D.W. in Fast Neutron Physics p. 999, Interscience Publishers (1960).
49. Seth, K. K., Bilpuch, E. and Newson, H.W., Nuc. Phys. 47, 137 (1963).
50. Huddleston, C. M. et al. Phys. Rev. 117, 1055 (1960).
51. Johnson, R. G. Private communication in BNL 325 Supp. 2 (1964).
52. Manero, F. et al. Private communication in BNL 325, Supp.2 (1964).
53. Towle, S.H. and Gilboy, W.B. Nuc. Phys. 32, 610 (1962).
54. Johnson, R. G. Private Communication in BNL 325, Supp. 2 (1964).
55. Smith, W. R. Comp. Phys. Comm. 1, 106 (1969).
56. Ericson, T. Ann. Phys. (N.Y.) 23, 390 (1963).
57. Feshbach, H. Int. Conf. on Nuc. Structure
58. Merzbacher, E., Crutchfield, P.W. and Newson, H.W. Ann. Phys. (N.Y.) 8, 194 (1959).
59. Heidmann, J. and Bethe, H.A. Phys. Rev. 84, 274 (1951).
60. Blatt, J. M. and Weisskopf, V.W. Theoretical Nuclear Physics: New York, John Wiley and Sons (1952).
61. Bracewell, R. "The Fourier Transform and its Applications" McGraw Hill (1965).

62. Gove, H.E., Proc. Int. Conf. Nuc. Structure, Kingston
Canada Ed. Bromley and Vogt, University of Toronto (1960)
North Holland.